Title
The Future of Bulk Microphysics Schemes

Author
Hu, Arthur Z.

Publication Date
2023

Peer reviewed|Thesis/dissertation

The Future of Bulk Microphysics Schemes

By

ARTHUR HU

DISSERTATION

Submitted in partial satisfaction of the requirements for the degree of

DOCTOR OF PHILOSOPHY

in

ATMOSPHERIC SCIENCE

in the

OFFICE OF GRADUATE STUDIES

of the

UNIVERSITY OF CALIFORNIA

DAVIS

Approved:

Adele Igel, **Chair**

Matthew Igel

Shu-Hua Chen

Committee in Charge

2023

Table of Contents

Acknowledgement

I would like to first express my gratitude to Professor Adele Igel for introducing me to the world of cloud microphysics modeling, financially supporting me, and training me to be an independent researcher. It has been an incredible ride. I'd also like to thank all current and past members of the Igel Research Group and my dissertation committee for providing valuable advice.

It was also a great honor to be able to work with some wonderful microphysicists outside of UC Davis, including Patrick Chuang (my senior thesis advisor), Mikael Witte, Hugh Morrison, Marcus van Lier-Walqui, and Sean Santos. I would like to thank Adele again for introducing me to some of them and indirectly helping me secure my postdoc position at the Columbia University. I'm looking forward to working with them even after my graduation.

Having had ups and downs during my PhD career, I'd like to thank all my ASGG friends, Mahjong friends, Karaoke friends, and my families especially my cousin Jessica for keeping me sane whenever I was in a slump. And lastly, I'd like to thank my parents for their immense support. They're not typical Asian parents, but I hope I made them a little prouder and a little less disappointed.

Abstract

Atmospheric models are getting progressively more sophisticated as computational power has grown exponentially over the past few decades. The module responsible for predicting the evolution of hydrometeors, the microphysics scheme, has also gone through a series of updates. However, in the operational forecasting world, its moment-resolving structure has remained largely unchanged due to its high computational efficiency compared to a bin scheme or the more recently developed Lagrangian superdroplet method, without losing too much accuracy. In this dissertation, we seek to improve the bulk scheme in its current state and also give guidance to its future development, from an improved shape parameter diagnostic equation, to understanding the structural limitation of bulk schemes in general, and to exploring a more natural representation of a droplet size distribution that could potentially be the beginning of a paradigm shift for bulk schemes in numerical weather prediction.

Observational records from five in-situ flight campaigns were used to improve our understanding of aerosol-dispersion effect and the shape parameter diagnostic equation in a bulk scheme. We identify the reason why past studies found inconsistent sign of the aerosol-dispersion correlation by distinguishing local correlation from cloud-mean correlation. No clear correlation is found between cloud-mean aerosol concentration and cloud-mean dispersion, while in-cloud regions with high droplet dispersion are typically associated with low local droplet concentration. A new equation is proposed to diagnose the shape parameter in marine warm stratocumulus clouds for double moment bulk schemes in cloud-resolving models or large-eddy simulations.

We use a special bulk scheme called Arbitrary Moment Predictor (AMP) to understand the effect of structural differences between bin and bulk scheme. One-dimensional kinematic simulations show that overall differences between AMP (bulk) and bin schemes are small. They produce similar mean liquid water path, but AMP has a significantly lower mean precipitation rate due to slower precipitation onset. The primary reason for the divergence between the two schemes is found to be the collision-coalescence process, particularly autoconversion. By adjusting the diameter cutoff between cloud and rain categories in AMP, the largest difference between the two schemes can be reduced to about 10%, making the structural differences between AMP and bin schemes smaller than the parameterization differences between two bin schemes.

To explore the feasibility of a bulk scheme with unified liquid water category, we upgrade AMP to be configurable as a unified category bulk scheme (U-AMP) in addition to its original separate category setting (S-AMP). Due to our lack of knowledge of such a novel scheme, we first perform an extensive search for the best configuration regarding the optimal moments to predict and the best assumed shape parameter under a variety of initial conditions. When configured optimally, U-AMP far outperforms S-AMP in estimating precipitation rate, with which S-AMP struggles the most. U-AMP is also on par with S-AMP in estimating other quantities such as CWP, RWP, and LWP, where S-AMP already makes near-perfect predictions compared to bin schemes. U-AMP's superiority over S-AMP in simulating certain precipitation patterns is mostly due to its ability to situations where multiple modes exist within the traditional rain category ($D > 80\ \mu m$), which can occur when large raindrops fall through a layer of small raindrops. Such structural improvements by U-AMP could mark the beginning of a shift in the paradigm for bulk scheme development.

1 Introduction

Clouds and aerosols have a large impact on Earth's weather and climate systems due to their role in regulating the planet's radiation budget and affecting atmospheric processes. They modulate Earth's radiation budget by reflecting, absorbing, and transmitting incoming shortwave radiation and outgoing longwave radiation (Boucher et al., 2014; Stephens, 2005). Clouds, depending on their height, can either cool the climate by reflecting sunlight back into space or warm it by trapping the outgoing longwave radiation (Hartmann, 1992; Trenberth et al., 2007). Similar to clouds, aerosols can also affect their environment on multiple levels. They can directly affect the radiation budget by scattering and absorbing solar radiation (aerosol direct effect) and indirectly impact the atmospheric by altering cloud properties and precipitation patterns (aerosol indirect effects; Albrecht, 1989; Twomey, 1977). Aside from their relevance in climate science, aerosols and clouds are also the precursors to precipitation, making our understanding of them crucial for short-term weather prediction. Aerosols can act as cloud condensation nuclei (CCN) or ice nucleating particles (INP), which influence cloud droplet and ice crystal formation, which leads to changes in cloud lifetime, albedo, and precipitation patterns (U. Lohmann & Feichter, 2005; Rosenfeld et al., 2008; Stevens & Feingold, 2009). Enhancing the accuracy in representing aerosols, clouds, and their interactions in atmospheric models is therefore critical for reliable climate predictions and weather forecasts.

Accurate modeling aerosols and clouds poses significant challenges. The primary difficulties can be summarized into three categories: (a) the vast number, the variety of shape (aerosol and ice particle), and/or chemical composition (aerosol) of the particles involved, (b) the lack of fundamental understanding of the processes involved (Morrison, van Lier-Walqui, Fridlind, et al., 2020; Pöschl, 2005), and (c) the nonlinearity of aerosol-cloud interactions. With quintillions of cloud droplets and aerosols in a typical cloud, it is infeasible to predict the evolution of each particle, its environment, and their interactions. In current operational and research atmospheric models, aerosol and clouds are modeled using microphysics schemes, which abstracts the processes involving individual particles through parameterizations.

Aside from the recently developed Lagrangian super droplet method (e.g., Shima et al., 2009), the two most well-established microphysics scheme types are the bulk microphysics and bin microphysics schemes. Bin schemes track the number of droplets within discrete size or mass ranges (i.e., size-resolved or mass-resolved), allowing the particle size distribution (PSD) to evolve freely but with higher computational cost (A. P. Khain et al., 2015). Bulk schemes, in contrast, predict quantities proportional to moments of the PSD (i.e., moment-resolved), typically mass and number concentration (e.g., Kessler, 1969; Lin et al., 1983; Meyers et al., 1997). Albeit not a required feature for bulk schemes in principle, they usually prescribe a gamma probability distribution for the PSD, which is less flexible but can be one or two orders of magnitude more computationally efficient than bin schemes (Morrison, van Lier-Walqui, Fridlind, et al., 2020). This limits bin schemes to research purposes and renders bulk schemes the only viable option for operational weather forecasting and global-scale climate prediction. Improving the accuracy of bulk schemes, particularly in their treatment of aerosol, clouds, and their interactions, can potentially have a significant impact on our ability to predict future weather and climate events and guide policymaking.

Bulk schemes have evolved considerably since the seminal work by Kessler (1969), which introduced a microphysics scheme that predicted only the mass mixing ratio of liquid water (cloud and rain) without considering the shape of the size distribution. Ice microphysics was later included near 1980 (Koenig & Murray, 1976; Lin et al., 1983; Rutledge & Hobbs, 1984), which made the schemes more realistic with a more accurate (slower) sedimentation rate of ice and the inclusion of latent heat transfer through freezing and melting (Fovell & Ogura, 1988; Gao et al., 2006; Q. Liu et al., 1997; Lord et al., 1984; McCumber et al., 1991). In the 1990s and 2000s, the next major update to bulk scheme brought the inclusion of another moment (number concentration) as well as aerosol-cloud interactions (Ghan et al., 1997; Khairoutdinov & Kogan, 2000; Ulrike Lohmann et al., 1999; Ming et al., 2007; Morrison & Gettelman, 2008; Rotstayn & Liu, 2003). Recent developments in bulk schemes (post-2010) have focused on higher-resolution (kilometer-scale) operational weather prediction (Benjamin et al., 2016; Jason A. Milbrandt et al., 2016; Vie et al., 2016) and incorporating machine learning into autoconversion parameterization (Chiu et al., 2021; Seifert & Rasp, 2020), which bulk schemes are known to struggle with. Aiming to better understand the limitations of bulk schemes and provide guidance for their future development, this dissertation uses observational records to address some known issues in bulk schemes concerning aerosol-cloud interaction, uses modeling results to identify the effects of the structural difference between bin and bulk schemes, and explores the feasibility of a new type of bulk scheme with unified liquid water category, which can potentially mark the beginning of a paradigm shift for bulk schemes in numerical weather prediction.

Aerosols and clouds interact through what is known as aerosol indirect effects. The two widely known effects are the cloud albedo effect and the lifetime effect. The cloud albedo effect refers to the situation where higher aerosol concentration leads to smaller cloud droplets but higher total surface area, which reflects more sunlight (Twomey, 1977). Smaller cloud droplets also mean less total precipitation, leaving more of the cloud suspending in the sky and reflecting sunlight, which is known as the lifetime effect (Albrecht, 1989). One of the lesser known aerosol indirect effects is its "dispersion effect" (Y. Liu & Daum, 2002), which refers to the idea that cloud droplet distributions formed in higher aerosol concentration environments will have different values of relative dispersion (the ratio of standard deviation and mean droplet size) from those formed in low aerosol concentration, which in turn impacts the albedo of the clouds. Aside from its significance in radiative forcing, this aerosol-dispersion relationship is also used in diagnosing the shape parameter in bulk microphysics schemes (Morrison & Grabowski, 2007; Peng & Lohmann, 2003; Thompson et al., 2008). However, all of these bulk scheme implementations use the cloud-mean relationship between aerosol and cloud to describe the aerosol-dispersion effect across all scales, whereas there is no consensus on even the sign of this effect across different scales (e.g., Chandrakar et al., 2016; Igel & van den Heever, 2017; Y. Liu & Daum, 2002; Wang et al., 2021, more in Table 1.1). Chapter 2 aims to reconcile this issue by distinguishing local correlation from cloud-mean correlation.

After investigating aerosol-cloud interaction through our observational study, we recognize the importance of understanding microphysical processes to improve the accuracy of atmospheric models. Atmospheric models rely on microphysics schemes, such as bin and bulk schemes, to represent these microphysical processes. Bin schemes predicts the number of droplets within discrete size or mass ranges, while bulk schemes predict bulk quantities proportional to moments of the PSD, typically mass and number concentration. Aside from this structural difference, bin and bulk schemes also parameterize physics differently, such as velocity-diameter relationship, collision-coalescence parameterization, condensation formulation, etc. Although there has been a number of studies that compared the advantages and disadvantages of bin and bulk schemes (Fan et al., 2012, 2016; Li et al., 2009; Seifert & Beheng, 2006a, 2006b), the focuses of these studies are on the *existing* schemes. This means that the differences shown in their bin-bulk comparison can be a result of (a) the presence of an aerosol budget, (b) adoption of saturation adjustment, (c) parameterization of autoconversion, etc. However, none of these studies were able to draw any meaningful conclusion about the effect of their structural difference due to other compounding factors. With the help of Arbitrary Moment Predictor (AMP), the effect of bin-bulk structural difference can be assessed in great detail in Chapter 3. We compared the mean value and the trend of liquid water path and surface precipitation in full microphysics settings. The effect of bin-bulk structural difference is also assessed for individual microphysical processes (nucleation, condensation, evaporation, collision-coalescence, and sedimentation) to see which process contributes to the final error the most.

Drawing on the insights from the study on bin-bulk structural difference, we identified the strengths and weaknesses of a theoretical bulk scheme that uses the same set of physical routines as a bin scheme. One notable weakness of a bulk scheme is in fact not required by its structure but adopted by virtually all existing bulk schemes, i.e., a separate cloud and rain category with a predefined size boundary between the two. In Chapter 4, we use an updated version of AMP to explore the possibility of a unified category bulk scheme that treats cloud and rain particles within a single category. We aim to assess the potential benefits and limitations of such unified category bulk scheme by evaluating its performance against an existing separate category bulk scheme. This innovative approach has the potential to simplify the representation of cloud microphysical processes and bridge the gap between cloud-derived and rain-derived processes.

2 Aerosol-Dispersion Effect

2.1 Background

The amount of aerosol is a key parameter modulating cloud microphysical and macrophysical properties and their subsequent long-term impact on climate. Broadly speaking, aerosol has two primary effects on cloud microphysics of warm-phase clouds. The first is the cloud albedo effect (Twomey, 1974, 1977): given a fixed amount of liquid water content, an increase in aerosol concentration (N_a) leads to smaller droplets but higher total surface area, which reflects more sunlight. The second is the lifetime effect (Albrecht, 1989): as smaller droplets are slower to precipitate, more liquid water remains as part of the cloud and spend more time reflecting sunlight. These two mechanisms can change the average albedo of the Earth and thus affect the climate.

A lesser-discussed effect is the proposed "dispersion effect" (Y. Liu & Daum, 2002). Dispersion, or more specifically, relative dispersion (ϵ) is defined as the ratio of standard deviation and mean droplet size, and it is one way to quantify the width of the distribution, i.e., smaller ϵ for a narrower distribution, and vice versa. The dispersion effect refers to the idea that cloud droplet distributions formed in higher aerosol concentration environments will have different values of relative dispersion from those formed in low aerosol concentration, which in turn impacts the albedo of the clouds.

Table 2.1. Summary of Selected Past Literatures on the Topic of Dispersion Effect.

	Positive correlation	No correlation	Negative correlation
Intra-cloud $\epsilon - N_d$	Y. Wang et al., 2021 ($\epsilon - N_{a,i}$)		Igel & van den Heever, 2017; C. Lu et al., 2012; M.

			Lu et al., 2007; Pawlowska et al., 2006
Inter-cloud $\epsilon - N_d$ or $\epsilon - N_a$	Costa et al., 2000; Liu & Daum, 2002; M.-L. Lu et al., 2007; Martin et al., 1994; Pandithurai et al., 2012; Pawlowska et al., 2006; Rotstayn & Liu, 2003; Yum & Hudson, 2005	Prabha et al., 2012	Chandrakar et al., 2016; Gonçalves et al., 2008; Grabowski, 1998; Hsieh et al., 2009; M. L. Lu & Seinfeld, 2006; Ma et al., 2010; Martins & Silva Dias, 2009; X. Wang et al., 2011

Since the initial proposal of this effect, the sign of the $\epsilon - N_a$ and the closely related $\epsilon - N_d$ (droplet number concentration) correlation has been a highly debated subject. Table 1 summarizes the results from these previous studies. While the initial studies on the topic championed a positive correlation between the two quantities, many studies have since found the opposite relationship. In this study, we propose that some of the disagreement can be resolved by consciously recognizing that the impact of aerosol number concentration on relative dispersion can be observed from two perspectives: intra-cloud and inter-cloud correlation. Intra-cloud correlation represents the local correlation between ϵ and N_d within a cloud, while inter-cloud correlation represents how the cloud-mean values of the two quantities correlate among a large set of clouds. The inter-cloud $\epsilon - N_d$ correlation sheds light onto how the background aerosol concentration affects the mean properties of the clouds since cloud-mean N_d may better serve as a proxy for pre-cloud N_a. On the other hand, the intra-cloud correlation may better reveal how the cloud microphysical processes including non-aerosol factors (e.g., updraft velocity and entrainment) cause droplet concentration and relative dispersion to co-vary. Table 1 shows that while there is indeed disagreement about the inter-cloud correlation, there is universal agreement that the intra-cloud correlation is negative.

Some studies have recognized these two perspectives (e.g., Lu et al., 2007 who discuss "in-flight" relationships and "ensemble-averaged" relationships), but most have not. In particular, the lack of distinction has been problematic when parameterizing the relative dispersion in bulk microphysics schemes. The positive inter-cloud correlation has been used to develop empirical diagnostic equations for relative dispersion based on droplet concentration in these schemes (Morrison & Grabowski, 2007; Peng & Lohmann, 2003; Thompson et al., 2008). When these schemes are used in cloud-resolving and large eddy simulations, the effect is to diagnose high relative dispersion in grid boxes where the local droplet concentration is high and vice versa. In this context, the schemes are using an equation based on a positive *inter*-cloud correlation to diagnose the *intra*-cloud variation of relative dispersion. Such a diagnosis is inappropriate since all previous studies tell us that a negative intra-cloud correlation is expected (Table 2.1).

The objectives of this study are to explicitly show that inter-cloud and intra-cloud analysis do not result in the same relationship between ϵ and N_d, to discuss the underlying physical reasons for why they are not the same, and to propose an alternative diagnostic equation for the relative dispersion for use in bulk microphysics schemes in cloud-resolving models.

We will do so by analyzing five in-situ campaign datasets that were collected in vastly different places around the world (see Section 2.2). Section 2.3 presents the results of the inter- and intra-cloud $\epsilon - N_d$ correlation. Section 2.4 describes the development of a new diagnostic relative dispersion equation and the performance of the diagnosis. Section 2.5 gives some concluding remarks of the findings.

2.2 Data Sources

We analyze in-situ measurements from five flight campaigns performed over the Pacific and Atlantic (see Table 2.2). Flights in all five campaigns surveyed exclusively shallow warm phase clouds, most of which were stratocumulus clouds (VOCALS, MASE, POST, and most of ORACLES), while some were cumuli (some in ORACLES and all in GoMACCS). For any given flight, there could be one or multiple clouds being surveyed. This dataset captures day-to-day meteorological variation, cloud-to-cloud variation under the same meteorological settings, and intra-cloud variation. As such, the dataset is well suited to address our objectives.

We also choose these campaigns because of their similar set of instrumentation. In each campaign, the measurement of interstitial (unactivated) aerosol number concentration $N_{a,i}$ was recorded by a Passive Cavity Aerosol Spectrometer (PCASP); droplet size distribution (DSD) (and hence the relative dispersion ϵ and total droplet number concentration N_d) was recorded by a Phase Doppler Interferometer (PDI). We intentionally use PDI measurements of the DSD exclusively because this instrument minimizes the coincidence errors that are known to exist with other common DSD instruments and can cause undercounting in number, overestimation of the size, and overestimation of the relative dispersion (Chuang et al., 2008). The PCASP records the number concentration of aerosol particles with diameters of 0.1 – 3 μm. Data is reported at 1 Hz.

Table 2.2. Summary of the Investigated Campaigns.

Abbreviation	Name	Time	Location	Cloud type	Sample size (# flights/ascents)
VOCALS-Rex (Zheng et al., 2011)	VAMOS Ocean-Cloud-Atmosphere-Land Study-Regional Experiment	10/16/2008 – 11/13/2008	Off the coast of northern Chile	Stratocumulus	11/16
MASE (Lu et al., 2007)	The Marine Stratus/Stratocumulus Experiment	7/2/2005 – 7/17/2005	Off the coast of Monterey, California	Stratus/ Stratocumulus	4/6
POST (Carman et al., 2012)	Physics of Stratocumulus Top	7/14/2008 – 8/15/2008	West coast of California	Stratocumulus	16/16
ORACLES (Redemann et al., 2020)	ObseRvations of Aerosols above CLouds and their intEractionS	08/2016 – 09/2016, 08/2017	Southeast Atlantic	Stratocumulus / some Cumulus	10/20
GoMACCS (Bates et al., 2008)	Gulf of Mexico Atmospheric Composition and Climate Study	07/2006 – 09/2006	Texas - northwestern Gulf of Mexico	Cumulus	14/21

Note. In the column of sample size, the number of ascents represents a survey of multiple (cumulus) clouds for the campaign of GoMACCS, while one ascent means a survey of only one (stratocumulus) cloud for the rest of the campaigns.

2.3 Inter- and Intra-Cloud Correlation

Aside from $N_{a,i}$ and N_d, we also calculate the total aerosol number concentration (of particles with diameters greater than 0.1 μm) $N_a = N_d + N_{a,i}$ by assuming that each droplet contains one aerosol particle. We think this is a reasonable assumption given the small droplet size across all campaigns we analyze – the vast majority ($>$ 95% by number) have a diameter less than 25 μm. We also introduce the local activation fraction (LAF). In principle LAF is defined as the ratio of local droplet concentration to maximum activatable cloud condensation nuclei (CCN) concentration given the environmental moisture and updraft profile. By this definition, the maximum LAF would be 1 somewhere in the cloud. In practice there is no easy way to calculate LAF with this definition. Instead, here we define LAF as N_d/N_a (which is the same as $N_d/(N_{a,i} + N_d)$) similar to what was done by Gillani et al. (1995). This equation approximates our ideal definition under the assumptions that a) 0.1 μm (minimum detectable particle size for PCASP) is roughly the smallest unactivated in-cloud equilibrium size for an aerosol particle that could serve as a CCN in the sampled clouds, and b) all aerosol particles between 0.1 and 3 μm are activatable. Of these two assumptions, (a) undercounts maximum activatable CCN and (b) overcounts it. Note that $N_{a,i}$ is non-zero at all cloudy points in all campaigns except VOCALS (where LAF is > 0.99 at a mere 0.03% of data points) which suggests that the undercounting due to the first assumption is not large. Finally, note that variability in N_a is small and the maximum LAF in all campaigns is at least 0.9 which suggests that the overcounting of CCN is also not large. Although this approximation of LAF seems to be acceptable for the campaigns we chose to analyze, we would advise caution before using the same approximation for observational studies in which the maximum LAF is much lower than 1.

We investigate the correlation between relative dispersion ϵ and three quantities: total aerosol number concentration N_a, N_d, and LAF, from two perspectives: inter-cloud (correlation among different clouds) and intra-cloud (correlation of different sampling volumes within a cloud). More specifically, for inter-cloud correlation, we split each flight into separate ascents from cloud base to cloud top (only one ascent in most flights, see Table 2), take the mean ϵ of each ascent and check if there exists any correlation with ascent-mean N_a, N_d, or LAF. For the inter-cloud correlation of N_a, to ensure that the mean aerosol concentration is representative of the boundary layer without much influence from the free troposphere, we only take measurements from the lower half of each cloud. For intra-cloud correlation, we simply look for any local correlation between ϵ and other cloud properties sampled at a frequency of 1 Hz within each cloud as we are interested in any processes, microphysical or dynamical, that can change the local relative dispersion.

The raw data are further subsampled to account for the different sampling strategies implemented by each campaign. For example, the flights in VOCALS and MASE took an unbiased survey across the vertical extent of the clouds using level flight legs, whereas the sampling strategy in POST emphasized the cloud top and used a sawtooth flight pattern. ORACLES and GoMACCS did not always capture the full vertical extent of the clouds. To make sure that certain levels of the cloud are not grossly overrepresented, we set a maximum subsample size N_T/n_l for each layer of the cloud, where N_T is the total number of data points collected in this cloud, and n_l is the number of layers (20) we set for the cloud.

Figure 2.1 shows the $\epsilon - N_a$, $\epsilon - N_d$, and $\epsilon - LAF$ inter-cloud correlation. Ascents with fewer than 25 data points were discarded. We observe no clear inter-cloud correlation between cloud-mean relative dispersion and any of the three cloud properties of interest (N_a, N_d, and LAF), either within a campaign or across different campaigns. MASE is the only campaign that shows high correlation between mean relative dispersion and N_a, N_d, and LAF. It is also the campaign with the fewest flights and lowest range in aerosol concentration which minimizes the importance of the correlations. The lack of consistent correlation in the other four campaigns suggests that we cannot infer much information about the cloud-mean relative dispersion of DSDs from the background aerosol number concentration, cloud-mean droplet number concentration, or their ratio. This suggests that the cloud-mean variability in relative dispersion is less controlled by the background aerosol concentration than by meteorological conditions. We suspect this finding explains why many previous studies showed inter-cloud correlation of inconsistent sign (Table 1). Additionally, since all five campaigns used the same set of instruments to measure cloud droplet and aerosol size distribution, this null result is robust to both measurement and sampling.

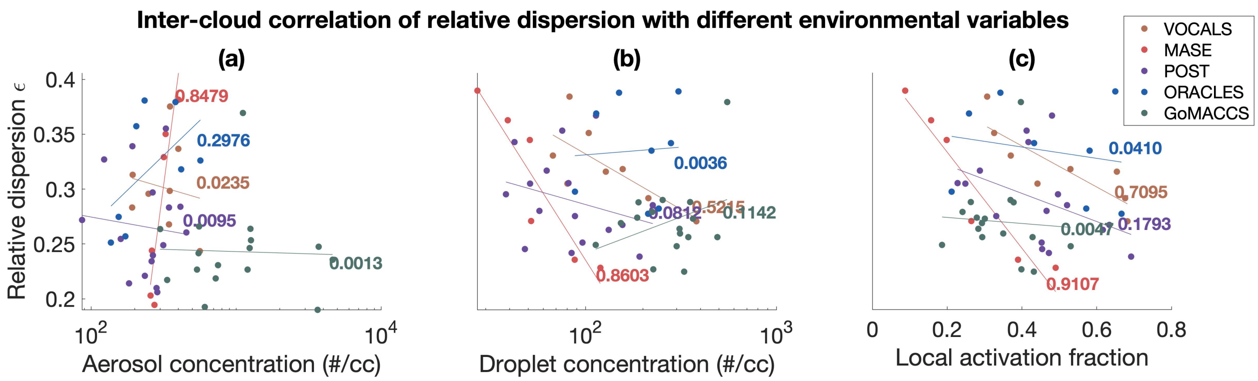

Figure 2.1: Inter-cloud correlation between the flight-mean relative dispersion of DSD and (a) flight-mean aerosol number concentration, (b) flight-mean droplet number concentration, and (c) flight-mean local activation fraction. Each dot represents a cloud-mean datapoint and is color-coded according to its campaign. The correspondingly colored lines are the trendlines for each campaign. The number to the right is the R^2 of the correlation.

Figure 2.2 shows the $\epsilon - N_a$, $\epsilon - N_d$, and $\epsilon - LAF$ intra-cloud correlations for each campaign separately. Clearer $\epsilon - N_d$, and $\epsilon - LAF$ correlations are visible in this figure particularly for VOCALS and MASE and to a lesser extent for POST. In all campaigns, N_a alone does not correlate well with ϵ, which is to be expected since the total aerosol number concentration should not have substantial spatial variation in a well-mixed boundary layer (J. Wang et al., 2007). $\epsilon - N_d$ has stronger correlation but the variability is large for low N_d and low ϵ. However, we see a significant $\epsilon - LAF$ correlation (recall LAF is N_d locally nondimensionalized by N_a) for all three stratocumulus campaigns. Note that, for the $\epsilon -$

LAF correlation, the uncertainty is consistent for the entire range of LAF. We suspect the reason of this negative correlation is that the regions with higher LAF tend to be more adiabatic, associated with a history dominated by updrafts, and thus more likely to retain the narrowing effect (i.e., lower ϵ) from condensation. This is supported by the observations when comparing adiabatic fraction (ratio between observed LWC and adiabatic LWC) against LAF (Figure 2.3). On the other hand, regions with lower LAF might be subject to more turbulent mixing and entrainment which would tend to increase the distribution width. LAF is also by definition partially controlled by N_a. In all three campaigns showing a negative $\epsilon - LAF$ correlation, the aerosol concentration variability is low (not shown). The variability of LAF, at least in this study, is therefore mostly controlled by the dynamics and non-aerosol microphysics and not by heterogeneous aerosol concentrations. Whether the $\epsilon - LAF$ correlation would be altered in highly heterogeneous aerosol concentrations should also be investigated.

Similar results can be found in the simulation work done by Igel and van den Heever (2017), where they showed a negative $\epsilon - N_d$ and $\epsilon - N_{d,scaled}$ correlation. Their scaled droplet concentration ($N_{d,scaled}$) is similarly defined as LAF except that it is normalized by the global maximum of N_a, rather than by the local N_a. If N_a is spatially homogeneous, then these two methods of scaling are identical. Finally, note that since high LAF is by definition correlated with low $N_{a,i}$, this negative $\epsilon - LAF$ correlation is consistent with positive $\epsilon - N_{a,i}$ correlation found by Y. Wang et al. (2021).

As mentioned, among the five campaigns studied, VOCALS and MASE show the strongest intra-cloud correlations. The reasons are not entirely clear. One possibility is that full sampling of the cloud from cloud base to cloud top, like was done in VOCALS and MASE, might be necessary to reveal the full range of the effect. POST shows a worse correlation perhaps because most of the measurements are biased towards the cloud top layer, and as we will show in Section 4.2, the relative dispersion depends on altitude. ORACLES and GoMACCS also show no significant correlation. This could also be due to not having the complete information of the vertical span of the clouds or it may more fundamentally indicate that the relationship of droplet relative dispersion to other microphysical properties varies between cloud types.

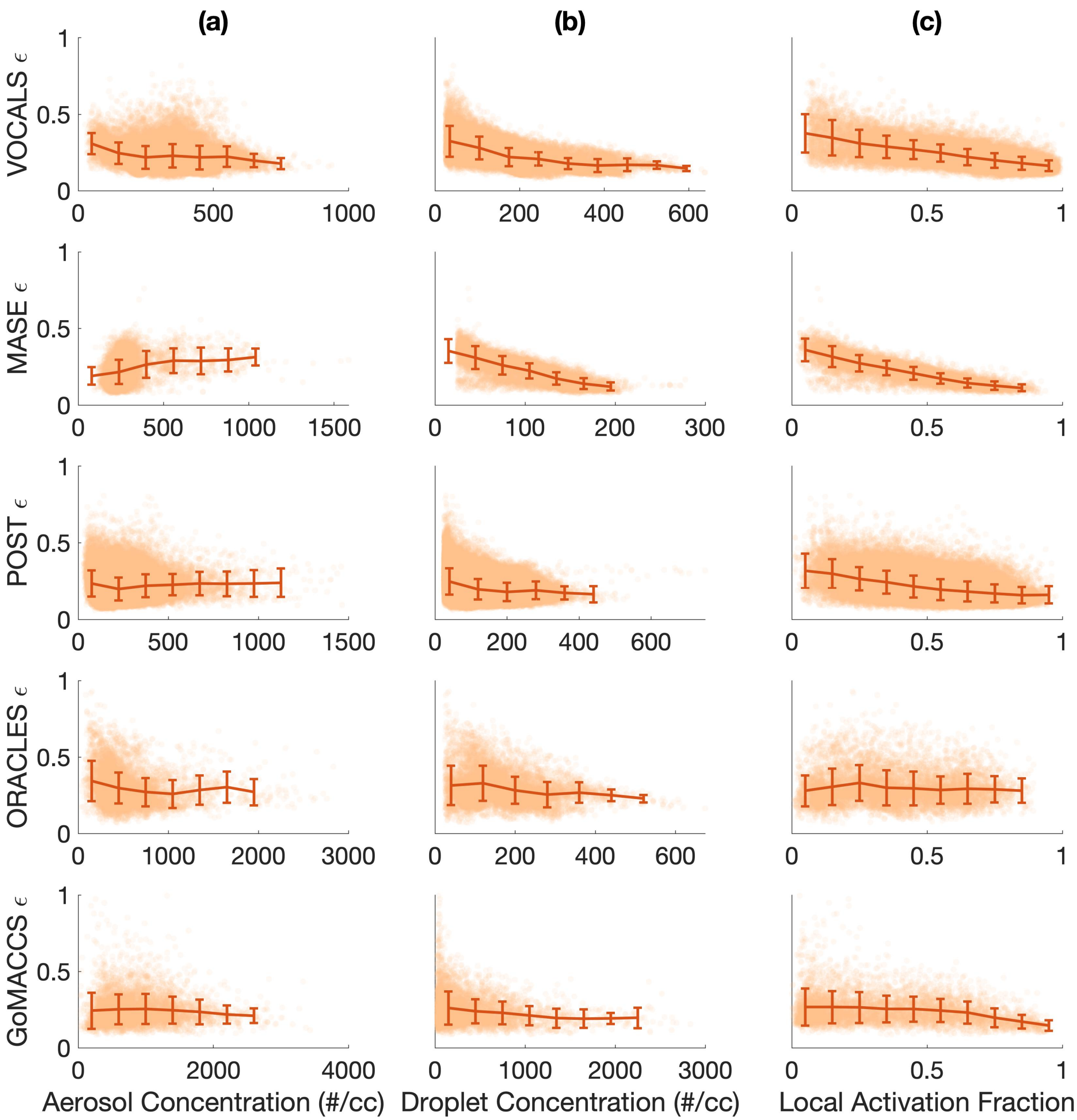

Figure 2.2: Intra-cloud correlation between the relative dispersion of DSD and (a) N_a, (b) N_d, and (c) LAF. Each transparent dot represents a data point. Mean and standard deviation of relative dispersion are calculated at each decile of the independent variable.

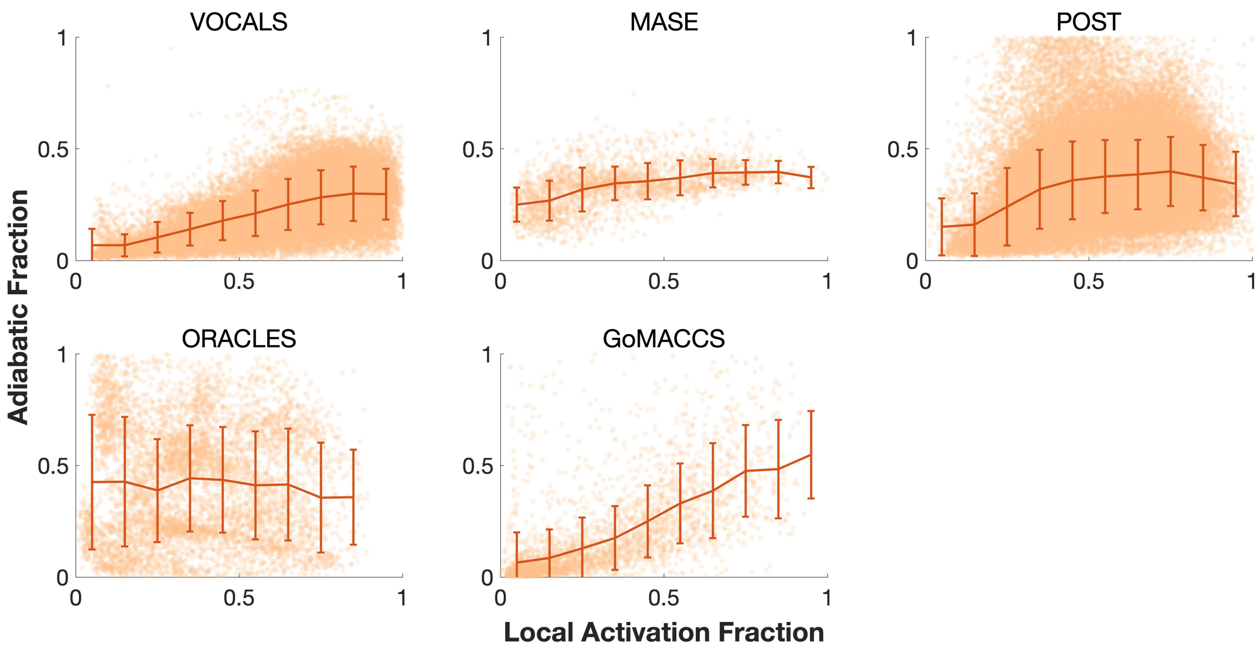

Figure 2.3: Scatter plot of adiabatic fraction and local activation fraction. Mean and standard deviation of adiabatic fraction are calculated at each decile of LAF. Datapoints with AF > 1 are not shown for POST, ORACLES, and GoMACCS, which is partly due to the difficulty of identifying the lifting condensation level.

2.4 Diagnosing Relative Dispersion

To estimate local relative dispersion, we perform systematic assessment of which combination of cloud properties best diagnoses the relative dispersion of the DSD. We diagnose ϵ using multivariate linear regression. Five potentially relevant cloud properties are used as predictors: N_d, LAF, liquid water content (LWC), normalized height above cloud base (NH), and AF. NH is defined as the ratio of the distance above the cloud base to the thickness of the cloud

$$NH = \frac{z - z^b}{z^t - z^b}, \tag{2.1}$$

where z^b and z^t represents the altitude of the cloud base and cloud top. NH and AF are included here as they have previously been shown to correlate with ϵ (Jia et al., 2019; M.-L.

Lu et al., 2007; Stevens et al., 1996). Although several studies (Jia et al., 2019; C. Lu et al., 2012; Yang Wang et al., 2021) have suggested a causal relation between vertical velocity (w) and ϵ, it is not included in the predictor sets because the direct correlation between w and ϵ is too weak for w to be a predictor. We suspect this absence of a direct $w - \epsilon$ correlation is because ϵ is controlled by the integrated history of vertical motions (and other factors) but w is only an instantaneous quantity. We refer the interested readers to the supplemental information (Section 2.7, Figure 2.7 and Figure 2.8) for an explicit $\epsilon - w$ scatter plot and how w affects the correlation between ϵ and other cloud properties.

Rather than simply assuming using all the predictors will provide the best model, we systematically test all combinations of predictors to avoid mutual dependence (as between LAF and AF shown in Figure 2.3). From our five physical variables, 31 combinations (a.k.a., "predictor sets") can be generated. Each predictor set is then used to model the relative dispersion using multivariate linear regression.

2.4.1 Methods to Assess the Predictor Set

For a given campaign, a set of regression coefficients can be obtained for each predictor set and each flight ascent. For example, if we try to use a predictor set {A,B} to model the relative dispersion for each cloud ascent, and twenty ascents were conducted in a given campaign, we would have 20 sets of regression coefficients, each with three parameters: an intercept term (p_0), a coefficient for A (p_A), and a coefficient for B (p_B).

We can analyze the effectiveness of each of the 31 predictor sets with two different metrics. One metric, which we call "consistency" K of the predictor set, is how little the set of regression coefficients changes across different flight ascents given a predictor set. Higher values of K indicate that the regression coefficients are more similar across the campaign.

The other metric, which we call predictability Π, is how accurate the predicted relative dispersion $\hat{\epsilon}$ is compared to the measured dispersion ϵ. The definition of predictability Π is like that of R^2 (coefficient of determination) of a correlation, but we obtain $\hat{\epsilon}$ in two ways. The first uses the cloud regression coefficients to predict the relative dispersion in the cloud itself. In this case, the predictability of a given predictor set is dubbed as the specialized predictability Π_s. The other prediction method uses the campaign-mean regression coefficients, and this predictability is dubbed as the campaign-predictability Π_c. Additionally, the calculation of Π_c is slightly different from Π_s: only 70% of the dataset is randomly selected as the training set and used to obtain the campaign-mean regression coefficients, which are then applied to the remaining 30% (test set) and used to calculate the campaign predictability Π_c. This 70%-30% divide is to check if there is any overfitting. This also means that Π_c can be smaller than 0 since the regression coefficients are applied to a different set of data from which they are originally obtained. See the Appendix (Section 2.6) for how consistency and predictability are obtained mathematically.

2.4.2 Results

Figure 2.4 shows K and Π of all 31 predictor sets for all five campaigns. Each of the 31 pie graphs below the x-axis represents a combination of the five predictors. The "best" predictor set (with highest overall consistency and predictability) for each campaign is highlighted. The best predictor set and the corresponding campaign-mean regression coefficients are listed in Table 3.

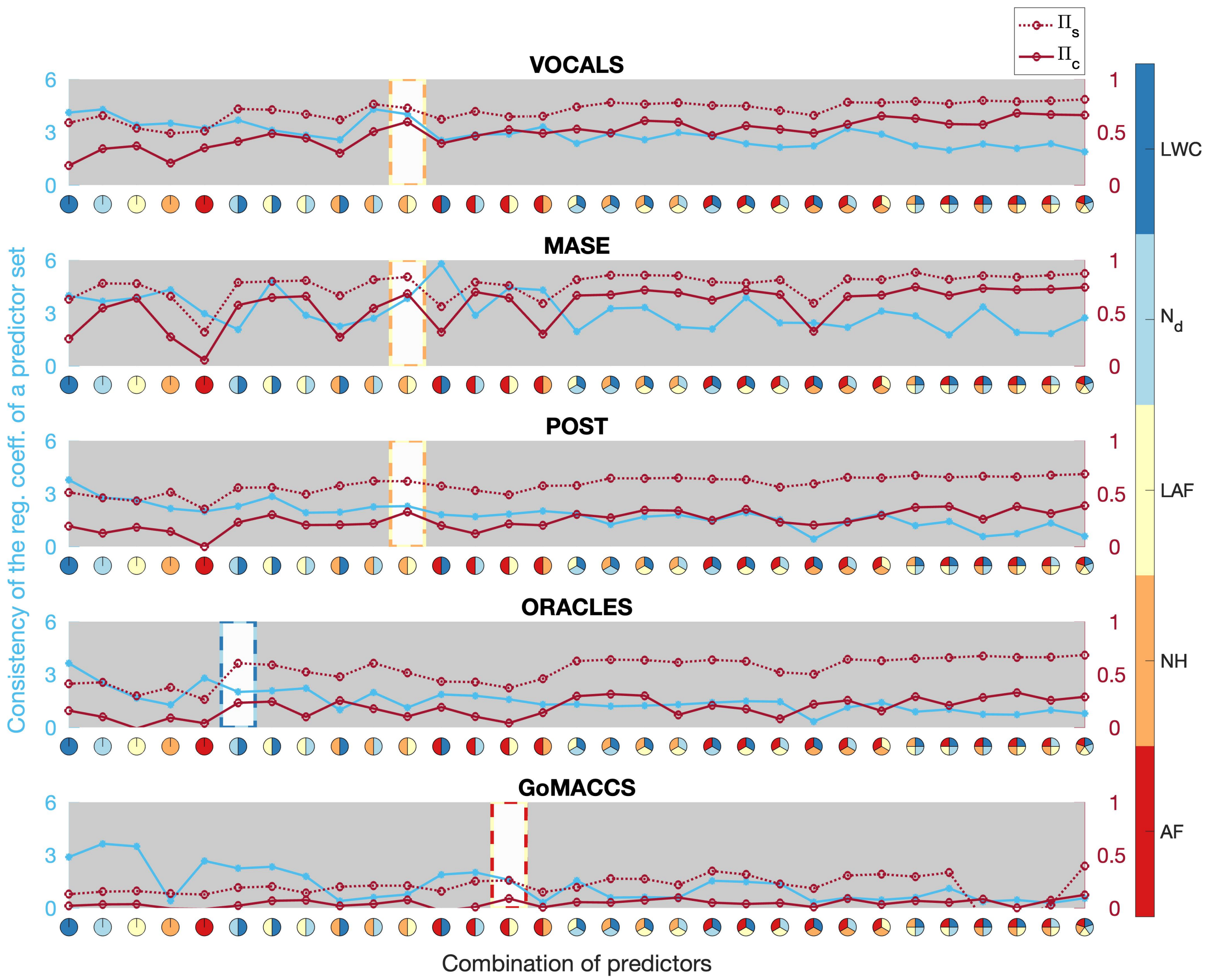

Figure 2.4: The consistency of regression coefficients (blue ∗) and predictability (red ∘) of each predictor set. Note that the best predictor set (highlighted) for the three stratocumulus-dominated campaigns are chosen to be the same one for the sake of a unified diagnostic equation for stratocumulus clouds.

The predictor set of $\{LAF, NH\}$ has the best overall performance for VOCALS (Figure 2.4), POST, and MASE. The optimal predictor set for ORACLES is $\{N_d, LWC\}$, which performs well for individual clouds with a Π_s of ~0.7. Unfortunately, all predictor sets for

ORACLES suffer from overfitting and lack of general predictability. No predictor set appears to diagnose relative dispersion in GoMACCS with a predictability higher than 0.4. A few reasons why neither LAF nor NH works well as a predictor are that a) high aerosol loading leads to overall low LAF, causing the signal to be overwhelmed by the noise; b) the estimation of NH is too simple as cumulus cloud tops are generally not horizontally homogeneous. For the sake of completeness, we choose $\{LAF, AF\}$ as the optimal predictor set of GoMACCS, but this set does not make a particularly good model.

Figure 2.5 shows the agreement between the measured relative dispersion and the campaign-prediction of relative dispersion using the best predictor set for each campaign (specialized prediction not shown). As part of the goal of this study is to propose an alternative diagnostic equation for the relative dispersion, it is necessary to look at the predictability even beyond the campaign level. We therefore combine the data points from all the stratocumulus-dominated campaigns (VOCALS, MASE, and POST where each campaign is equally sampled) and perform an aggregated multivariate linear regression to predict local relative dispersion. We find a meaningful predictability (Π_{Sc}) of $\sim$0.50 with the equation

$$\hat{\epsilon} = 0.386 - 0.184 \cdot LAF - 0.115 \cdot NH, \tag{2.2}$$

where the 95% confidence interval of each coefficient is $(0.382, 0.391)$, $(-0.191, -0.177)$, and $(-0.121, -0.110)$. This suggests that such correlation holds for marine stratocumulus clouds across different campaigns. The equation gives a lower limit for relative dispersion of 0.087 (when LAF and NH are both 1), which corresponds to a nearly monodisperse distribution and gives an upper limit of 0.39. (Note that most microphysics schemes assume a gamma DSD with a shape parameter μ that is related to ϵ by $\mu = \frac{1}{\epsilon^2} - 1$. This equation gives a lower limit on μ of about 5.5.) This upper limit seems reasonable for the clouds that were sampled here but may be too low in precipitating clouds. More in-situ data on precipitating clouds might be needed to account for the scenarios with $\epsilon > 0.4$. Nonetheless, as mentioned previously, most existing diagnostic equations for ϵ are based on the inter-cloud perspective and give the wrong sign of correlation between ϵ and N_d. This equation, which is constructed from an intra-cloud perspective, is more appropriate than these previous diagnostic equations for models that explicitly resolve stratocumulus clouds and should represent an improvement.

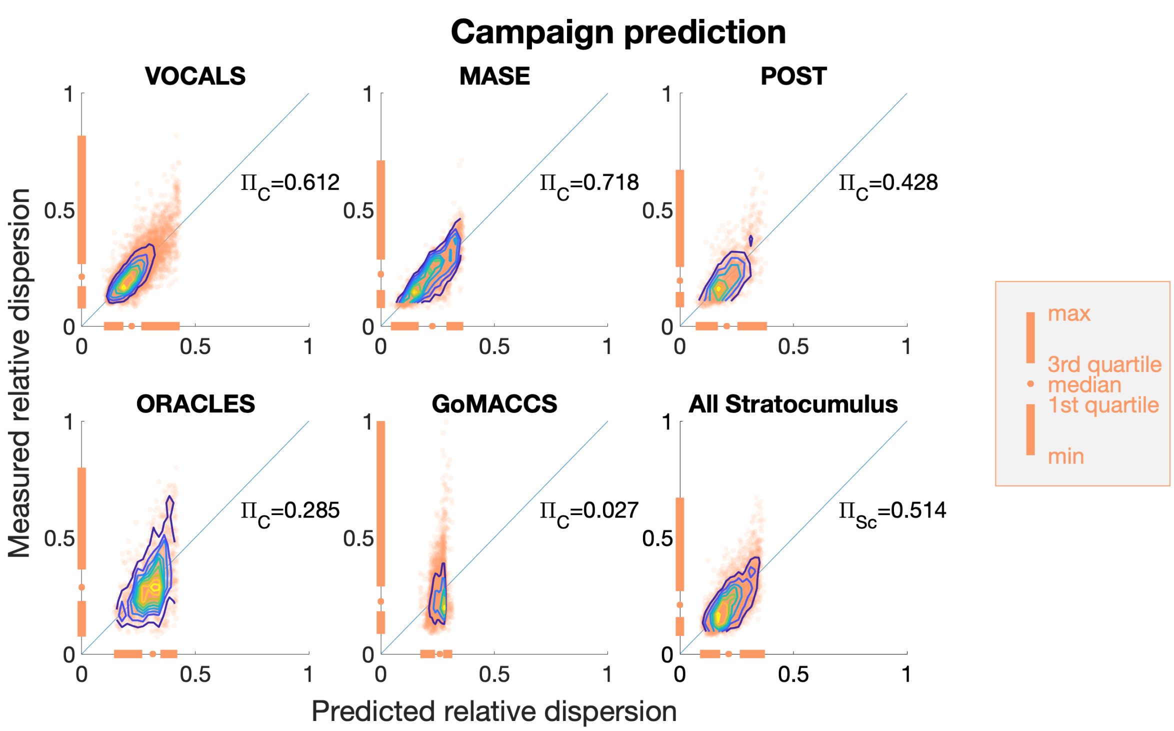

Figure 2.5: Campaign predictions, i.e., the campaign-mean regression coefficients are used to diagnose the relative dispersion of DSD in each cloud. The set of predictors used for each campaign is {LAF, NH} for VOCALS, MASE, and POST; {N_d, LWC} for ORACLES; {ER, NH} for GoMACCS. Contour plots represent the density of the datapoints. The thick orange lines and dots on the axes are the quartile plots of the data, from which the distribution of predicted and measured relative dispersion can be inferred.

Table 3: The Campaign-Mean Regression Coefficients and the Campaign-Predictability for the Optimal Predictor Set.

	Int	LWC	N_d	LAF	NH	AF	Π_c, Π_{Sc}
VOCALS	0.460			-0.215	-0.152		0.612
MASE	0.386			-0.304	-0.0618		0.718
POST	0.381			-0.180	-0.133		0.428
ORACLES	0.426	-0.238	-2.25×10^{-4}				0.285
GoMACCS	0.284			-0.111		-0.0331	0.027
All Sc.	0.386 $\pm$ 0.048			-0.184 $\pm$ 0.007	-0.115 $\pm$ 0.0057		0.514

Note. "Int" represents the intercept term. The last row corresponds to the coefficients and predictability for all stratocumulus campaigns. A 95% confidence interval are shown for each coefficient for the all-stratocumulus linear regression.

2.4.3 Analysis on Scale Dependence

As atmospheric models can operate on a wide range of resolution, it is also valuable to perform an analysis of the predictability of ϵ on different length scales and of the consistency of the coefficients in the diagnostic equation. We test a range of length scales from ~50 m to ~50 km by taking the average of the in-situ measurements that are used in the aforementioned regression model. Note that the average of dimensionless variables (LAF, ϵ, etc.) are obtained by separately calculating the average of numerators and denominators before taking the ratio. Like in Figure 2.4, the Π_{Sc} at different length scales are also obtained from the 30% test set that is not used to generate the model. As random sampling is involved, twenty trials are run for each length scale level, and the mean and standard deviation of the Π_{Sc} and the coefficients are shown in Figure 2.6.

We find that the Π_{Sc} is greater than 0.45 for length scales from 50 m (resolution of the in-situ measurements) up to 10 km, and quickly fall to near 0 for length scales larger than 30 km (Figure 2.6a). Figure 6b also shows that the coefficients of the diagnostic equation remain roughly unaltered from 50 m to 1 km. This gives us hope that a diagnostic equation like Eq. 2.2 can be adopted for bulk microphysics schemes in both cloud-resolving and large-eddy models. The peak of Π_{Sc} at length scale of 1 km is likely due to the smoothing effect of averaging, leaving more signal than noise in the averaged data. In addition, the low Π_{Sc} for length scales close to an entire cloud ($>$ 30 km) is also consistent with our discovery of the lack of inter-cloud correlation as discussed in Section 2.3.

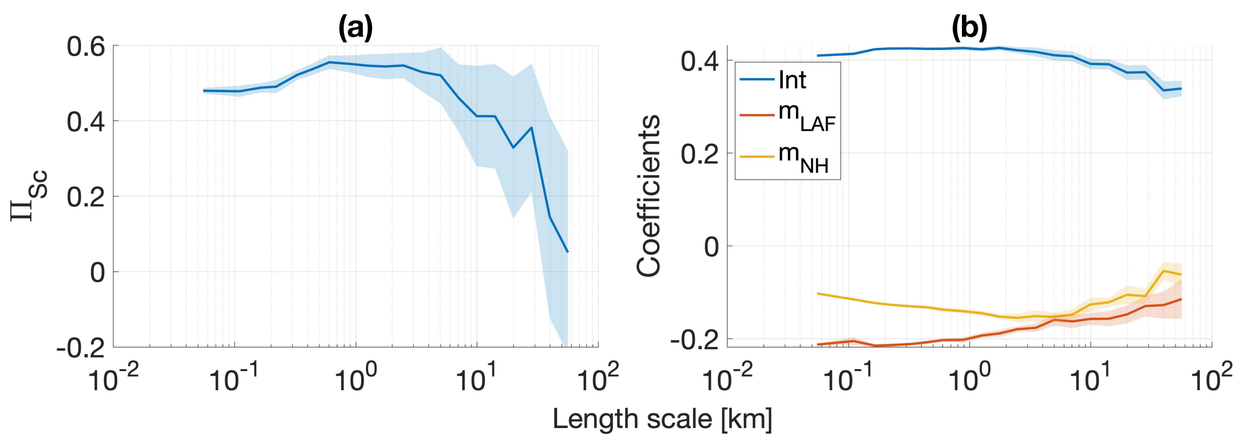

Figure 2.6: Scale dependence of (a) predictability of ϵ in stratocumulus-dominated campaigns; (b) coefficients of the diagnostic equation. The solid lines are the mean values of 20 trials with random sampling, and the shaded regions are the standard deviation. The length scale is calculated by multiplying the flight speed (55 m/s) by the time over which the measurements are averaged.

2.5 Summary and Discussion

The goal of this study is to understand the relationship between the relative dispersion of the cloud droplet size distribution and other cloud properties. The correlation between any two properties can be quantified from two different perspectives: inter-cloud and intra-cloud. Contrary to previous studies, we find that the inter-cloud correlation between relative dispersion and aerosol or droplet concentration is not statistically significant, suggesting that the background aerosol concentration does not have a dominant control on the cloud-mean relative dispersion of DSD. This finding is perhaps a reason why previous studies have reported such contradictory results, although meteorological controls may also be important for the sign of the inter-cloud aerosol-dispersion relationship. On the other hand, although the intra-cloud $\epsilon - N_a$ and $\epsilon - N_d$ correlations are still minimal, the $\epsilon - LAF$ correlation is notably more significant, at least for the stratocumulus dominated campaigns (VOCALS, MASE, and POST), indicating that in-cloud physical processes could mediate the magnitude of ϵ. We find that a lower ϵ can be expected in regions with higher LAF. We believe this is due to regions with high LAF usually being associated with updrafts containing condensationally-narrowed droplet distributions. Low ϵ being associated with updraft was also found in an observational study of Southern Ocean stratocumulus clouds, albeit only when aerosol loading is low (Yang Wang et al., 2021), in cumulus clouds (Lu et al., 2012), and theoretically based on parcel model simulations (Chen et al., 2016). Additionally, a positive correlation between LAF and adiabatic fraction (as a measure of the degree of mixing) suggests that turbulent mixing could promote the broadening of droplet spectra, which agrees with past modeling studies (Abade et al., 2018; Lasher-Trapp et al., 2005; Lu & Seinfeld, 2006; Noonkester, 1984).

We also find local ϵ to be associated with normalized height with a slightly weaker negative intra-cloud correlation, while the standard deviation of the DSD remains roughly constant with height despite the increase in mean droplet size (not shown). This observation is in agreement with Lu et al. (2007) who suggest the dependence on normalized height is due to cloud base mixing and updraft velocity variance. Other observational (Noonkester, 1984) and modeling (Lu & Seinfeld, 2006; Stevens et al., 1996) studies have shared similar results. Specifically, all of them showed a nonmonotonic vertical profile of ϵ with maxima at the cloud base and top (smaller than the cloud base maximum), and a minimum in the mid-cloud regions. They also attribute the increase in dispersion at the cloud top and base to vertical and turbulent mixing. Additionally, Stevens et al. (1996) showed that the sampling strategy adopted by Noonkester (1984) can cause the cloud-edge maxima of ϵ to be reduced by a factor of $1/2$ in the observations. Of the campaigns analyzed in this study, VOCALS and MASE have a similar sampling strategy to the campaign studied in Noonkester (1984), which is likely one reason why we could not see a local maximum of ϵ at the cloud top.

This apparent distinction between the two perspectives underscores the need for caution when using cloud-resolving models and large eddy simulation that use two-moment bulk microphysics schemes. The diagnostic equation for relative dispersion should be based on the intra-cloud correlation because the clouds are individually resolved in these simulations. Here, we propose an equation for diagnosing relative dispersion within a stratocumulus cloud using the information of LAF and NH (Eq. 2.2), both of which are known or can easily be calculated in many two-moment bulk schemes. Upon investigating the length scale dependence of this diagnostic equation, we find both the predictability of ϵ and the consistency of regression coefficients remain high (> 0.45) at length scales between $\sim$50 m and $\sim$10 km. This suggests that the diagnostic equation can be applied to bulk microphysics schemes in models with different preferred resolution settings, from cloud resolving models to large-eddy simulations. However, this equation should be used with caution since it cannot predict any relative dispersion value greater than $\sim$0.4 (or a gamma DSD shape parameter less than 5.5) and can limit the maximum width predicted by the bulk scheme. This upper limit of relative width of distribution could potentially slow down precipitation formation (if it is accounted for in the autoconversion parameterization), and this cannot be addressed by this study as all the clouds we analyzed are nonprecipitating with only a few datapoints having their $\epsilon > 0.4$.

Further observational studies on drizzling stratocumulus clouds may be needed to extend this upper limit. Nonetheless, we feel that the present diagnostic equation is an improvement over previous diagnostic equations that have been used in cloud-resolving microphysics schemes. Further studies are also needed to investigate the physical processes controlling relative dispersion in clouds, particularly cumulus clouds, and the relationship between relative dispersion and other local cloud properties. Finally, similar analysis should also be performed to study the controls on droplet concentration. Since droplet concentration and relative dispersion are closely tied, such analysis may provide additional insights into the relative dispersion as well.

2.6 Appendix

With an arbitrary predictor set {A,B} for a campaign with 20 clouds surveyed, we quantitatively evaluate the invariability of regression coefficients by defining the individual consistency of predictor A as $\kappa_A = \frac{\mu_A}{\sigma_A}$, where μ_A and σ_A are the mean and standard deviation of the linear coefficient of A (p_A) across all 20 clouds. Note that this individual consistency is the inverse of $\frac{\sigma_A}{\mu_A}$, or the relative dispersion of p_A; the term "relative dispersion" is avoided here to prevent potential confusion with the ϵ of the DSD while also giving the concept of consistency a positive tone – larger values are better. We then define the bulk consistency for the entire predictor set {A, B} as $\mathrm{K}_{A,B} = \overline{\boldsymbol{\kappa}} = \frac{1}{3}(\kappa_0 + \kappa_A + \kappa_B)$. More generally, the consistency for any one predictor set P out of the 31 predictors is defined as $\mathrm{K}_P = \overline{\kappa}$. With this K_P for each predictor set, we can quantitatively compare which predictor set has the best consistency in its regression coefficients and is thus more generalized and can be applied under different circumstances.

To quantitatively evaluate the accuracy of the prediction, we define the predictability as $\Pi = 1 - \frac{\Sigma(\hat{\epsilon}-\epsilon)^2}{\Sigma(\epsilon-\overline{\epsilon})^2}$, where $\hat{\epsilon}$ is the predicted value of relative dispersion, and $\overline{\epsilon}$ is the mean observed value. This is slightly different from the definition of the R^2 of two correlating variables since the predicted relative dispersion $\hat{\epsilon}$ might not lie in the same range as the measured ϵ.

2.7 Supplemental Information

We find the vertical velocity w in the campaigns investigated in this study to be similar to what was shown in Jia et al. (2019). Specifically, the central panel of Figure 2.7 is a scatter plot showing the relationship between ϵ and LAF and colored by vertical velocity, similar to what was done in Jia et al. (2019). Updrafts appear to be associated with low ϵ, and vice versa for downdrafts. However, when the $\epsilon - w$ correlation is plotted explicitly (left panel of Figure 2.7), we find that they are in fact not strongly correlated and w is thus not useful for diagnosing ϵ, which is one of the focuses of this study. In addition, this relatively weak association is only found to exist in VOCALS on a day-to-day basis but not in aggregate, and no association at all was found for POST, ORACLES, and GoMACCS (w data are not available for MASE). The right panels of Figure 2.7 shows the $\epsilon - LAF$ correlation as colored by NH.

It is obvious that ϵ is jointly controlled by both LAF and NH (overall lower ϵ for higher NH and higher LAF). The effect of w on the correlations between ϵ and other variables (N_a, LAF, AF, and LWC) for all applicable campaigns are shown in Figure 2.8. Vertical wind velocity again does not appear to significantly alter these relationships.

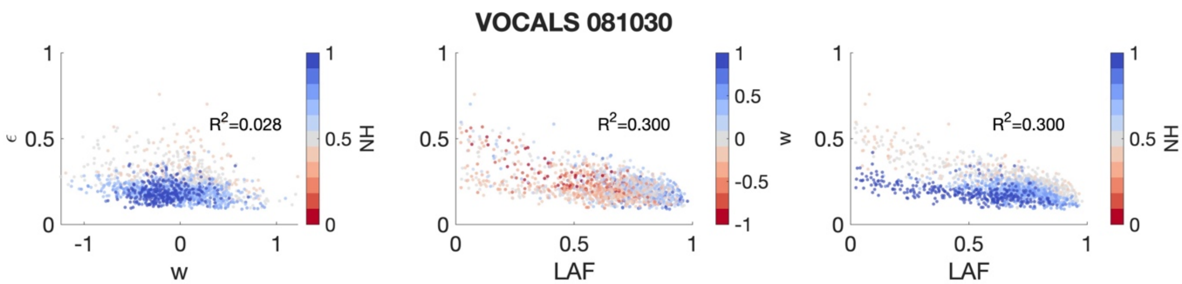

Figure 2.7. Direct w — ϵ and LAF — ϵ correlation. The right two panels are the same except the middle panel is colored by vertical velocity and the right is colored by normalized height. The data is from VOCALS Twin Otter research flight on 10/30/08.

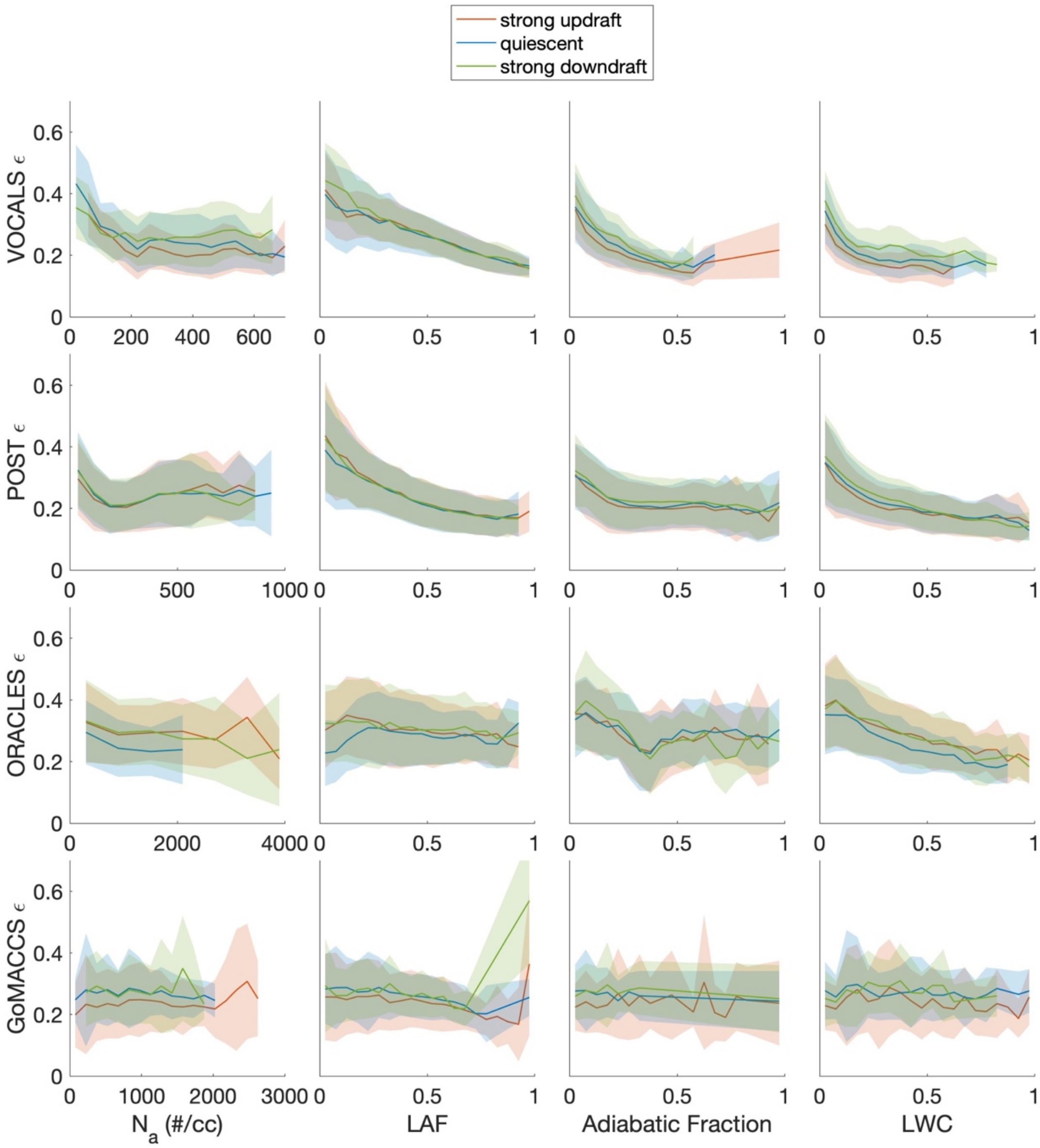

Figure 2.8. ϵ vs. N_a, LAF, AF, and LWC with different vertical wind condition. Strong updraft and downdraft are defined as regions with wind velocity higher than the 80th percentile or lower than the 20th percentile of the campaign. "Quiescent" represents the 40th to 60th percentile. The shaded regions are the standard deviation.

3 Bin vs. Bulk Microphysics Scheme

3.1 Background

Modeling clouds is hard. As noted in great detail in Morrison et al. (2020), the two biggest obstacles are a) the sheer number of cloud and precipitation particles to predict and b) the lack of the fundamental understanding of microphysical processes involved. With quintillions of droplets in a typical cloud, it is infeasible to predict the evolution of each droplet and its environment. In addition, there does not exist a fundamental governing equation or benchmark model that can help inform the modeling of microphysics in larger scale, unlike other subgrid physical processes such as radiation, turbulence, and convection. Clouds are thus only modeled from a macroscopic perspective with its parameterizations determined empirically. Aside from the more recently developed Lagrangian superdroplet method (e.g., Shima et al., 2009), the two most well-established microphysics scheme types are the bulk microphysics scheme and the bin microphysics scheme. Bin schemes keep track of the number of droplets of within discrete size or mass ranges (i.e., size-resolved or mass-resolved), allowing the particle size distribution (PSD) to evolve freely but is therefore computationally expensive (A. P. Khain et al., 2015). On the other hand, bulk schemes predict quantities proportional to moments of the PSD (i.e., moment-resolved), typically mass and number concentration (e.g., Kessler, 1969; Lin et al., 1983; Meyers et al., 1997). Albeit not a required feature for bulk schemes in principle, they also typically have a separate liquid water category (cloud mode and rain mode) and prescribe a gamma probability distribution function (PDF) for the PSD, which is less flexible than bin schemes but computationally efficient enough to model large-scale weather systems and global climate. This difference in PSD treatment between the two is known as their structural difference. In practice, however, they are also different on another level – how physical processes and properties are parameterized (A. P. Khain et al., 2015). This includes terminal velocity-diameter relationships, mass-diameter relationships, the collision-coalescence parameterization, the droplet activation parameterization, the condensation formulation, etc. Since the parameterizations are not easily convertible from one scheme to another, separating the importance of these two types of difference has been difficult. In this study, we aim to isolate the structural difference from the parameterization difference between bin and bulk schemes.

Although there has been a great number of studies that compared bin and bulk schemes, their objectives are mainly to assess the advantages and disadvantages of *existing* schemes (Fan et al., 2012, 2016; Li et al., 2009; Seifert & Beheng, 2006a, 2006b). In these studies, the explanation for the difference between simulations performed by bin and bulk schemes are almost never related to their structural difference. Instead, it was pointed out that the possible reasons could be a) the lack of inclusion of an aerosol budget, b) wide adoption of saturation adjustment, and c) parameterization of autoconversion that was derived under a narrow range of conditions (Fan et al., 2016). Despite being valuable addition to our knowledge of the existing models, none of these studies mentioned the relative importance of a model's structure and parameterization choices on the final prediction. However, it is well known that microphysics parameterization choices can have a large impact on simulations. For example, in an idealized supercell simulation, Falk et al. (2019) found that the terminal speed parameterization is a greater factor in determining how a supercell splits than the choice of a bin vs bulk microphysics scheme. Another study by Johnson et al. (2015) showed that the accumulated precipitation from a deep convective cloud can vary from 0 to 70 mm just by adjusting 11 cloud and aerosol parameters within physically reasonable ranges within a single bulk scheme. Parameterization sensitivity is not limited to bulk schemes, especially when ice microphysics is involved. This is because, unlike liquid hydrometeors, ice particles are observed with a variety of shapes and habits in the atmosphere, which poses challenges on predicting how they fall and interact with other ice or liquid particles (Morrison et al., 2020). The case study of a squall line event discussed in Xue et al. (2017) revealed that different bin schemes can behave quite differently regarding reflectivity patterns, cold pool extent, and thermodynamic structure, although many of the differences can be attributed to the ice-phase parameterization. Nevertheless, they showed that the spread among the bin schemes was qualitatively similar to the spread among the bulk schemes tested in Morrison et al. (2015), further hinting that model intercomparisons between bin and bulk schemes should be done carefully. These findings, again, prompt the question, how similar would bulk and bin schemes be if they were only different structurally?

It is a valuable question to ask for two reasons: 1) because knowing how bin and bulk schemes are different structurally can help us understand both the limitation and the true capability of a moment-resolved scheme and 2) it may also give us confidence in the future development of bulk schemes if the bin-bulk differences are found to be small. Additionally, the efficiency of bulk schemes is still required for large scale simulations in the foreseeable future despite the exponential increase in computational power and as such continued improvement of bulk schemes is necessary.

Many efforts have been made towards narrowing down the effect of different microphysics schemes by prescribing a velocity field and disallowing feedbacks from the microphysics. Morrison & Grabowski (2007) compared their two-moment (2M) bulk scheme with a bin model as a benchmark in this way. They found that the simulations performed by bulk and bin schemes were similar for mean effective radius and cloud water path with the bulk simulations having a slightly larger mean effective radius. They also noted that the uncertainty was most likely a result of their relative dispersion diagnostic equation. Shipway & Hill (2012) conducted a similar study. They concluded that the 2M bulk schemes generally perform more similar to a bin scheme than 1M bulk schemes do but produce larger precipitation peaks than any other schemes, which is a result of their excessive size sorting problem. Excessive size sorting is a result of the structure of bulk schemes (Morrison, 2012) and exists in most 2M schemes and can be improved considerably with a three-moment (3M) bulk scheme (J. A. Milbrandt & McTaggart-Cowan, 2010; Jason A. Milbrandt & Yau, 2005; Shipway & Hill, 2012).

Even with the same prescribed dynamics, the different predictions that the microphysics routines in bulk and bin schemes make can still be a combined effect of structure and parameterization. To address this problem, Igel (2019) (hereafter I19) designed the Arbitrary Moment Predictor (AMP) to isolate and compare the effect of structural difference alone. At its core, AMP is a bulk scheme that assumes a gamma PSD and predicts moments, but it uses a bin scheme to do microphysics calculations. The scheme was designed not necessarily to replace existing bulk schemes, but to study the effect of the structural differences between bulk and bin schemes. All differences between simulations with AMP and simulations with its underlying bin scheme can be attributed to structural differences. Igel (2019) performed simulations in an idealized box model with individual processes turned on (condensation, evaporation, and collision-coalescence). In the idealized box model, it was found that AMP could mimic its bin counterpart for condensation and evaporation quite closely, whereas AMP and its underlying bin scheme could produce substantially different evolutions of rain water production during collision-coalescence. Igel et al. (2022) (hereafter I22) further explored the reasons for poor performance of AMP during collision-coalescence.

Following on from I19 and I22, this study increases the complexity from single-process box model simulations to 1D kinematic simulations with all warm phase microphysical processes turned on. The objective of this study is to examine processes not previously discussed in I19 and I22 (droplet activation, sedimentation) and to examine how the interactions between all microphysical processes forced by simplified dynamics magnify (or not) the different performances of bin and bulk schemes due to their structural differences. Although 2M bulk schemes are still the default and AMP can be configured to be either 2M or 3M, simulations tested in this paper will only the 3M AMP because unlike a 2M bulk scheme, a 3M bulk scheme can prognostically evolve the width of the PSD. In this study, we configure AMP to act like a typical 3M bulk scheme in which the 3rd, 0th, and 6th moments of the cloud and rain size distributions are predicted. This moment combination was found to be among the best for 3M schemes for individual processes like condensation, evaporation, collision-coalescence (I19), and sedimentation (J. A. Milbrandt & McTaggart-Cowan, 2010).

The rest of the paper is organized as follows. Section 3.2 briefly explains the mechanics of AMP. Section 3.3 describes the model setup, the simulations with different combinations of microphysical processes, and the range of initial conditions used for these simulations. Section 3.4 presents the results from the simulations. Section 3.5 gives the concluding remarks of the findings.

3.2 Mechanics of AMP: Bin Physics Put into a Bulk Scheme

In order to isolate the structural difference from the parameterization difference between bin and bulk schemes, a hybrid bin-bulk microphysics scheme, AMP, was designed (I19). Figure 3.1 is a conceptual schematic of the procedures of AMP:

1. At the beginning of each time step, parameters of a gamma distribution are diagnosed from the moment values ($M_k{}'$) of a PSD from the last time step.
2. The gamma-shaped size distribution is then discretized.
3. The discretized PSD is passed into bin microphysics scheme routines, which include any combination of condensation, evaporation, collision-coalescence, and/or sedimentation.
4. Moment values (e.g., 3rd, 0th, and 6th) are diagnosed after the microphysics routines complete.
5. These moment values (M_k) are passed into the dynamics routines (advection, divergence, etc.), which is performed by the dynamical core and is not part of AMP. The products are the predicted moment values ($M_k{}'$) for the next time step.

AMP treats each hydrometeor category separately. In this study, we have two hydrometeor categories: cloud and rain, with a diameter threshold of ~80 μm, as adopted by many existing bulk microphysics scheme (Beheng, 1994; Berry & Reinhardt, 1974; Lee & Baik, 2017; Seifert & Beheng, 2001; Yuan Wang et al., 2013), although an alternative threshold of 50 μm will be examined in Section 3.4.4. If there is mass in both categories, their discretized PSDs are concatenated before being passed into the microphysics routine (Step 3).

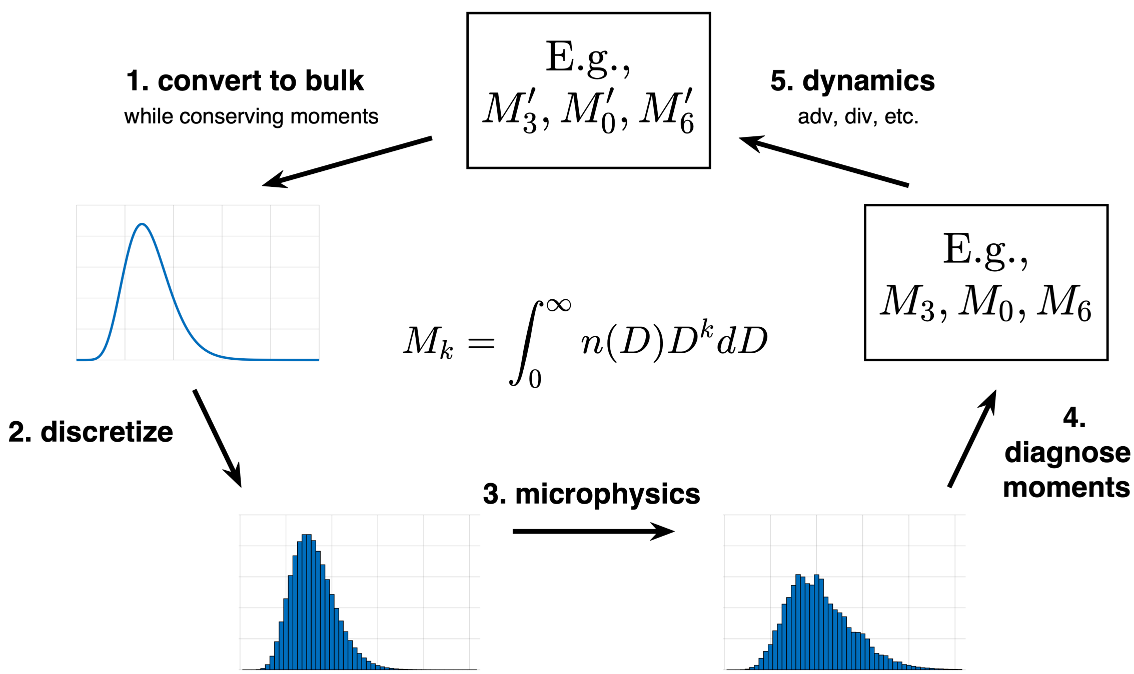

Figure 3.1. The steps taken by AMP to predict the moments of one hydrometeor species. The equation at the center is the definition of k[th] moment. The microphysics processes in Step 3 can include any combination of condensation, evaporation, collision-coalescence, and/or sedimentation. M_k' after Step 5 is the k[th] moment M_k after dynamics is calculated. Note that Step 5 (dynamics) is performed by the dynamical core and is not part of AMP.

Since no single bin scheme is perfect, we implemented two underlying bin schemes into AMP: the Hebrew University spectral bin microphysics (SBM; A. Khain et al., 2004) and the Tel Aviv University (TAU) bin scheme (G. Feingold et al., 1988; Tzivion et al., 1987, 1999). The inclusion of the TAU scheme as an option is new to AMP in this study. The most prominent difference between these two bin schemes is that HU-SBM only predicts the mass for each droplet size bin, whereas TAU predicts both mass and number. The inclusion of two bin schemes allows us to assess the relative importance of the AMP-bin difference compared to the difference between two bin scheme types. All simulation cases in this study are thus performed with four microphysics schemes, which we denote as AMP-SBM, bin-SBM, AMP-TAU, and bin-TAU.

Note that we do not include an aerosol scheme in any test. Rather we specify an aerosol concentration that is a constant and droplet activation is parameterized by calculating the local cloud condensation nuclei (CCN) concentration and comparing it with the local droplet concentration. If the CCN concentration exceeds the droplet concentration, new droplets are formed. The calculation of the CCN concentration is different in the two bin schemes. More information about the representation of this process and all other processes may be found in the references above.

In summary, AMP is structurally a bulk scheme with bin scheme parameterizations. As such, comparing simulations with AMP with its underlying bin scheme sheds light on the structural differences between bulk and bin schemes. With the ability to switch each microphysical and dynamical process on and off, we can pinpoint the specific process in the model that leads to the differences in the simulation results by AMP and bin schemes, which will give us insights into the fundamental limitations of moment-resolved schemes with prescribed functional forms. A more detailed description of AMP can be found in Section 2 and Appendix A of I19.

3.3 Model Setup: 1D Simulations

This study builds on the box model AMP simulations performed by I19 and I22 by incorporating advection into the testing and extending the simulation into a 1D environment by utilizing the Kinematic Driver (KiD; Shipway & Hill, 2012). The key feature of KiD is that it prescribes a kinematic framework without the feedback from the microphysical processes (latent heat release, condensate loading, etc.). Despite being idealized, the benefit of this feature is that it simplifies the interpretation of the results so that any differences between model outputs from two different microphysics schemes must come directly from the schemes themselves rather than from complex feedbacks between microphysics, thermodynamics, and dynamics. This is therefore a natural continuation of the box model in the previous work while retaining a large degree of simplicity. As noted in the previous section, although AMP can be configured to conserve any combination of two or three moments, all simulations in this study resemble a typical 3-moment bulk scheme, i.e., predicting the conventional 3rd, 0th, 6th moments.

In this study, 1D (column) "full microphysics" simulations are designed to mimic shallow warm cumulus clouds. By "full microphysics" we mean that droplet activation, condensation, evaporation, sedimentation, and collision-coalescence are all active. In these full microphysics tests, the initial conditions are based on KiD test case #102 (see the KiD documentation) which specifies an oscillating vertical velocity field along with initial temperature and relative humidity. Figure 2 shows the prescribed vertical velocity and the initial relative humidity profile. Note that the wind field is only set to advect vapor and hydrometeors and the temperature field is held constant in time. To cover a wide range of aerosol and dynamic conditions, we run a suite of simulations with vertically constant aerosol concentration (N_a) that cover aerosol environments from maritime ($100/cc$) to continental ($1600/cc$) and dynamics from calm ($w_{max} = 1\ m/s$) to vigorous ($w_{max} = 16\ m/s$). As mentioned earlier, two pairs of microphysics schemes (AMP-SBM and bin-SBM, AMP-TAU and bin-TAU) are tested for each case to increase the robustness of the results.

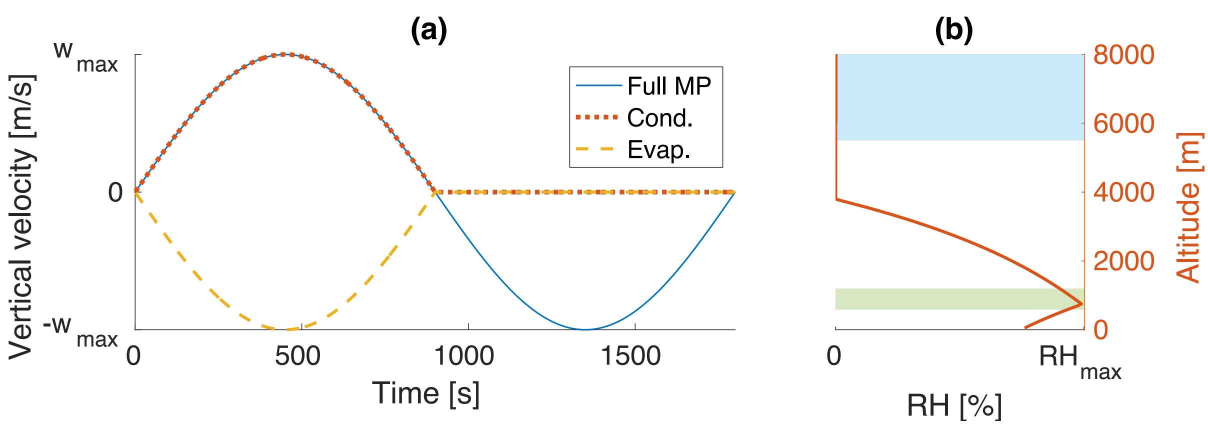

Figure 3.2. (a) Prescribed vertical velocity of the field for full microphysics, cases with condensation (updraft only), and cases with evaporation (downdraft only). (b) Initial relative humidity (RH) profile. The default $RH_{max} = 100\%$ unless otherwise specified in Figure 3.3. The light green band represents the height and thickness of the initial layer of water for collision-coalescence and evaporation cases, and the light blue one represents that for the sedimentation case.

We also run a systematic series of tests in which one or more microphysical processes is turned off in order to ascertain the contribution of individual processes to the total difference between the AMP and bin schemes. Figure 3.3 summarizes the simulations in this study: four sets of simulations with only a single process turned on, each with its respective initial condition suite (bottom row), along with three sets of simulations with combined processes and the same initial conditions as described above (left edge).

In all cases with condensation and droplet activation turned on (cases a, b, c, d), simulations are initialized with the same conditions as the full microphysics simulations. In cases b-d, evaporation is eliminated by holding the vertical wind speed at 0 m/s after the first half of the velocity oscillation (Figure 2a, orange dotted line).

In the cases without condensation or droplet activation (case e, f, g), we are required to initialize the simulation with existing condensed water. For the collision-coalescence case (e), water is initialized between 600 m and 1200 m with sizes in the cloud droplet category (initial mean mass diameter $\overline{D}_m = 15 - 27\ \mu m$) and with the shape parameter ranging from 1 to 9. No vertical wind is included and so these simulations are essentially the same as box model simulations.

For sedimentation (case f), we initialize with an existing rain water layer between 5500 m and 7000 m, similar to what was done in Milbrandt & Mctaggart-Cowan (2010), the only difference being that our initial rain water path increases linearly from 0 at the bottom to 0.5 g/kg at the top of the layer. The $\overline{D}_m$ in these cases are set to typical raindrop sizes ($200 - 600\ \mu m$). As with collision-coalescence, we vary the shape parameter ($\nu = 1 - 9$) to test how AMP responds to different initial distribution widths in these idealized cases and there is no vertical wind.

For evaporation (case g), the simulations are again initialized with a liquid water layer between 600 m and 1200 m with the same range of cloud droplet sizes as for collision-coalescence. We also vary the initial maximum relative humidity (RH_{max}) from 40% to 100% (Figure 2b). The vertical wind speed evolves according to the yellow dashed line in Figures 2a where $w_{max} = 2\ m/s$. Although there exist countless other combinations of microphysical processes and initial conditions, we find these seven cases to be the most useful for illustrating the structural differences between bulk and bin schemes.

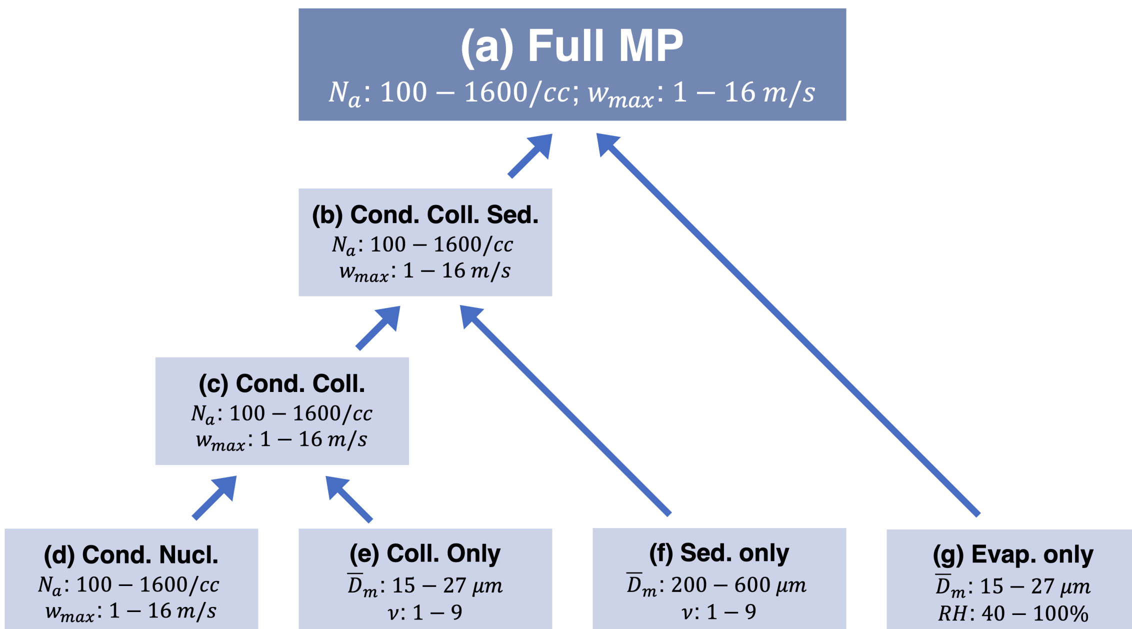

Figure 3.3. A selection of simulations tested in this study. Note that all cases with condensation turned on automatically include the nucleation process and it is found to lead to almost no difference between AMP and bin schemes.

3.4 Differences between AMP and bin simulations

As our main objective is to reveal the structural differences between bulk and bin schemes in general, the results shown in this section (percent differences, coefficients of determination R^2, etc.) compare AMP simulations with simulations using AMP's underlying bin scheme, as was done in I19 and I22. (We note that the bin scheme simulations should not be treated as benchmark or truth, and bin schemes are not inherently superior than bulk schemes in general as the difference between the two bin schemes tested can be significant.) In this study, we run AMP with two different underlying bin schemes (SBM and TAU) and we only draw conclusions if a qualitatively similar difference is present for both SBM and TAU.

Figure 3.4 (hereafter referred to as the pyramid figure) gives a high-level summary of AMP-bin mean differences in the test cases shown in Figure 3.3. The rest of this section will specifically discuss the full microphysics case regarding an overall AMP-bin difference, cases with individual processes turned on regarding the source of that difference, and the cases along the left edge regarding the interaction effect of microphysical processes on AMP-bin difference.

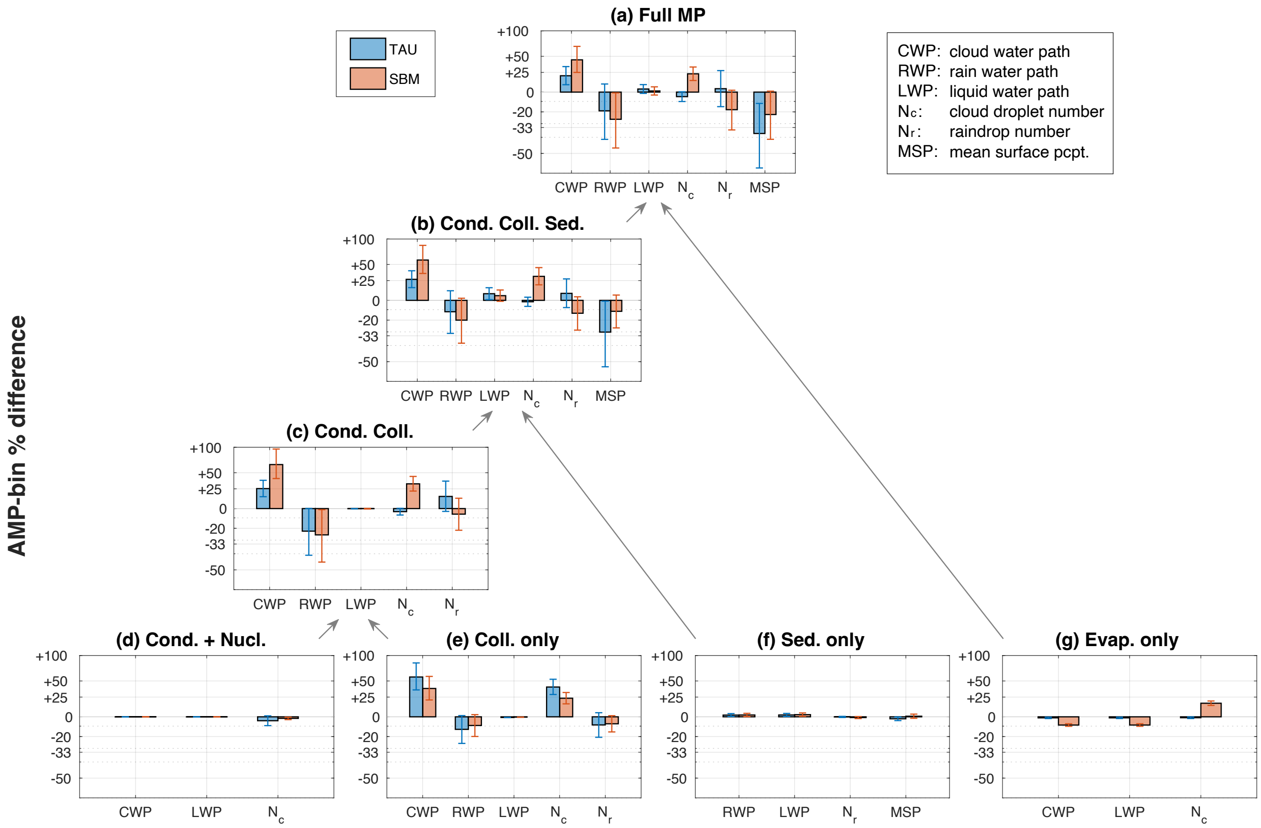

Figure 3.4. Summary of the effect of structural difference between AMP and bin. Each bar represents the mean percent difference between AMP and bin across the simulation suite shown in Figure 3.3. A selection of simulations tested in this study. Note that all cases with condensation turned on automatically include the nucleation process and it is found to lead to almost no difference between AMP and bin schemes., with the error bar showing the standard deviation of AMP-bin ratio across the initial condition space. The vertical axes are in log-scale for intuitive ratio comparison. Variable symbols are defined in the upper-left box.

3.4.1 Full microphysics

For the full microphysics simulations, we compared several cloud/precipitation properties between AMP and bin and here we show three: liquid water path (LWP), cloud water path (CWP), and surface precipitation rate (Figure 3.5). There are many ways to compare the output of AMP and bin; here we report the correlation of each property's timeseries in AMP with its timeseries in bin in terms of R^2 (text color) and the ratio of each property's temporal mean in AMP to that in bin (cell shading). Overall, we find similar LWP between AMP and bin but very different CWP and surface precipitation rate.

The cloud property that is most similar between AMP and bin is LWP. We find that the difference in LWP between bin and AMP is small across the simulation suite for both underlying bin schemes, with a mean ratio between 0.9 and 1.1 (or percent difference less than 10%) (Figure 3.4a and Figure 3.5a, b). This is expected because LWP is strongly controlled by condensation, which behaves similarly between the AMP and bin schemes (see Section 3.4.2.1), despite AMP having no knowledge about the explicit distribution from the previous time step.

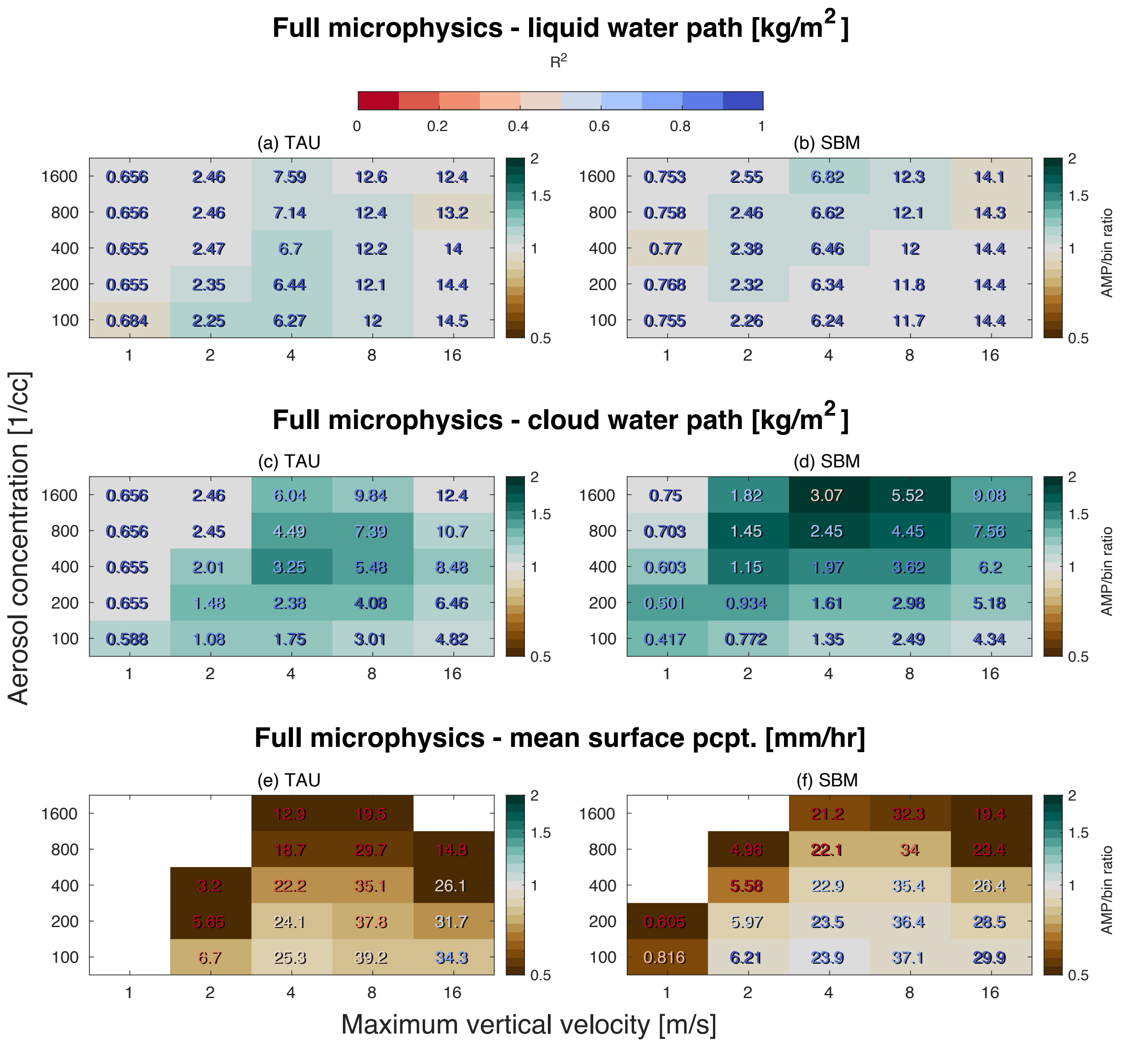

Figure 3.5. Summary of how mean (a, b) LWP, (c, d) CWP, and (e, f) mean surface precipitation are sensitive to aerosol concentration and maximum vertical velocity. **Bluer numbers and grayer grid cells mean more similarity between AMP and bin simulations.** Each grid cell represents a full simulation with a certain combination of aerosol concentration and vertical velocity. Number in the grid: the mean value of, for example, LWP across the entire bin simulation. Color of the number (red-blue): temporal correlation (R^2) between AMP and bin. Grid cell shading (brown-green): ratio of mean value of, for example, LWP (AMP/bin).

On the other hand, the two schemes start to diverge when it comes to the partitioning of liquid water content into cloud and rain water content. Across the entire simulation suite, AMP consistently underestimates the rain water content (Figure 3.4a) and overestimates cloud water (Figure 3.4a and Figure 3.5c, d), each by ~20% on average. As we will show, this discrepancy likely comes from the collision-coalescence process. As the derivative of cloud droplets, raindrops can be inherently harder to predict in AMP even with the same physical parameterization as the bin model. The biggest difference between AMP and bin lies in their mean surface precipitation rate, where AMP predicts consistently less rainfall than the bin counterpart by at least 10%, sometimes up to 50% (Figure 3.4a and Figure 3.5e, f). This is because surface precipitation is sensitive to not only the aforementioned rain production rate but also sedimentation rate, which is another process that leads to an even larger difference between the two schemes (see Section 3.4.2.3). Finally, differences in cloud droplet and raindrop number concentration are inconsistent in sign across the AMP-bin pairs, but usually 10% or less (Figure 3.4a).

Despite the noticeable difference between AMP and bin schemes, it is also worth noting that the magnitude of the AMP-bin difference is similar to that between the two bin schemes, TAU and SBM, as shown in a times series comparison of cloud water path and mean surface precipitation rate in Figure 3.6a-b for the case $N_a = 400/cc, w_{max} = 2\ m/s$. Figure 3.6c-d summarizes the full simulation suite similarly to Figure 3.5. The important implication from this significant TAU-SBM difference is that, when comparing cloud water path and mean surface precipitation, the parameterization differences (between TAU and SBM) are at least as important as the structural differences (between bin and bulk schemes), if not more important in the case of TAU. This suggests that it is difficult to draw any conclusions about the ways in which bin schemes are “better” than bulk schemes by simply comparing off-the-shelf bin and bulk schemes.

In summary, across the entire aerosol concentration ($100 - 1600/cc$) and maximum vertical velocity ($1 - 16\ m/s$) domain, we find that the overall AMP-bin difference is small and usually even less prominent than the difference between the two underlying bin schemes (SBM and TAU).

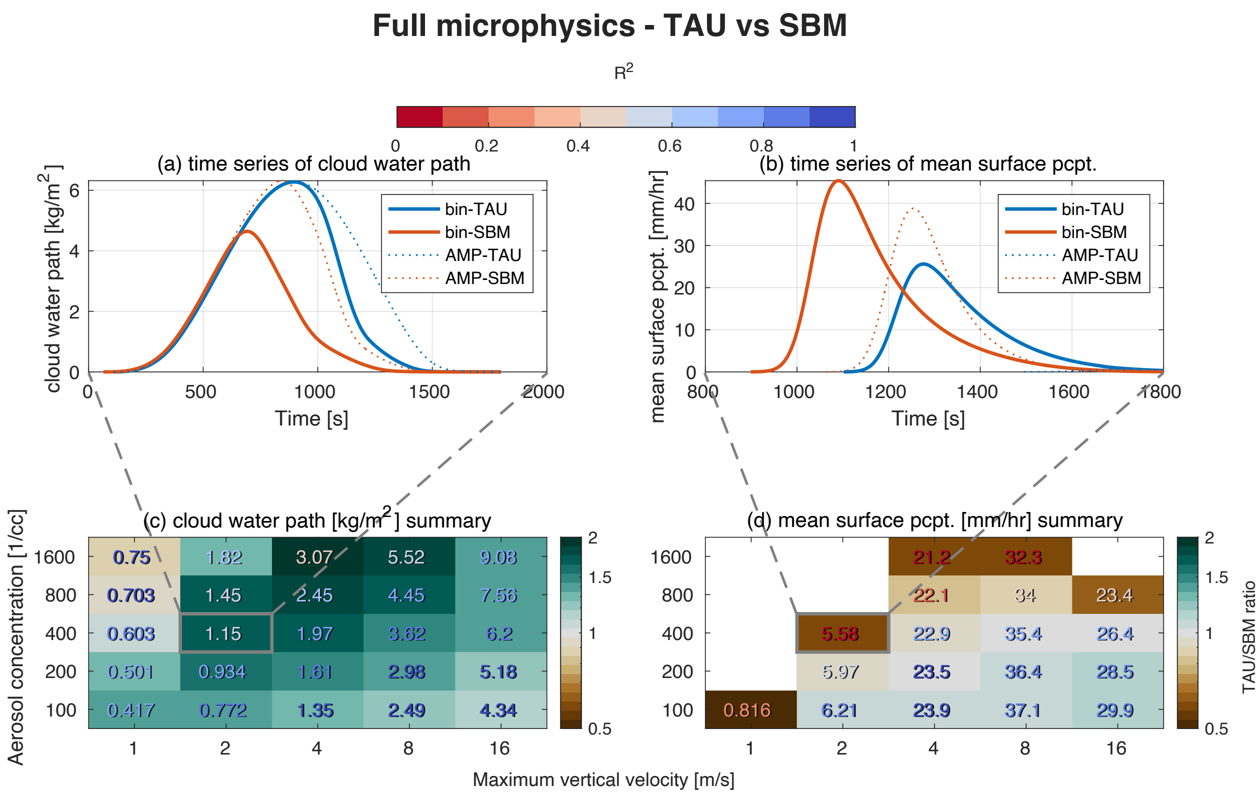

Figure 3.6. Time series of (a) cloud water path and (b) mean surface precipitation rate of the case $N_a = 400/cc$, $w_{max} = 2\ m/s$. A summary comparison between TAU and SBM are shown in (c) Cloud water path and (d) mean surface precipitation rate, which are similar to Figure 3.5c-f. The number in the grid is now the mean value of the corresponding variable in the entire SBM simulation. The grid cell shading represents the ratio of mean value between TAU and SBM.

3.4.2 Simple Microphysics

In order to understand which microphysical process(es) most contribute to the manifestation of structural differences between the scheme types, we next discuss the idealized simulations with only single microphysical processes (condensation and nucleation, evaporation, sedimentation, and collision-coalescence).

3.4.2.1 Condensation and nucleation

When only condensation and nucleation are turned on, our tests show that AMP can capture the evolution of cloud mass almost perfectly regardless of aerosol concentration or vertical velocity while it slightly underestimates number concentration compared to the bin schemes (Figure 3.7). Among the 25 test cases, only one case ($N_a = 400/cc$, $w_{max} = 4\ m/s$) will be shown in detail since all cases in the simulation suite are qualitatively similar and the magnitude of the difference is not a function of the initial conditions.

For cloud mass, the nearly perfect emulation of the bin scheme suggests that having the knowledge of the explicit PSD is not necessary for predicting the cloud water path when condensation is the dominating microphysical process in a cloud. This is perhaps not surprising since the amount of mass condensed is largely a product of the evolution of supersaturation, which is strongly controlled by the dynamics but only weakly affected by the microphysics routine of the simulation.

With regard to the number concentration, the AMP-bin difference is slightly larger (Figure 3.7a) but still largely insignificant compared to the differences from other microphysical processes (Figure 3.4d). This difference is not related to condensation but due to droplet activation and the constraint of an assumed gamma distribution. Bin schemes typically activate a certain number of droplets based on CCN concentration and supersaturation and then assign them with the smallest possible diameter. This results in a discrete distribution with all droplets in one size bin. According to Steps 1 and 2 of the AMP procedure (Figure 3.1), AMP has to fit a gamma distribution to that one-bin histogram and then discretize it while ensuring mass conservation before passing the discrete distribution into the bin microphysics routine. However, the Step 1 of the AMP procedure might fail when no combination of gamma parameters can be found to conserve all three moments (3^{rd}, 0^{th}, 6^{th}) in which case small differences are introduced for the 0^{th} and 6^{th} moments but not the 3^{rd} moment (by design). The time and altitude of such failure are shown in red in Figure 3.8b, and one such instance is zoomed in and shown in Figure 3.8a. As noted earlier, the bin scheme's (SBM) distribution has all mass in the smallest size bin, whereas AMP overflows a small portion to the larger size bins due to the constraint of a gamma distribution. Since mass is always conserved during Step 1 of the AMP procedure, this leads to an overestimation of mean droplet size and therefore an underestimation of number concentration. Although AMP can sometimes fail to represent the bin scheme during droplet activation, in reality, however, newly activated droplets do not all have the same size. Compared to bin schemes in which all newly activated droplets are of the same size, which results in a zero-width PSD, the bulk approach that uses a gamma distribution to describe the PSD of newly activated droplets is perhaps closer to reality.

I19 also found that AMP could nearly perfectly reproduce the bin results for condensation alone. However, in those tests, droplet nucleation was not included, and AMP and bin simulations always started with identical droplet size distributions. As such, the tests here provide a more rigorous test of AMP's ability to simulate the condensation rates by adding in the complexity of droplet nucleation.

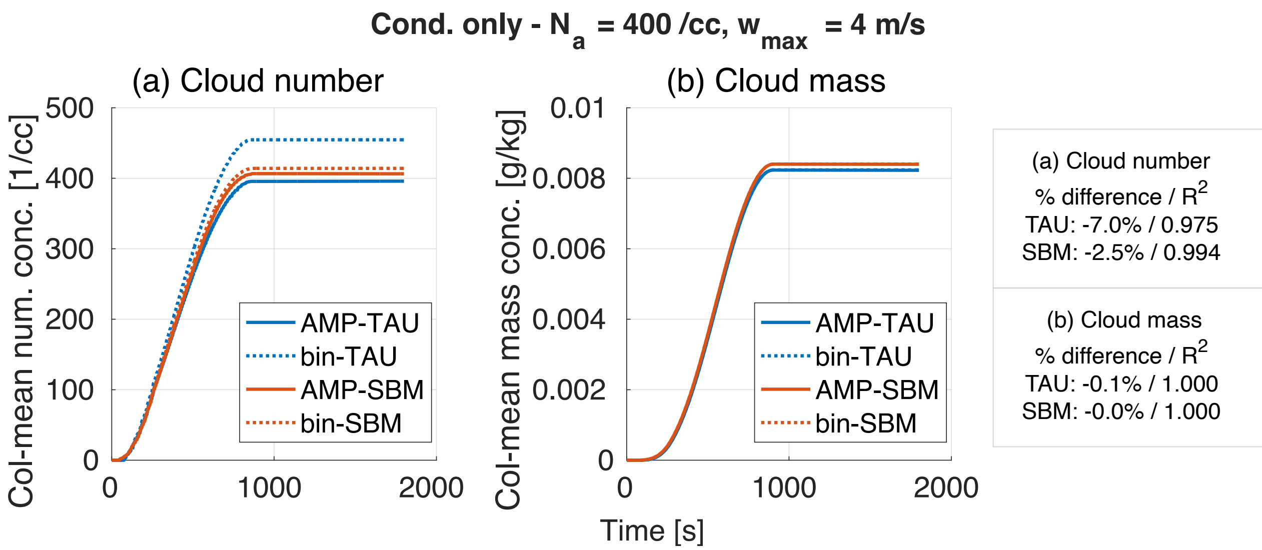

Figure 3.7. Evolution of column-mean cloud droplet (a) number and (b) mass concentration. The mean AMP-bin percent difference of all 25 tested cases and their R^2 are noted on the rightmost panel.

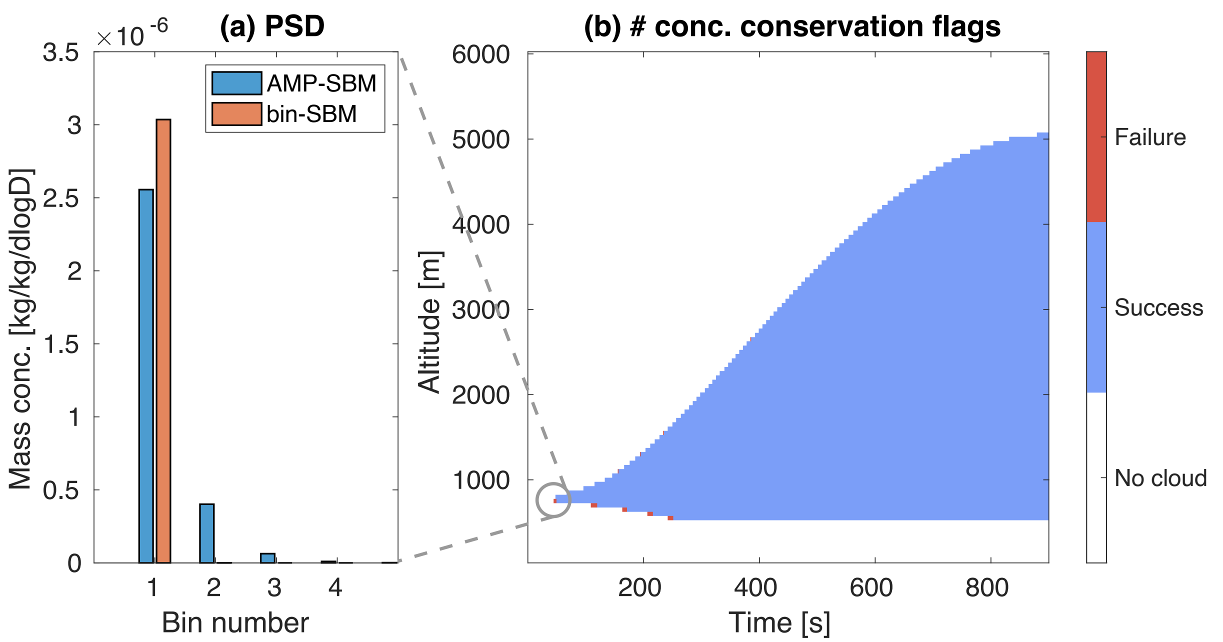

Figure 3.8. (a) a snapshot of PSD at t = 45 s, z = 750 m (circled in b). Only the first four bins are shown since the rest have no mass. (b) Profile of whether number concentration conservation is successfully conserved during Step 1 of AMP procedure. Only the first half (900 s) of the simulation is shown since no new droplets are activated in the second half. Note that mass again is always conserved.

3.4.2.2 Evaporation

We find negligible difference between AMP and bin schemes for the evaporation-only simulation suite with varying initial cloud droplet sizes and relative humidity (RH) environments. AMP-SBM tends to evaporate mass too quickly but reduce the number concentration too slowly compared to bin-SBM (Figure 3.4g). AMP-TAU and bin-TAU are nearly identical (Figure 3.4g). There was no strong dependence of the differences on the initial RH or initial mean droplet size. As with the condensation only case, only one simulation will be shown in detail due to the similarity between all test cases. Figure 3.9 shows the evolution of cloud number and mass for the case $RH = 99\%$, $\overline{D}_m = 25\ \mu m$. Although AMP and bin somewhat diverge when the fraction remaining is between 0.1 and 0.7, the overall difference between AMP and bin is small ($< 10\%$) and comparable to, if not smaller than, the difference between bin-SBM and bin-TAU.

The reason why AMP tends to evaporate number more slowly and evaporate mass faster than the bin schemes is likely because of the homogeneous mixing assumption in which all droplets are assumed to experience the same relative humidity. As shown in the snapshots of size distribution in Figure 3.10, as evaporation eliminates smaller droplets faster than larger droplets, the mean droplet size increases and the distribution shape changes for the bin scheme case. On the other hand, since AMP is forced to let the distribution shape conform to a gamma one, it redistributes mass within the PSD and inadvertently creates droplets even larger than before the evaporation, as shown in the shaded areas in Figure 3.10. This behavior is especially evident in AMP-SBM. These handful of extra-large droplets are what lead to the slower number evaporation and faster mass evaporation shown in Figure 3.9. Nevertheless, since this effect is not present in TAU, we can conclude that this problem is not universal to bulk schemes in general and can be largely mitigated with an appropriate parameterization for evaporation.

We tested evaporation of rain ($\overline{D}_m = 200 - 600\ \mu m$) in addition to cloud with the four schemes and found no difference between AMP and bin since the aforementioned effect becomes negligible when the mean size is significantly larger (not shown).

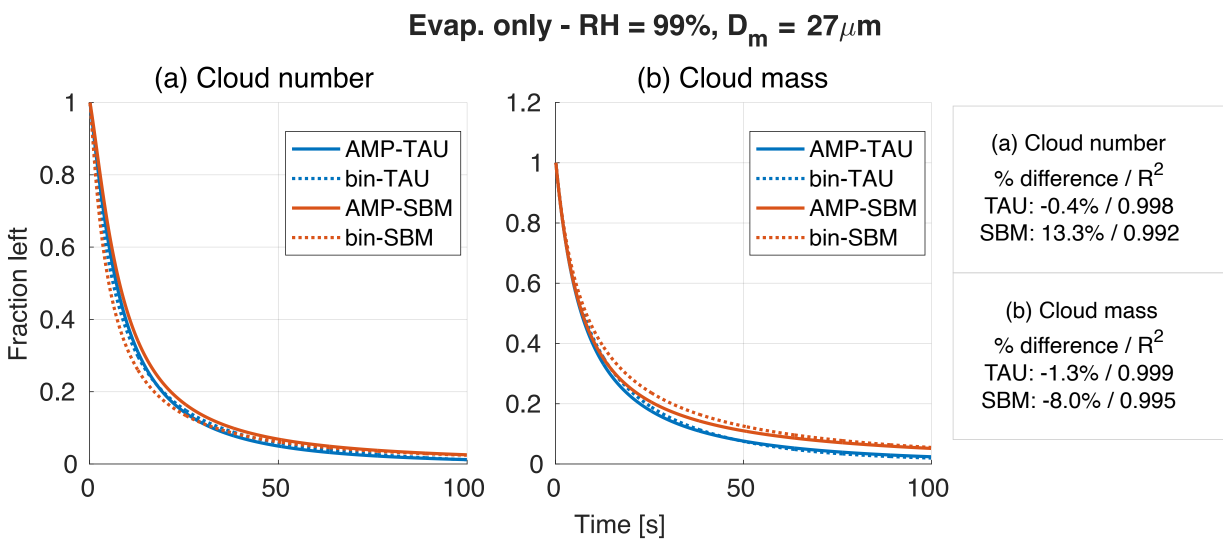

Figure 3.9. Fraction of (a) cloud number and (b) cloud mass evaporated over time with 99% initial maximum RH, 25 μm $\overline{D}_m$. The shape parameter is set to 4, and the mass mixing ratio is set to 1 g/kg. The mean AMP-bin percent difference of all 25 tested cases and their R^2 are noted on the rightmost panel.

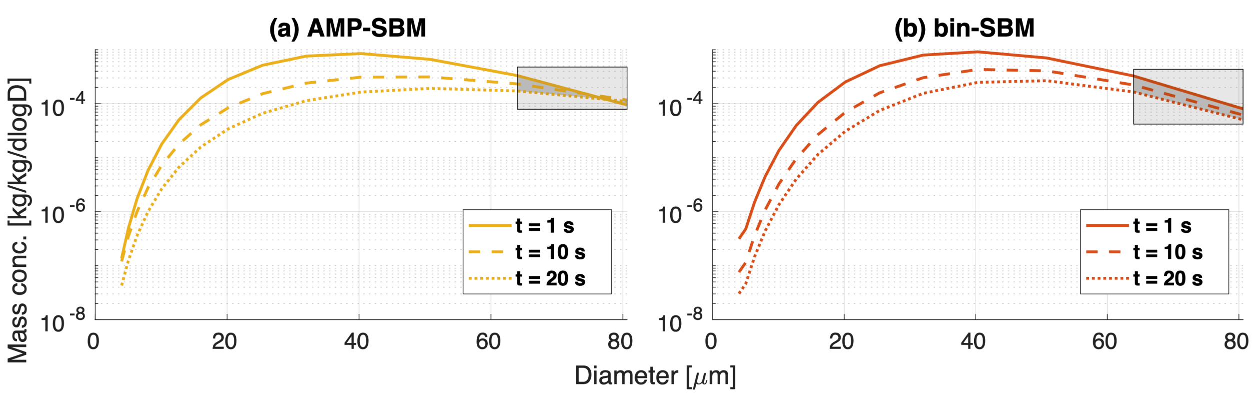

Figure 3.10. PSD of AMP-SBM vs bin-SBM in the same evaporation simulation as Figure 3.9 at 1 s, 10 s, and 20 s and z = 1200 m. The TAU cases are not shown as the difference between AMP and bin is negligible.

3.4.2.3 Sedimentation

The sedimentation-only simulation suite tests how raindrop PSDs with different mean sizes and distribution widths respond to sedimentation. AMP is found to have a slightly less size-sorting effect than the bin schemes. However, the mean AMP-bin difference is found to be small ($< 5\%$) for both rain mass and number concentration (Figure 3.4f and Figure 3.11). Like the previous two tests, one representative case ($\overline{D}_m = 600\ \mu m, \nu = 3$) will be shown in detail below since the results are similar across cases. As can be seen in Figure 3.12, the evolution of rain mass and number can be captured reasonably well by AMP, while it tends to overestimate the sedimentation rate of rain number and underestimate the sedimentation rate of rain mass compared to bin schemes. A detailed comparison between the PSDs of AMP and bin can be seen in Figure 3.13. This AMP-bin difference is likely again due to the constraint of an assumed distribution shape. Since the largest droplets preferentially fall from the layers above, the PSD of the layers below starts to become less gamma-like due to these additional largest droplets. Again, as AMP does not remember the explicit PSD between time steps, the mass of these largest droplets that fell to the layers below in the previous time step is redistributed towards droplets of smaller sizes. As terminal velocity is positively correlated with droplet size, the artificial loss of these largest droplets leads to a lower sedimentation rate, which manifests as a slightly weaker size sorting effect compared to the bin schemes, i.e., mass falls slower while number falls faster in AMP than the bin schemes. Our results are qualitatively in agreement with Milbrandt & Mctaggart-Cowan (2010) who performed similar tests.

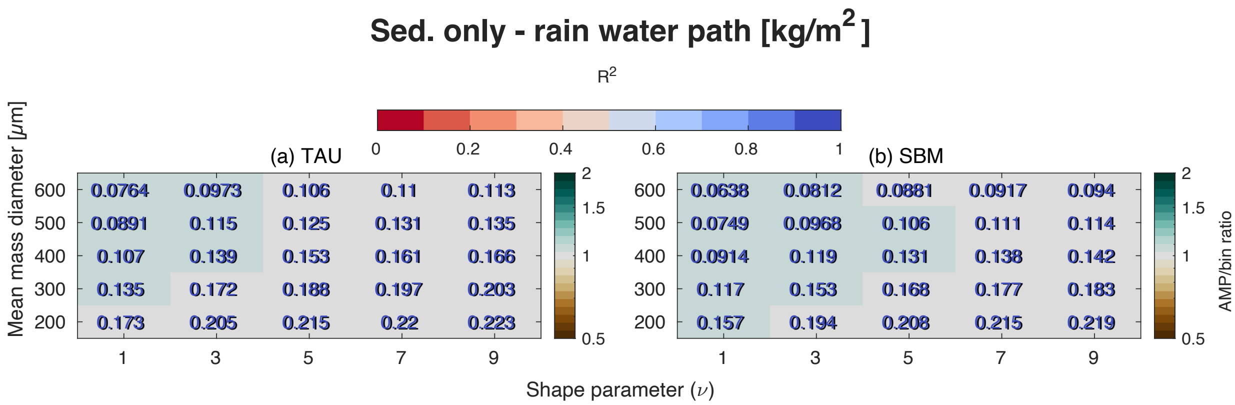

Figure 3.11. As in **Figure 3.5** but for rain water path in the sedimentation only case.

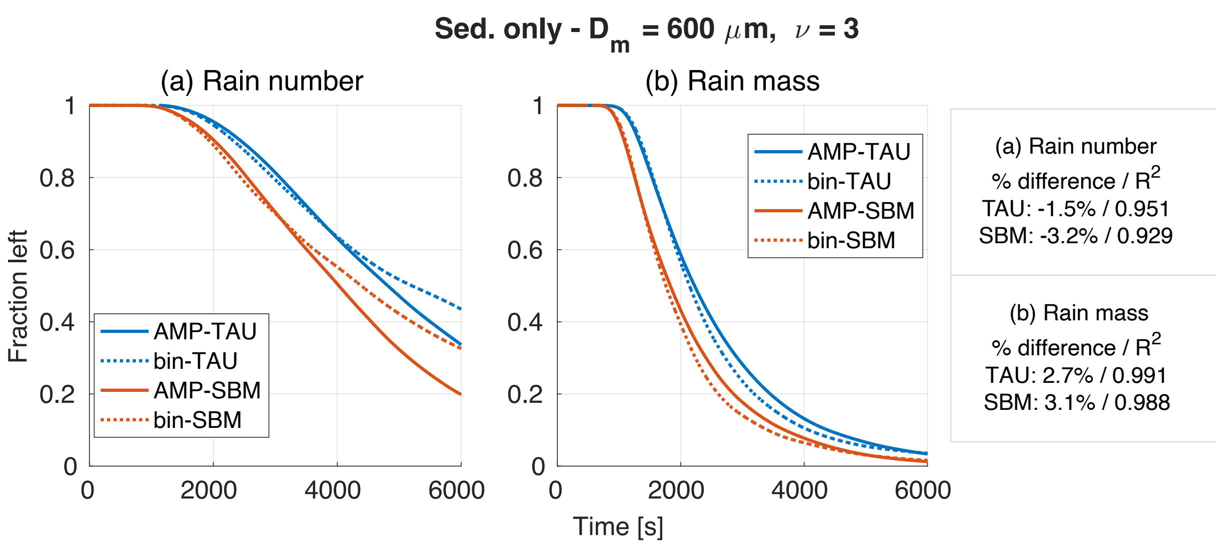

Figure 3.12. Fraction of (a) rain number and (b) rain mass that has yet to fall out of the system. The mean AMP-bin percent difference of all 25 tested cases and their R^2 are noted on the rightmost panel.

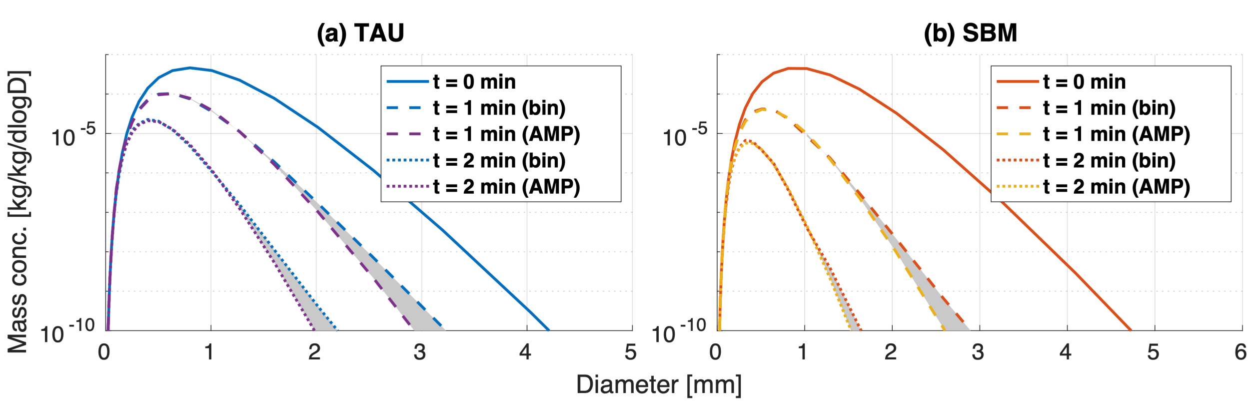

Figure 3.13. PSD of AMP vs bin in the same sedimentation simulation as Figure 3.12 at t = 0 min, 1 min, 2 min. The snapshot is taken at the second to top layer (z = 6933 m).

3.4.2.4 Collision-coalescence

Collision-coalescence in AMP produces rain much more slowly than in the bin schemes, which turns out to be the most difference-inducing microphysical process among all, as was also the case in I19. I22 took a more in-depth look at collision-coalescence in AMP vs. bin. The results here focus only on the traditional 3M AMP configuration and are in agreement with the discussion in I22.

A comparison of how long it takes for each scheme to convert half of initial cloud mass to rain mass (cloud half-life) through collision-coalescence is shown in Figure 3.14. AMP is found to be systematically slower than the bin schemes at growing cloud droplets into the rain category. A closer look at the comparison of the PSD evolution reveals that AMP, having two separate cloud and rain modes, often has trouble making "rain initiators," the handful of extra-large droplets that can serve as the seeds for collision-coalescence and the subsequent rain production. Specifically, in the bin schemes, the growth of cloud droplets happens disproportionally to the largest ones between $t = 1\ min$ and 6 min, as indicated by the shaded area in the lower panel of Figure 3.15 (c, d). Meanwhile, the change in the AMP PSD happens much more evenly across the spectrum, as shown in the upper panels of the same figure (a, b). This behavior of AMP is what delays the production of those rain initiators, and the problem is exacerbated when the condition is not in favor of collision-coalescence, i.e., small mean droplet size and large shape parameter, hence the larger discrepancy between AMP and bin towards the lower right corner of Figure 3.14.

The gamma distribution assumption and the intrinsic positive feedback nature of collision-coalescence (more large droplets lead to larger difference in terminal velocity, hence more collisional growth) are the two major factors slowing down the collisional rate in AMP.

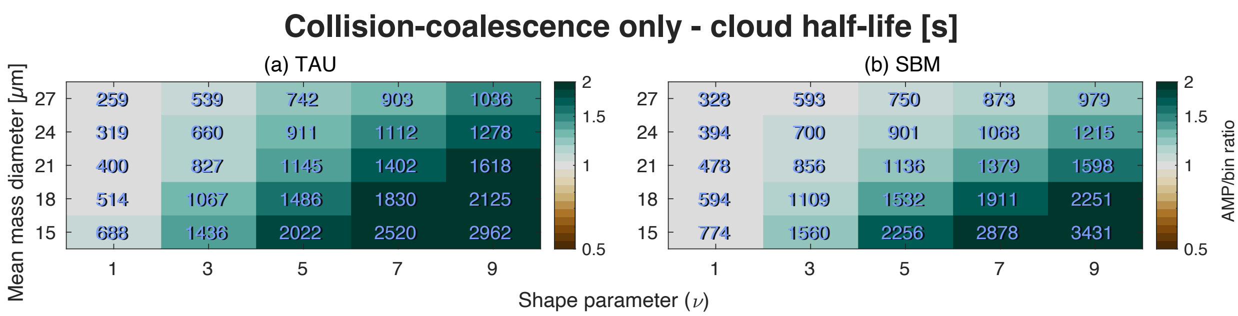

Figure 3.14. As in **Figure 3.5** but for cloud half-life in collision-coalescence only simulations.

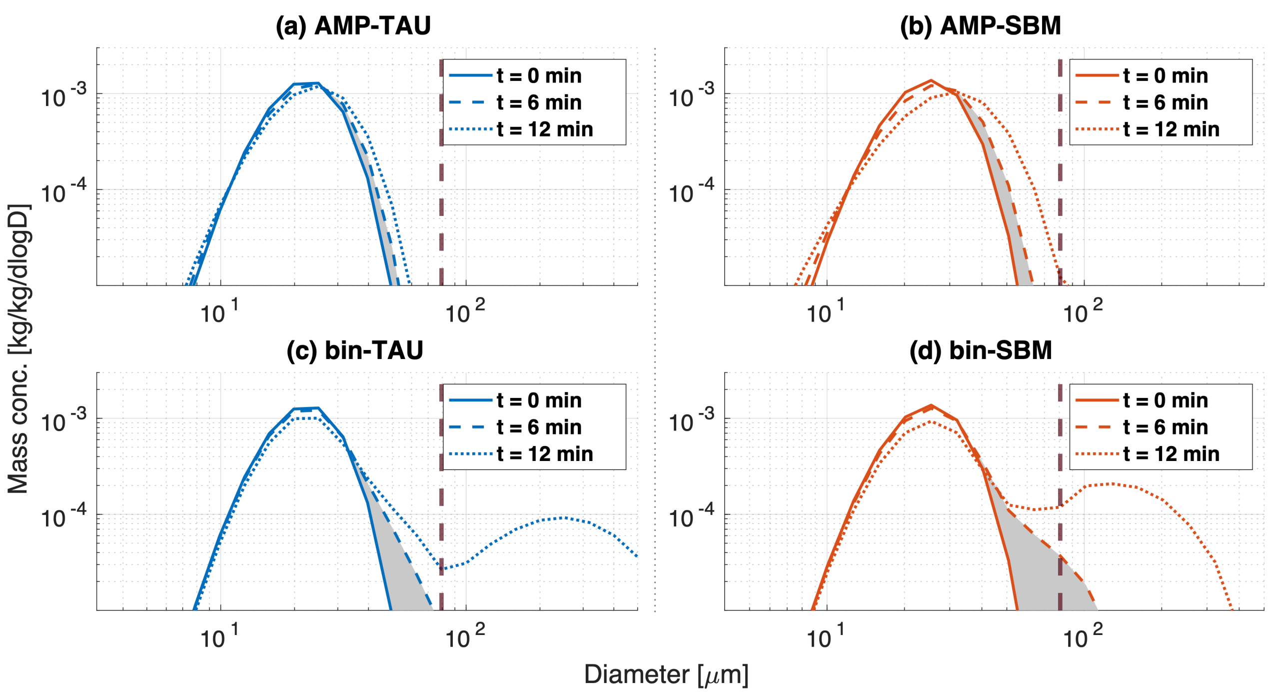

Figure 3.15. Snapshots of size distribution for AMP and bin schemes in the collision-only simulation ($\overline{\mathrm{D}}_{\mathrm{m}}$ = 21 μm, ν = 9, z = 1200 m). The shaded area represents the change in distribution between 1-min and 6-min mark. The dark red vertical dashed line marks the threshold size separating cloud and rain category in AMP.

Next, we shift our perspective to the differences between AMP and bin in simulating rain production, which is closely related to collision-coalescence. In traditional bulk schemes, warm phase collision-coalescence is artificially partitioned into three subprocesses: autoconversion (coalescence between cloud-sized droplets to form rain-sized drops), accretion (raindrops collecting cloud-sized droplets to form larger raindrops), and self-collection (of cloud or rain drops). Among them, autoconversion is particularly difficult to model and has posed major challenges to the development of bulk schemes ever since its inception despite the tremendous amount of effort in recent years even with machine learning techniques (Berry & Reinhardt, 1974; Chiu et al., 2021; Graham Feingold et al., 1998; Khairoutdinov & Kogan, 2000; Y. Kogan, 2013; Lee & Baik, 2017; Y. Liu & Daum, 2004; Seifert & Beheng, 2001; Seifert & Rasp, 2020). In AMP, although the microphysics routine itself is performed by the bin schemes and hence does not distinguish between these modes of collision-coalescence, we can still assess these processes using careful tests.

To see whether the challenge in representing autoconversion in bulk schemes is simply a result of its microphysical parameterizations or its bulk-like structure, we test how the AMP-bin difference is sensitive to the proportion of autoconversion in rain production by initiating a bimodal distribution (two gamma combined) with varying configurations of the two modes. Here, we denote these two modes as the $L1$ mode and the $L2$ mode ("L" for liquid water), where the mean size of $L1$ is smaller than $L2$. Note that the two modes do not imply their respective size being larger or smaller than the cloud-rain size threshold D_t. In the context of collision-coalescence, they can be pictured as the collected mode ($L1$) and the collector mode ($L2$). In all autoconversion sensitivity tests, we set a constant $\overline{D}_m = 15\ \mu m$ for the $L1$ mode, a constant total liquid water content at $q_l = 1\ g/kg$, same initial $\nu = 5$ for both $L1$ and $L2$ modes, but vary mass fraction of the collector $L2$ mode ($X_{L2} = \frac{L2\ mass}{L1\ mass + L2\ mass}$) from 10^{-5} (almost all $L1$) to 1 (all $L2$) and a varying initial mean mass diameter of the $L2$ mode ($\overline{D}_{L2m}$) from 30 μm to 100 μm. If AMP can perform autoconversion well, then perhaps autoconversion parameterizations in bulk schemes can be improved. If AMP *only* has trouble in the cases where autoconversion dominates the rain production (high X_{L2} and low $\overline{D}_{L2m}$) but not in others, then we can conclude that the autoconversion problems in bulk schemes are not a result of poor autoconversion parameterizations but rather the structure of AMP-like bulk schemes.

The upper panels of Figure 3.16 show how much AMP and bin diverge as a function of X_{L2} (with a constant $\overline{D}_{L2m} = 50\ \mu m$) and as a function of $\overline{D}_{L2m}$ (with a constant $X_{L2} = 10^{-3}$). Clearly, AMP-bin difference is the largest when autoconversion dominates rain production (low $L2$ mass fraction and small $L2$ mode $\overline{D}_m$). This result shows that AMP and bin perform very similarly for accretion, but differently for autoconversion, which suggests that the difficulty in representing autoconversion is likely due to the bulk-like structure rather than the parameterization.

Almost all existing bulk schemes, however, are not only moment-resolved and have a fixed distribution shape, they typically also feature an artificially separate liquid water category (cloud mode vs rain mode). To test whether the representation of autoconversion is susceptible to this common feature of bulk schemes, we then perform the same set of tests using a version of AMP with a unified liquid water category, in which AMP searches for two sets of gamma parameters at the same time to create a bimodal distribution that conserves the total liquid water content (Step 1 of Figure 3.1), instead of sequentially searching for the gamma parameters for each liquid water categories (details of its mechanics can be found in I22). The lower panels of Figure 3.16 show the advantage of this AMP configuration. With the exact same microphysics routines and underlying moment-resolved structure as the original AMP, the unified category AMP is much better at representing the underlying bin schemes in almost all test cases, especially for cases where the original AMP struggles the most (high X_{L1} and low $\overline{D}_{L2m}$).

These results suggest that the perennial challenges involving autoconversion in bulk schemes likely stem not from the moment-resolved structure of a bulk scheme, but the fact that liquid water is artificially separated into two categories. If future studies can verify this finding with more general and realistic initial model configurations, then a bulk scheme with a unified liquid water category can potentially be more realistic than a traditional bulk scheme. I22 also found that the predefined cloud-rain size boundary could also slow down the growth of cloud droplets into the rain category, and the difference can be greatly reduced when AMP is configured to have a unified bimodal liquid category. For detailed analysis of collision-coalescence, we refer the interested readers to I22.

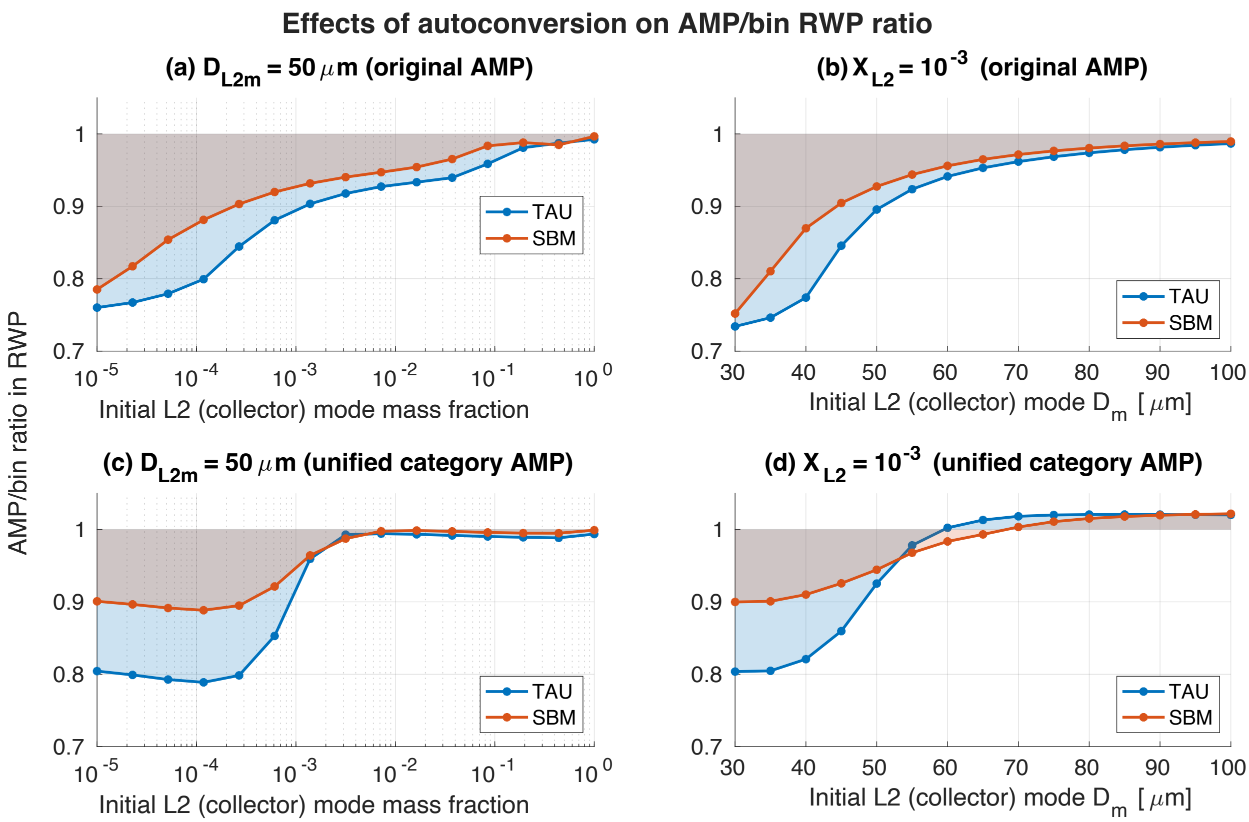

Figure 3.16. AMP/bin ratio in RWP as a function of initial L2 (collector) mode mass fraction and L2 mode $\overline{D}_m$. The upper panels are from the original AMP (with two liquid categories), and the lower panels are from the single category AMP (bimodal gamma). The shaded area shows the difference between AMP and its target (AMP/bin = 1).

3.4.3 Interaction effects between processes

The pyramid figure (Figure 3.4) summarizes how the structural difference between AMP and bin manifests as microphysical processes are progressively combined. Each bar represents the average percent difference between AMP and bin across a simulation suite designed for each process combination (shown in Figure 3.3).

An important suggestion from this pyramid figure is that the effect of structural differences in the full microphysics case (Figure 3.4a) can be traced down to the collision-coalescence (Figure 3.4e), suggesting that collision-coalescence is the major source of disagreement between AMP and its bin counterpart. Remarkably, the magnitude of the differences in the full microphysics simulations (Figure 3.4a) are nearly always of the same sign and of similar magnitude to those in the case of collision-coalescence only (Figure 3.4e).

It is most meaningful to trace the differences along the left edge (case d → c → b → a) since these simulation suites all use the same set of initial conditions. Figure 3.17 shows the change in AMP-bin percent difference by adding the process of sedimentation and evaporation to the simulation. The most noticeable change when sedimentation is added (case c to case b) is a slight increase in the LWP difference. This difference in LWP though is reduced in the full microphysics simulations (case a) when evaporation is added. In fact, for most quantities in Figure 19, the changes due to the addition of sedimentation are opposed by the addition of evaporation. These results suggest that the interaction of microphysical processes does not serve to amplify differences between AMP and bin, but rather that the interaction of processes, at least in this idealized scenario, has a small or insignificant impact on the total differences for most cloud and rain properties in AMP.

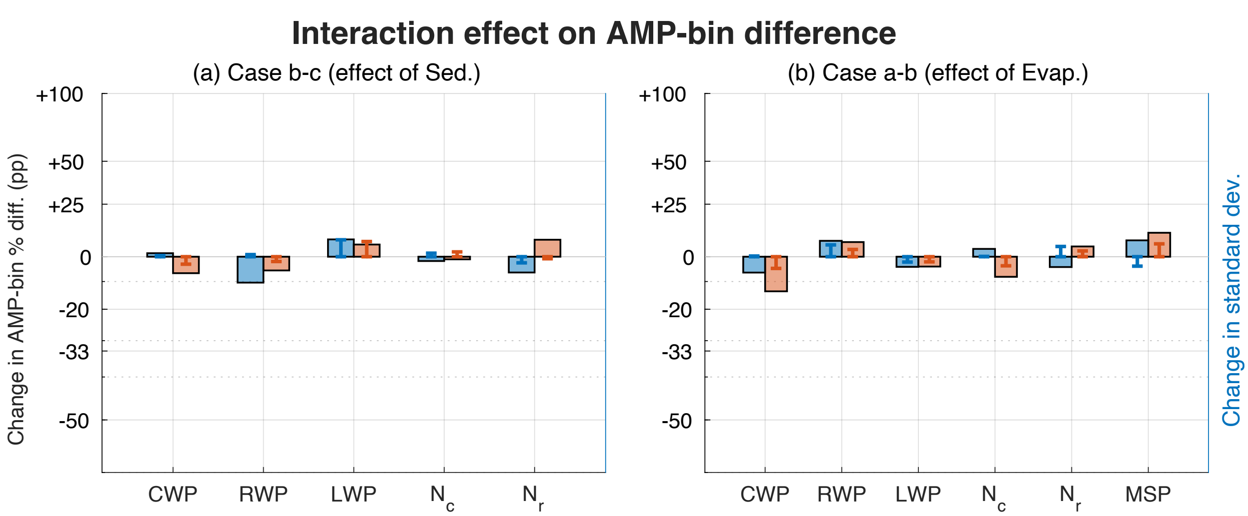

Figure 3.17. Effect of adding a microphysical process on AMP-bin difference. Bar heights represent the change in AMP-bin difference in percentage points (pp). Error bars represent the change in standard deviation by adding the process. The vertical axis range is kept the same as **Figure 3.4** for intuitive comparison.

3.4.4 Alternative size threshold separating cloud droplets and raindrop

Since AMP has cloud and rain as separate liquid water categories, one parameter that could affect the autoconversion rate in AMP is the size threshold separating the two categories. A lower size threshold could lead to faster autoconversion due to an earlier emergence of the rain mode, which can help mitigate the slow rain production problem associated with collision-coalescence discussed in Section 3.4.2.4. A smaller size threshold was tested in I22, and it was shown that, for the collision-coalescence process alone, a diameter threshold of $D_t = 50\ \mu m$ can greatly improve AMP's representation of SBM in a box model.

Here we rerun the entire simulation suite (Figure 3.3) to test the generality of this result by extending the simulation to one-dimensional model (KiD) and two types of bin schemes (TAU and SBM). In agreement with I22, we also find that AMP is much better at reproducing the bin results with this lower size threshold. Figure 3.18 shows that almost all the cases with $D_t = 50\ \mu m$ (bars with solid borders) have a smaller AMP-bin difference than its $D_t = 80\ \mu m$ (dotted borders) counterpart, especially for cloud water path and mean surface precipitation. Quite remarkably, the lower threshold results in nearly perfect partitioning of the LWP in AMP-TAU (Figure 17a).

The lower size threshold does occasionally result in larger differences than previously. Most notably, AMP with the lower threshold in case (d), where only condensation and nucleation are turned on, predicts a slightly lower cloud water path in AMP-TAU compared to bin-TAU. A closer look into the individual simulation (Figure 3.19) reveals that the apparent deficit in cloud water path comes from the early emergence of the rain mode due to the lower D_t, which results in a premature rain production via condensation. Note that the total liquid water condensed is still the same between AMP and bin, as shown in Figure 3.18d (LWP).

Nonetheless, the overall effect of this lower $D_t = 50\ \mu m$ is clearly a net positive over the original $D_t = 80\ \mu m$ when full microphysics is turned on. This change puts the AMP-bin difference even lower, often substantially lower, than the TAU-SBM difference (yellow bars in Figure 3.18), making the effect of structural differences between AMP and bin even smaller than the parameterization differences between the two bin schemes.

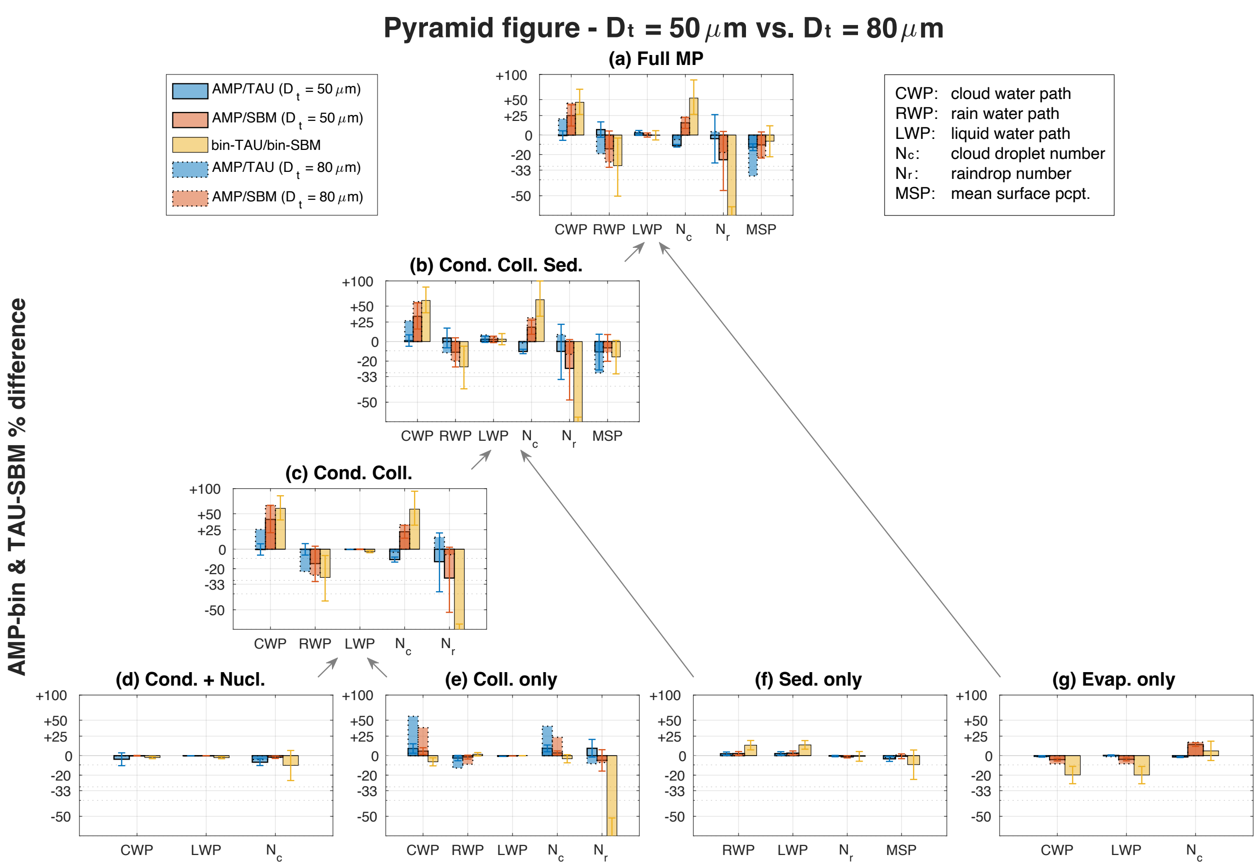

Figure 3.18. A pyramid figure comparing the AMP-bin difference between $D_t = 50$ μm (solid border) and $D_t = 80$ μm (dotted border, same as Figure 3.4) as well as the TAU-SBM difference. The error bars represent the standard deviation of AMP-bin or TAU/SBM ratio across the initial condition space.

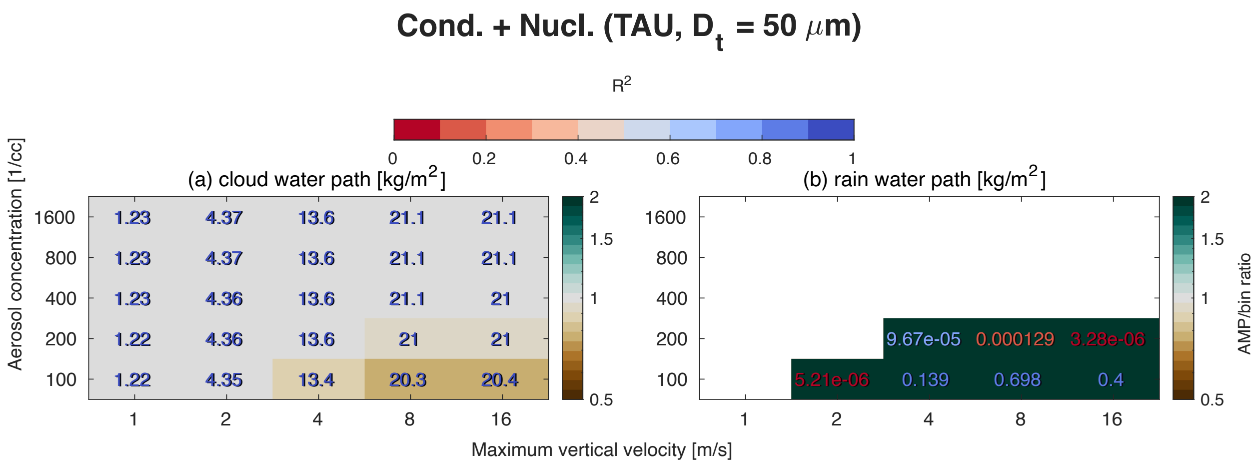

Figure 3.19. Summary of how (a) cloud and (b) rain water path is sensitive to aerosol concentration and maximum vertical velocity when only nucleation and condensation is turned on. Only TAU is shown in the figure as the AMP-bin difference found in SBM is negligible.

3.5 Summary

This study investigates how the structural differences between bin and bulk schemes (size-resolved vs. moment-resolved) manifest in their simulation results and how that knowledge can help shape the future of bulk scheme development. To do this, we must ensure that the bin and bulk schemes used in this study have identical microphysical parameterization routines, which can be a confounding variable, which is something that previous studies on this topic could not do since existing bin and bulk schemes are also different in their parameterizations. For this study, we use two existing bin schemes (SBM and TAU; Feingold et al., 1988; A. Khain et al., 2004; Tzivion et al., 1987, 1999) as the "benchmarks" and a custom-made bulk scheme (AMP; Igel, 2019), which is a wrapper function for an existing bin scheme. Because AMP uses the parameterization of the underlying bin scheme while only remembering the moment values between time steps (rather than the explicit PSD), it is technically a bulk scheme, and we can compare it against its underlying bin scheme to study the effect of their structural differences.

To build on what was done in Igel (2019), we adapted the 3M AMP into a one-dimensional kinematic driver (KiD) model and designed a suite of simulations with different model complexity. We first run tests with full microphysics turned on (condensation and nucleation, evaporation, sedimentation, and collision-coalescence), and then decompose them into individual and key combinations of processes in order to understand why bin and bulk schemes diverge and to study the interaction effects of microphysical processes on the AMP-bin difference. To make sure that the conclusions apply to a wide range of environmental and dynamics characteristics, we give each case a set of possible initial conditions (see Figure 3.3). We have the following conclusions based on these simulations:

1. Condensation alone can be represented almost perfectly by AMP compared to its underlying bin scheme, while droplet nucleation may cause AMP to underestimate slightly the number concentration due to the gamma distribution assumption. However, AMP's (or bulk schemes in general) approach could be desirable given that newly-activated droplets do not all fall into one size bin in reality.
2. Evaporation and sedimentation can be well represented by AMP. Small differences ($<$ 10%) may be noticeable due to the structural differences, but the AMP-bin difference caused by these processes are mostly negligible.
3. Collision-coalescence is the single largest source of discrepancy when AMP tries to emulate its bin counterpart. More specifically, AMP and bin struggle to agree on the

rate of autoconversion but appear to agree well if accretion is the dominant mode of rain production. Rain production in AMP can be significantly slower than the bin scheme when the cloud-rain threshold diameter is 80 μm. However, substantial improvement is gained when the threshold diameter is moved to 50 μm or if a unified liquid category is used (see also I22).

4. When full microphysics is turned on:
    a. Total liquid water content are represented well in AMP, with a mean AMP-bin difference of less than 5% for both quantities, regardless of the initial condition. This is because both quantities are largely controlled by condensation, which AMP can successfully represent as mentioned above.
    b. The quantity that shows the largest AMP-bin difference is the mean surface precipitation. The onset of precipitation predicted by AMP lags behind its underlying bin scheme since it is a product of sedimentation and collision-coalescence, both of which suffer, to a different degree, from the gamma distribution assumption. Again, a lower size threshold improves AMP's performance.
5. The interaction of microphysical processes does not serve to amplify the differences between AMP and bin, but rather has a small or insignificant impact on the total differences for most cloud and rain properties in AMP.

A surprising finding that is worth special recognition is that, in the full microphysics case, the mean AMP-bin difference is at least of the same magnitude of (when $D_t = 80\ \mu m$), and can be substantially smaller than (when $D_t = 50\ \mu m$), the mean TAU-SBM difference regarding cloud water path and surface precipitation rate (Figure 3.18). This shows that the choice of parameterization (SBM or TAU) can have an impact on the simulation results that is larger than the impact of model structure (bin or bulk). The results overall suggest that bulk schemes, *in principle*, are not as inherently limited in their ability to simulate microphysical processes as has been previously suggested (e.g., Fan et al. 2016). Rather, here we have shown that bin (size-resolved) and bulk (moment-resolved) schemes are more similar than they are dissimilar. In addition, if we look at these results from the opposite angle, the large differences between bin-SBM and bin-TAU show that the inherent uncertainties within the bin schemes can be much more significant than the structural differences between AMP and bin. This stresses that the results from bin scheme simulations should not be interpreted as ground truth by default but rather only a reference.

In summary, the work here is encouraging as it shows that AMP can emulate its underlying bin scheme under a wide range of circumstances, which is promising for future research involving bulk schemes. We have shown that virtually all AMP-bin differences (which again, for most processes are small) arise from assumptions regarding the underlying assumed PDF. Since the assumption of a fixed functional form is not a required feature for bulk schemes, the structural differences between bulk and bin schemes mentioned in this study can potentially be further minimized with smart implementation of schemes that do not rely on pre-defined functional forms for the PSD in the future (Chiu et al., 2021; van Lier-Walqui et al., 2020; Morrison, van Lier-Walqui, Kumjian, et al., 2020; Seifert & Rasp, 2020). Alternatively, as suggested in I22, the use of a unified liquid category could also bring the two scheme types closer together. Work is ongoing to further develop and test the unified category AMP in kinematic and dynamic simulations of clouds.

4 Unified Liquid Water Category Bulk Scheme

4.1 Background

Condensation, evaporation, collision-coalescence, and sedimentation are the four major microphysical processes that dominate how a liquid water droplet interacts with its environment. However, since there are typically $\sim 10^8$ droplets in every cubic meter of cloud and a cloud can easily reach $10^7 - 10^{10}\ m^3$ in size, it is usually infeasible to model these processes for individual droplets at a scale larger than a few cubic meters (e.g., Abma et al., 2013; Kumar et al., 2017; Perrin & Jonker, 2015). Statistical methods were therefore developed to model the microphysical evolution of a collection of droplets, instead of individual ones. Three major methods exist today, namely, bin schemes, bulk schemes, and Lagrangian particle schemes. As summarized in great detail in A. P. Khain et al. (2015), bin schemes resolve how droplets of different sizes (masses) interact with the environment and with each other. Bulk schemes only resolve the integrated moments of droplet distribution, typically the 3rd moment (mass) and the 0th moment (number), in each grid box. On the other hand, Lagrangian particle schemes track the properties and location of "superdroplets", each of which represents a large number of real droplets. Of the three, bulk schemes are the most computationally efficient and therefore the only type of scheme used operationally for weather forecast and climate prediction purposes.

At the expense of its computational efficiency, bulk schemes are known to face a number of unique challenges, for example in collision-coalescence and sedimentation (e.g., Igel et al., 2022; Milbrandt & McTaggart-Cowan, 2010), which could be associated with its fundamental design. In addition to using a predefined (often gamma) distribution to describe the particle size distribution (PSD), bulk schemes have typically also assumed two subcategories of liquid water (cloud and rain) ever since the first bulk scheme was proposed by Kessler in 1969. This is because liquid water PSDs in nature are observed to be bimodal, and they emerge by different microphysical processes – the cloud mode by condensation and the rain mode by collision-coalescence, respectively. Nearly all bulk schemes in the past have adopted this methodology (Table 2 in A. P. Khain et al., 2015), with the only exception to our knowledge being Kogan & Belochitski (2012).

An inevitable consequence of prescribing two categories of liquid water is that it necessitates a transfer of mass from one category to another. In a typical bulk scheme, this transfer of mass happens during collision-coalescence: "autoconversion" when cloud droplets collide to form raindrops and "accretion" when cloud droplets collide with raindrops to form larger raindrops. To parameterize these two processes, a size boundary between the two categories needs to be defined. Past studies have adopted a range of size boundaries anywhere between 50 μm and 80 μm (Berry & Reinhardt, 1974; Khairoutdinov & Kogan, 2000; Lee & Baik, 2017; Seifert & Beheng, 2001) in diameter, with some observation studies reach as low as 40 μm (Austin et al., 1995; Wood, 2005).

This disagreement has led to a few studies on the feasibility of a bulk scheme with atypical liquid water treatment (Y. L. Kogan & Belochitski, 2012; van Lier-Walqui et al., 2020; Szyrmer et al., 2005). More recently, the idea of a unified liquid water category bulk scheme has been revisited in Igel et al. (2022; hereafter I22) and Hu & Igel (2023; hereafter HI23). I22 found that a unified category (1-category, 4-moment) bulk scheme was noticeably superior compared to a separate category (2-category, 2-moment) bulk scheme when representing collision-coalescence, even though the number of total predicted moments and assumed gamma distributions are the same. Of all microphysical processes, autoconversion, which is the self-collection of cloud droplets to make raindrops, was found to benefit the most from the unified category (HI23). The reason for such improvement was attributed mostly to the lack of a predefined size boundary between cloud and rain category since there does not exist a single size boundary suitable for all circumstances (I22, HI23). However, these two studies only examined on the performance of unified liquid category in idealized models (box model in I22 and 1-D column model in HI23). I22 only examined collision-coalescence, and while HI23 examined all liquid microphysical processes, they only did so with a 6-moment bulk scheme (2-category, 3-moment). In this study, the 4-moment bulk schemes will be tested extensively as they are more common in operational models. Moreover, the exact configurations (predicted moments, assumed shape parameter, etc.) used for tests were chosen ad hoc and not examined systematically. This prompts a few questions:

Q1. What would be the best configuration for a 4-moment unified category bulk scheme regarding the combination of predicted moments and assumed shape parameter?

Q2. With this configuration, is a unified category bulk scheme demonstrably "better" than one with separate categories?

To address these questions, we examine whether this unified category bulk scheme makes systematically better predictions regarding cloud water path (CWP), rain water path (RWP), liquid water path (LWP), surface precipitation rate (SPR), and mass mean raindrop size ($D_{m,r}$) compared to a traditional two-category bulk scheme. A custom bulk scheme, AMP, is used to assess the performance of the unified category bulk scheme in a fair manner (Igel, 2019; hereafter I19). AMP was designed to be a bulk scheme in its essence, meaning that only moments like mass and number are carried to the next time step, but makes use of bin scheme microphysics routines. The advantage of using AMP is that it can be easily configured to predict different moments, assume different shape parameters, or switch between unified (U-AMP) or separate liquid category settings (S-AMP). In this study, S-AMP serves as a proxy for traditional separate category bulk schemes, and U-AMP as a novel unified category bulk scheme. AMP thus allows for an easy comparison among different configurations of U-AMP as well as assessing its advantages and disadvantages by comparing against the more traditional S-AMP. A detailed description of its design can be found in Section 2.

This paper is organized as follows. Section 2 explains the mechanism of AMP with unified liquid water category. Section 3 describes the model setup for the 1D simulations. Section 4 discusses the results from the simulation. Section 5 gives the concluding remarks of the findings.

4.2 Mechanics of AMP: bin physics put into a bulk scheme

As explained in more detail in I19 and Section 3.2 of this dissertation, AMP was initially designed specifically to study the characteristics of a moment resolved scheme (i.e. a bulk scheme) compared to a size resolved scheme (i.e. a bin scheme). In its initial design, AMP, like most existing bulk schemes, separated the liquid water category into cloud and rain modes, each of which conforms to a gamma distribution $N(D)$:

$$N(D) = N_0 D^{\nu-1} e^{-\lambda D}, \tag{4.1}$$

where N_0, ν and λ are the intercept, shape, and slope parameters. Starting from I22, a new version of AMP was developed that unified the liquid water category, which describes the entire liquid PSD spectrum with a linear combination of two gamma distributions:

$$N(D) = N_1 D^{\nu_1-1} e^{-\lambda_1 D} + N_2 D^{\nu_2-1} e^{-\lambda_2 D}, \tag{4.2}$$

where the subscript 1 and 2 represents the two modes, which will be referred to as L1 and L2 hereafter ("L" for "liquid"), where the mean size of L1 is smaller than that of L2. The terms "cloud" and "rain" are avoided since in principle it would be possible for both modes to have mean sizes that could be considered “cloud” or “rain”.

Figure 4.1 shows how AMP works and its different treatments of the liquid water category by the 4-moment unified category (U-AMP) and the 2-moment separate category (S-AMP). Note that both configurations predict four total moments. In both configurations, the shape parameters (ν’s) are both constants. Like a bulk scheme, AMP operates by calculating moments of the size distributions, where the kth moment of a distribution is given by the equation in the center of Figure 4.1.

1. At the beginning of each time step, the gamma distribution parameters are diagnosed from the four moment values from the last time step.
    a. S-AMP uses two moments (M_3', M_0') to diagnose the other two gamma parameters (N_0, λ) for each category sequentially. The gamma distribution of

the two categories are then concatenated together to obtain the full distribution.

b. U-AMP uses four moments (M_3', M_0', M_x', M_y') to diagnose all four parameters at the same time ($N_1, N_2, \lambda_1, \lambda_2$).

2. The PSD (which may or may not be bimodal) gets discretized to match the bin structure of the underlying bin scheme.
3. The discretized PSD gets passed into the bin microphysics routines.
4. Moment values are diagnosed after the microphysics routines complete. CWP and RWP in U-AMP are diagnosed in U-AMP during this step with an assumed size boundary of 80 μm in diameter.
5. These moment values (M_k) get passed into the dynamics routines (advection, turbulence, divergence, etc.), which are performed by the dynamical core which is not part of AMP. The products are the predicted moment values (M_k') for the next time step.

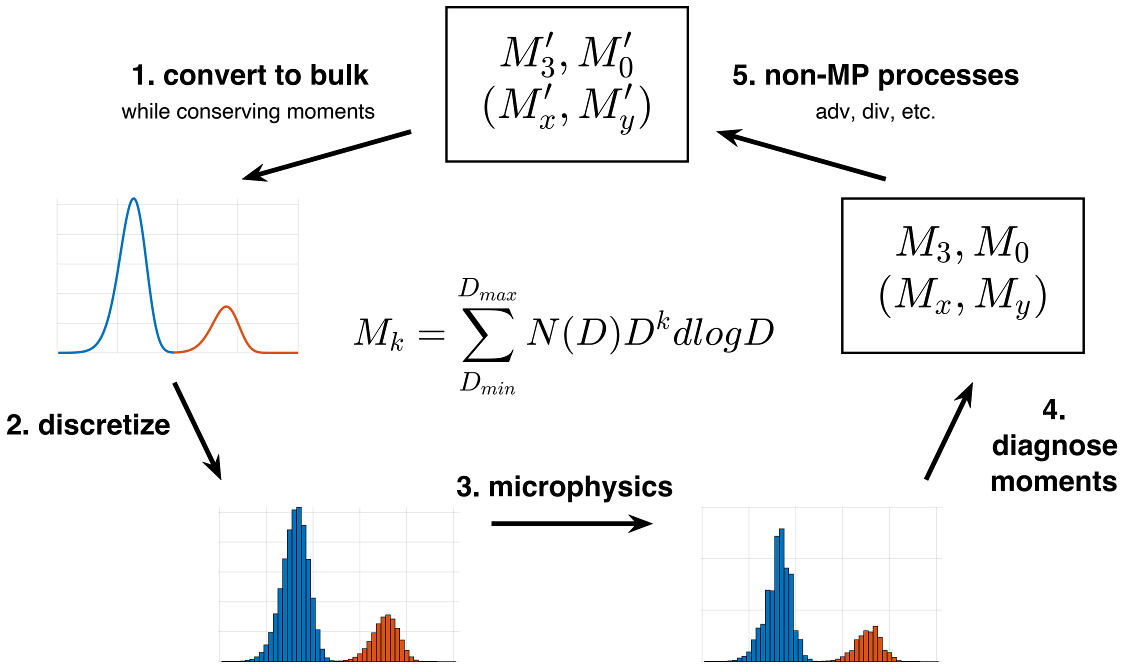

Figure 4.1. AMP's mechanics. The equation at the center is the calculation of the k^{th} moment of a discrete droplet size distribution N(D). D_{min} and D_{max} mark the size boundaries for each category in the case of S-AMP and for the entire liquid spectrum in the case of U-AMP. The blue and red parts of the distribution denote the two categories (S-AMP) or modes (U-AMP). Note that Step 5 is performed by the dynamical core and is not part of AMP.

We have chosen to study the configuration of U-AMP with four predicted moments because nearly all operational bulk schemes only have at most four moments to predict in the liquid category (2 moments for each category). The results from this comparison are therefore the most helpful in guiding future development of bulk schemes. Note however that U-AMP can be configured to predict six moments (as was done in HI23) and likewise S-AMP can be configured to predict three moments for each category (as done in I19, I22, and HI23).

Finally, we use two different underlying bin schemes, namely, the SBM (Hebrew University spectral bin microphysics; A. Khain et al., 2004) and TAU (Tel Aviv University bin scheme; Feingold et al., 1988; Tzivion et al., 1987, 1999) as the reference bin schemes, similar to what was done in I19, I22 (only SBM), and HI23. These schemes can also be run directly as the microphysics parameterization without AMP. These two schemes will be referred to generically as BIN.

4.3 Model Setup and Error Evaluation

The Kinematic Driver (KiD; Shipway & Hill, 2012) is used in this study to investigate U-AMP's feasibility in 1D column model. Similar to HI23 and many other studies (e.g., Hill et al., 2023), KiD is a favorable choice for theoretical studies such as this one as it is an idealized model without the feedback between microphysical processes and dynamics and thus eliminates most confounding variables.

Similar to HI23, every simulation case is performed using both the AMP and BIN schemes, We denote the simulations run by different microphysics schemes as AMP-SBM, bin-SBM, AMP-TAU, and bin-TAU and use the prefix "U-" or "S-" to distinguish between unified or separate category AMP. However, as was noted in HI23, the bin schemes should not be treated as "truth" since the difference between TAU and SBM can often be larger than bin-bulk difference. In this study, we still use the bin scheme results as reference for evaluating AMP's performance because (a) all AMP-bin differences in simulation results can be traced to their structural difference because AMP uses the same underlying physics routine as a bin scheme, and (b) this study's focus is whether a unified category bulk scheme (U-AMP) can mitigate some of structural disadvantages that traditional separate category bulk schemes (S-AMP) are known to suffer. A bin scheme, which also serves as the microphysics routine for both U-AMP and S-AMP, is therefore required as a reference to judge which bulk scheme performs better. We specifically use two reference bin schemes because we recognize that neither is perfect. Future studies that attempt to assess the performance of an operational bulk scheme should still use observations as the benchmark.

The set of base test cases in KiD are largely inherited from HI23 (Table 4), which includes all 16 combinations of aerosol concentration $N_a = \{100, 200, 400, 800\}/mg$ and maximum vertical velocity $w_{max} = \{2, 4, 8, 16\}\ m/s$, as shown in Table 4. This covers a wide range of background aerosol conditions from maritime ($100/cc$) to continental ($800/cc$) and dynamic conditions from calm ($2\ m/s$) to vigorous ($16\ m/s$). These cases are based on the built-in test case #101 which mimics a shallow convective cloud (see KiD documentation, which prescribes the evolution of vertical velocity and initialize with a profile of water vapor mixing ratio shown in. The time step is set to 0.5 second, and the thickness of each vertical layer is a constant of 50 meters. For convenience, a particular case will be referred to in the form of, for example, Na400w02, for the case $N_a = 400\ mg, w_{max} = 2\ m/s$. The evolution of liquid water content and surface precipitation rate of this case run with bin-SBM can be viewed in Figure 4.2.

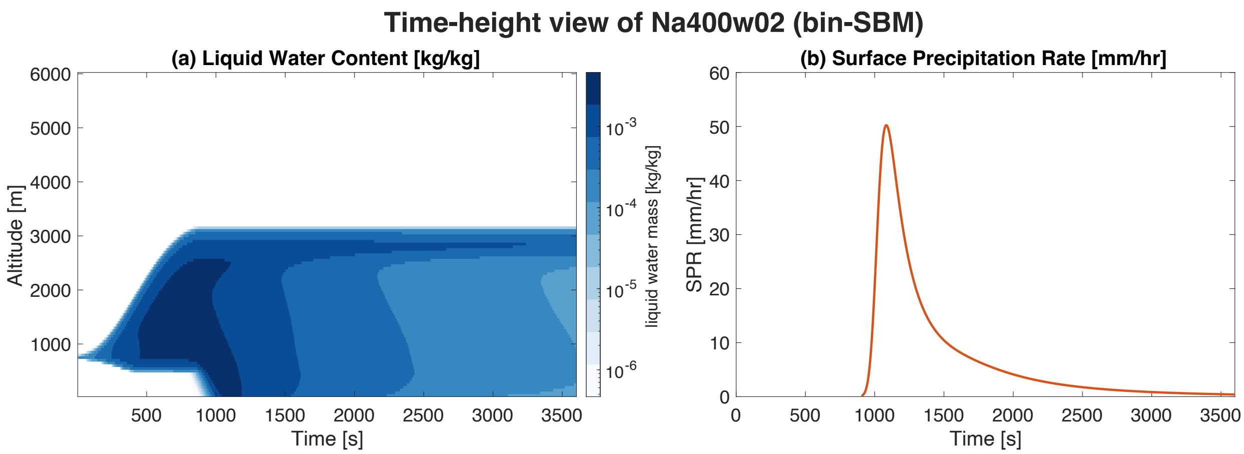

Figure 4.2. A time-height view of (a) liquid water content and (b) surface precipitation rate of the case Na400w02

For Q1 (search for the best U-AMP configuration), we use all 16 cases and vary the predicted moments (M_x, M_y) and assumed shape parameter (ν_1, ν_2). All simulations are run with full microphysics, i.e., condensation, evaporation, collision-coalescence, and sedimentation. Both M_x and M_y can be any distinct pair of numbers between 1 and 9 (except 3 since the 3rd moment, mass, is always predicted). Assumed shape parameters ν_1 and ν_2 can take any value from the set $\{2, 4, 6, 9, 12\}$. In total, 700 different configurations (28 moment combinations and 5 shape parameters for each mode) of U-AMP are tested for each of the 16 cases. A "similarity score" (S) is proposed to evaluate how good AMP is at representing bin scheme's simulation for each configuration and for each quantity of interest (CWP, RWP, LWP, SPR, $D_{m,r}$), which is calculated as follows:

$$S = 1 - \frac{\sum(Q_{AMP} - Q_{BIN})^2}{\sum\left(Q_{BIN} - \overline{Q_{BIN}}\right)^2}, \qquad (4.3)$$

Where Q represents the value of a particular quantity, the subscript denotes whether the value is from AMP or BIN, and $\overline{Q_{BIN}}$ is the mean value of Q_{BIN} across the entire simulation.

The definition is based on that of coefficient of determination (R^2), meaning that S peaks at 1 if AMP perfectly mimics the bin scheme (i.e., $Q_{AMP} = Q_{BIN}$ is always true). Unlike R^2, S can be negative if the results from AMP and bin are vastly different. This metric accounts for both the magnitude of Q_{AMP} and its timing relative to Q_{BIN}. In general, errors in timing are penalized more heavily with this metric than errors in magnitude. Finally, the best configuration of $\{M_x, M_y, \nu_1, \nu_2\}$ is determined by the highest total score after summing up the results of all 16 cases.

To evaluate the performance of U-AMP compared to S-AMP, we also use the set of cases in Table 4. The similarity score is evaluated for each case and each quantity of interest as a metric to compare whether one scheme consistently outperforms the other. A mean similarity score across all 16 cases is calculated to visualize which quantity of interest gain the most score by switching from S-AMP to U-AMP. The mean score is weighted by the mean value of the quantity of each case so that large error in a negligible quantity does not overwhelm the overall similarity score. Note that we have also run a suite of simulations to optimize the S-AMP configuration. The best configuration of S-AMP is presented throughout the study.

Table 4. Suite of KiD simulations and their respective peak surface precipitation rates from bin-TAU, which are similar to bin-SBM. The units are m/s for w_{max}, 1/mg for N_a, and mm/hr for surface precipitation rate.

N_a \ w_{max}	2	4	8	16
800	7.56	23.3	54.8	117
400	7.29	23.2	55.0	116
200	7.25	23.1	55.4	115
100	7.25	23.0	55.7	117

4.4 Results

When configured optimally in KiD, unified category AMP (U-AMP) is found to be far superior compared to the separate category (S-AMP) when estimating precipitation rate, with which S-AMP struggles the most. U-AMP is also on par with S-AMP in other quantities such as CWP, RWP, and LWP, for which S-AMP already makes almost perfect predictions when compared to the bin schemes. Estimates of mean raindrop size from both U-AMP and S-AMP also have roughly the same similarity score. Mean similarity scores across all 16 test cases are calculated for each quantity of interest and is shown in Figure 4.3.

We present a thorough investigation of how the selection of moments and assumed shape parameter of the gamma distribution affects the U-AMP's reproducibility of bin microphysics in Section 4.1, and how it compares to S-AMP (which follows the traditional separate categorization of cloud and rain category) in Section 4.2. When using the bin schemes as the reference, we find overall the best moment combination is $\{M_3, M_0, M_4, M_5\}$ and the best assumed shape parameter is 2-2 ($\nu_1 - \nu_2$) for SBM and 4-4 for TAU. This substantial improvement over the traditional method could mark the beginning of a paradigm shift for bulk schemes.

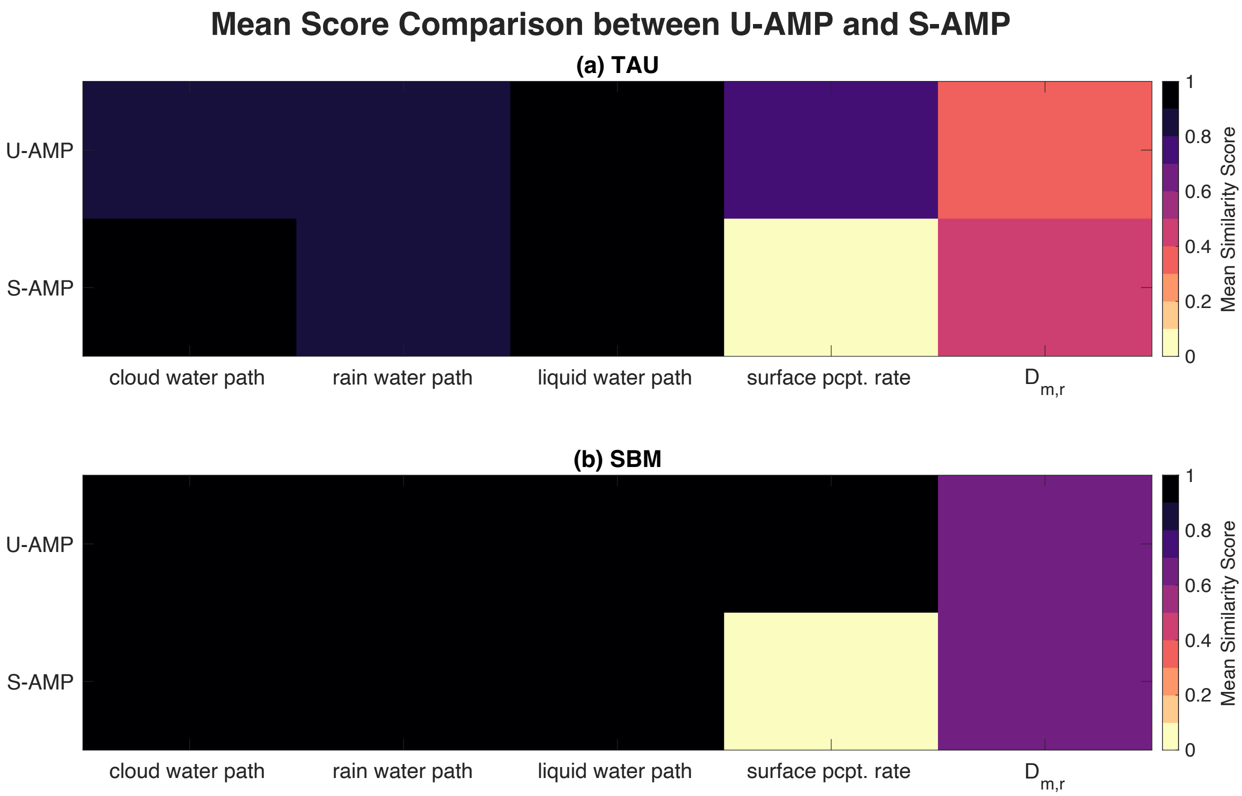

Figure 4.3. A summary of the weighted mean scores of different quantities of interest.

4.4.1 Best U-AMP Configuration

To find the best moment combination and shape parameter configuration for U-AMP, we test the aforementioned 700 configurations in all 16 test cases that produce rainfall in both bin-TAU and bin-SBM. One similarity score is calculated for each quantity of interest and for each U-AMP configuration. A heat map of similarity scores can be generated for each case to highlight the best configurations for that case. As illustrated in Figure 4.4, to get the most adaptable configuration that works for as many cases as possible, the heat maps from the 16 cases are summed up into one composite heat map, which can be seen in Figure 4.5 for surface precipitation and Figure 4.6 for rain water path. See the supplemental information for similar heat maps for LWP and CWP (Figure 4.10 and Figure 4.11).

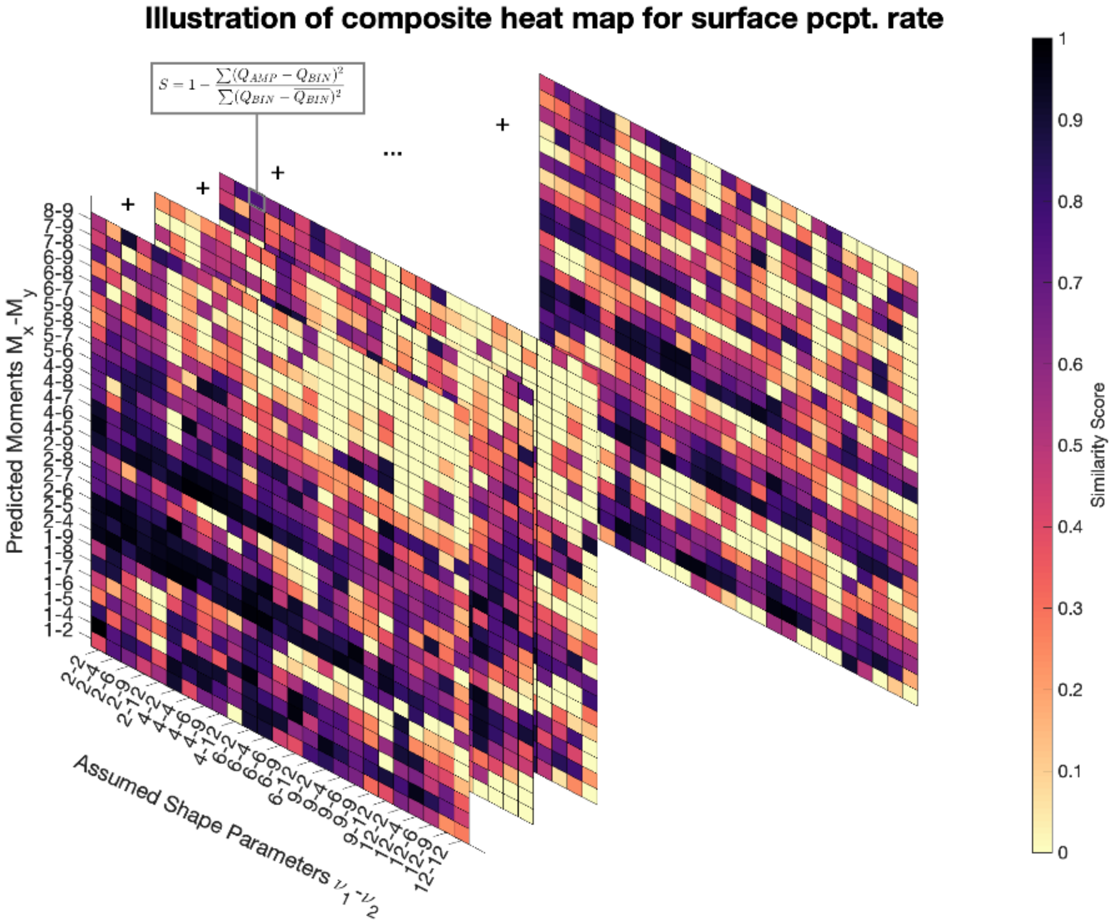

Figure 4.4. An illustration of how the composite score in Figure 4.5 is calculated. Each simulation is summarized in a grid, whose color represents its similarity score according to Eq. 4.3. Each vertical slice shows a matrix of similarity scores for all 700 configurations from 1 of 16 initial conditions in Table 4. For brevity, only 4 are shown out of a total of 16 cases. The composite score is calculated by summing up the similarity scores across all 16 cases.

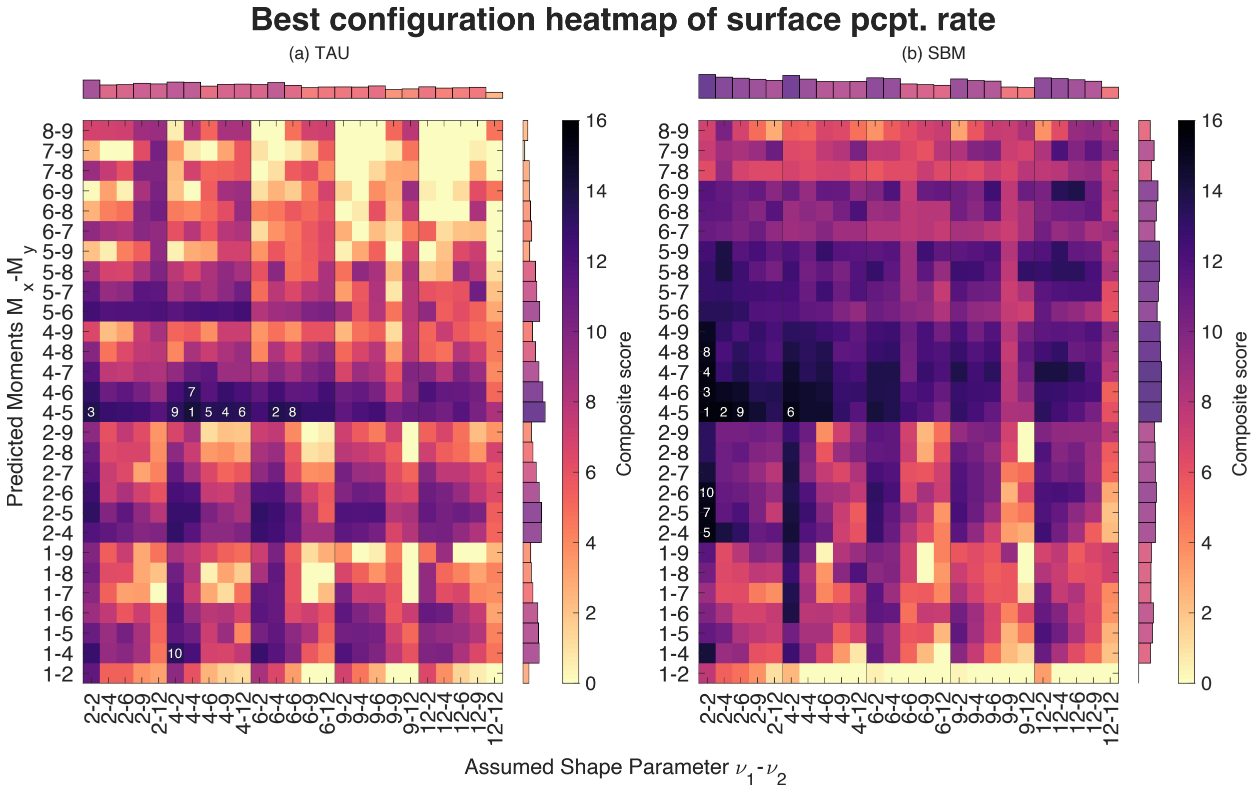

Figure 4.5. A heatmap of composite score showing the best predicted moments and assumed shape parameter configuration for minimizing error in surface precipitation rate across all 16 precipitating cases. The best 10 configurations are marked with their respective ranking in the grid. The bar graphs above and to the right of the heat map show the mean scores by assumed shape parameters and by moment combinations.

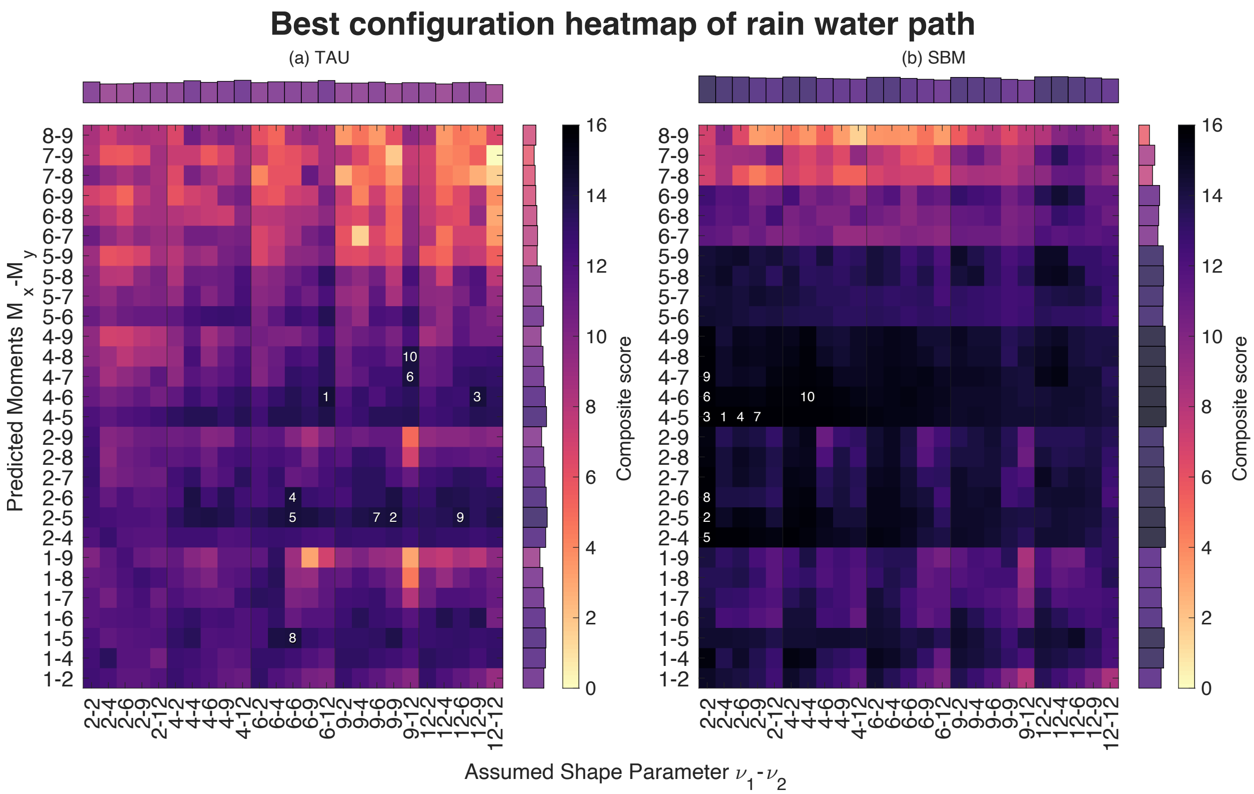

Figure 4.6. As in Figure 4.5 but for rain water path.

The best assumed shape parameter is found to depend on both the choice of bin scheme and the quantity of interest. U-AMP's best configuration for surface precipitation rate (Figure 4.5) suggests that it is not sensitive to ν_1 but strongly prefers ν_2 to be small, which translates to a wider distribution for the L2 (collector) drops. This is likely because the two processes most relevant to precipitation, collision-coalescence and sedimentation, both broaden the L2 distribution to the extent that requires ν_2 to be as low as 2 or 4 for maximum similarity between U-AMP and bin. The shape parameter of the L1 mode (as the collected drops), on the other hand, is mostly controlled by condensation and is therefore not as constrained as ν_2. This finding is robust as it is observed when using both bin schemes.

Regarding rain water path (Figure 4.6), U-AMP-TAU and U-AMP-SBM do not agree on the choice of the optimal shape parameter. TAU generally prefers ν_1 to be large (9-12) while SBM prefers it to be small (2-4). Upon closer inspection, this discrepancy stems from the fact that TAU and SBM generate different L1 (cloud-sized droplets) mode widths through condensation. It is already known (e.g., HI23) that TAU generates much narrower distribution than SBM due to TAU's 2-moment bin structure that partially mitigates the numerical broadening issue. As shown in (Fig), the L1 modes from TAU and SBM have vastly different widths, which then leads to a different rain production rate due to path dependence. The seemingly different U-AMP's preferences on higher ν_1 (narrow L1 distribution) is therefore merely a projection of TAU-SBM's structural differences and parameterization differences in the condensation routine.

For predicted moments, the two heat maps (Figure 4.5 and Figure 4.6) suggest that the best moments to predict are near M_3 ($M_2 - M_5$), regardless of the bin scheme of choice. This is somewhat different from the results from the previous study using the same AMP scheme (I22), which showed that moments of order higher than M_6 can be equally good or better, and Section 4.2 of I22 even suggested that a M_9 is necessary to predict to maximize information content and minimize errors. However, the full microphysics tests in this study show that $\{M_2, M_4, M_5\}$ are the most desirable moments to predict while moments higher than M_6 generally have a worse performance (lower similarity score). Since these moments are not associated with any known conserved quantities, the reason why $\{M_2, M_4, M_5\}$ are advantageous is likely because they individually capture an important aspect of the PSD while not being oversensitive to the largest droplets, which could lead to numerical instability in practice.

Even though M_4 and M_5 are not in the top 10 best configuration when estimating RWP using TAU, its mean score across all shape parameters is among the best. Combined with surface precipitation rate and other quantities such as LWP (see Figure 4.11), we find that $\{M_3, M_0, M_4, M_5\}$ is the best moment combination to predict and 4-4 (TAU) or 2-2 (SBM) are the best assumed shape parameters. We also use a similar approach to obtain the best assumed shape parameter for S-AMP, which is 4-4 for SBM and 10-10 for TAU. All U-AMP vs. S-AMP tests below will adopt these configurations.

4.4.2 U-AMP vs. S-AMP in KiD

We next investigate the reasons why U-AMP can perform so much better than S-AMP in surface precipitation rate even though the schemes' performance in RWP and other metrics is similar. U-AMP's and S-AMP's ability to replicate the bin scheme is evaluated with the similarity score for rain water path (RWP) and surface precipitation rate (SPR) across the 16 test cases (Figure 4.7). Comparison of the time series of these two quantities are also plotted for two specific cases: Na100w04 and Na400w08.

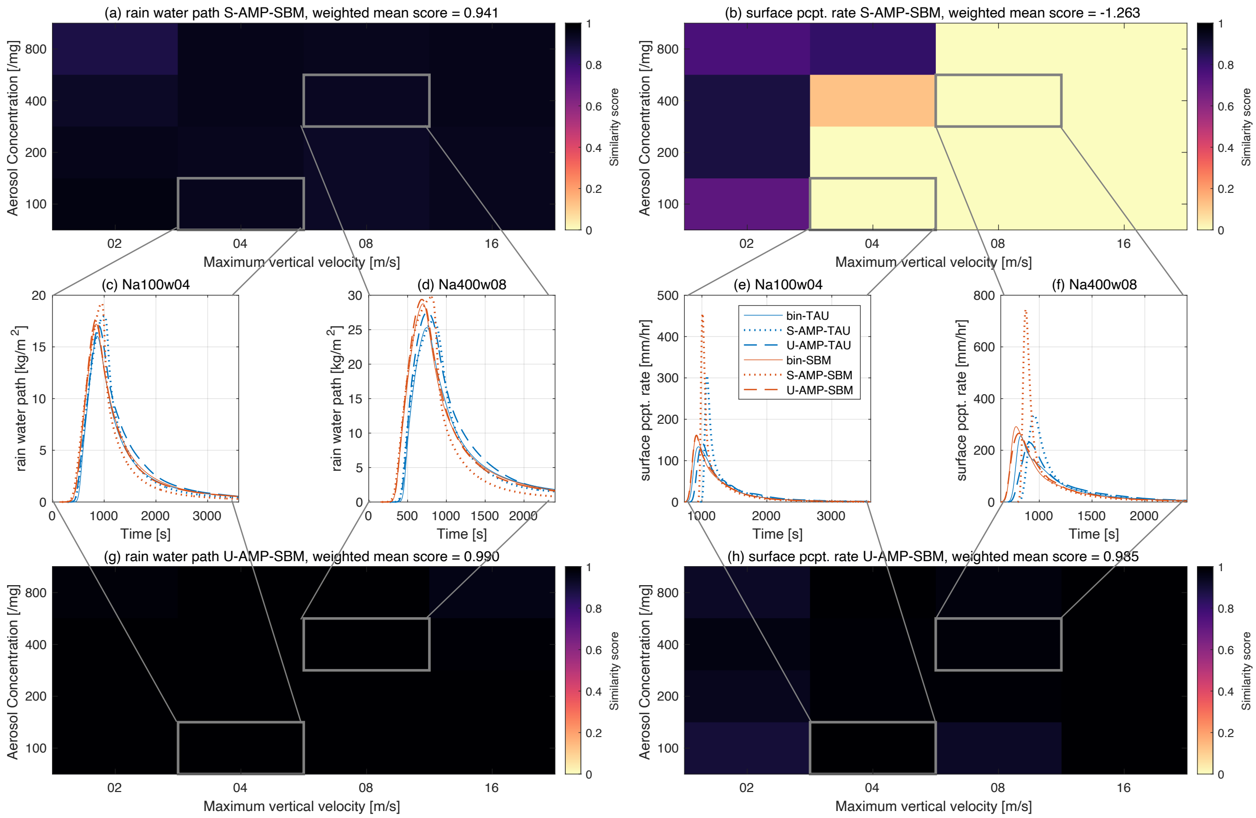

Figure 4.7. Scores of all full microphysics cases (Table 4) for rain water path (a, g) and surface precipitation rate (b, h). Two specific cases from two different regimes (Na100w04 and Na400w08) are selected to be plotted in the middle (c, d, e, f). All scores used here in this figure (a, b, g, h) are from SBM. Interested readers are referred to the supplemental information (Figure 4.12) for the same figure but with scores from TAU.

The similarity scores of CWP and LWP (Figure 4.13) by U-AMP are found to be generally on par with S-AMP since they are mostly controlled by condensation, which only has a meaningful effect on the L1 (cloud) mode and thus is not affected by the treatment of the liquid water category. U-AMP achieves a slightly higher mean similarity score in RWP and a similar score in $D_{m,r}$ compared to S-AMP. The time series plots (Figure 4.7c, d) confirm this finding, with U-AMP being marginally more bin-like compared to S-AMP in RWP and less bin-like in CWP. This small difference in RWP can be traced to their vastly different surface precipitation rates, which are much better represented with U-AMP compared to S-AMP in all SBM cases (Figure 4.7b, h). The time series plots (Figure 4.7e, f) of two cases show that U-AMP clearly outperforms S-AMP in their estimates of both the peak intensity and the timing of the precipitation. This stark difference marks U-AMP's clear advantage over S-AMP in predicting precipitation. The same visualization for TAU is shown in Figure 4.12, which qualitatively shows the same tendency in precipitation as SBM, but U-AMP's mean score in RWP is slightly lower than S-AMP since the assumed shape parameter chosen for this simulation ($\nu = 4$) is much lower than the optimal shape parameter for estimating RWP ($\nu \sim 10$).

A closer look into the evolution of the PSD reveals the reason why U-AMP is structurally superior compared to S-AMP when simulating certain precipitation patterns. Figure 4.8 shows a snapshot of the case Na200w04 at $t = 800\ s$. Although both U-AMP's and S-AMP's RWP closely match that of the BIN (Figure 4.8a), S-AMP struggles to allow the rain aloft to fall as quickly as U-AMP or BIN. Their respective PSD (Figure 4.8c-e) suggests that the underlying reason for S-AMP's slow sedimentation could be its explicit liquid water categorization. As large raindrops aloft fall through a layer below with smaller raindrops, a bimodal distribution can emerge *within* S-AMP's predefined rain category (diameter > $80\ \mu m$). Such a bimodal distribution cannot be modeled by S-AMP since it only allows one gamma distribution (one mode) to exist in the rain category. This restriction forces the original bimodal distribution into a new unimodal one with its peak between the two original modes, which annihilates the fast-falling largest raindrops, leading to a pent-up and delayed burst of precipitation, which can be seen in Figure 4.8b. The same visualization for TAU can be found in Figure 4.15 in the supplemental information.

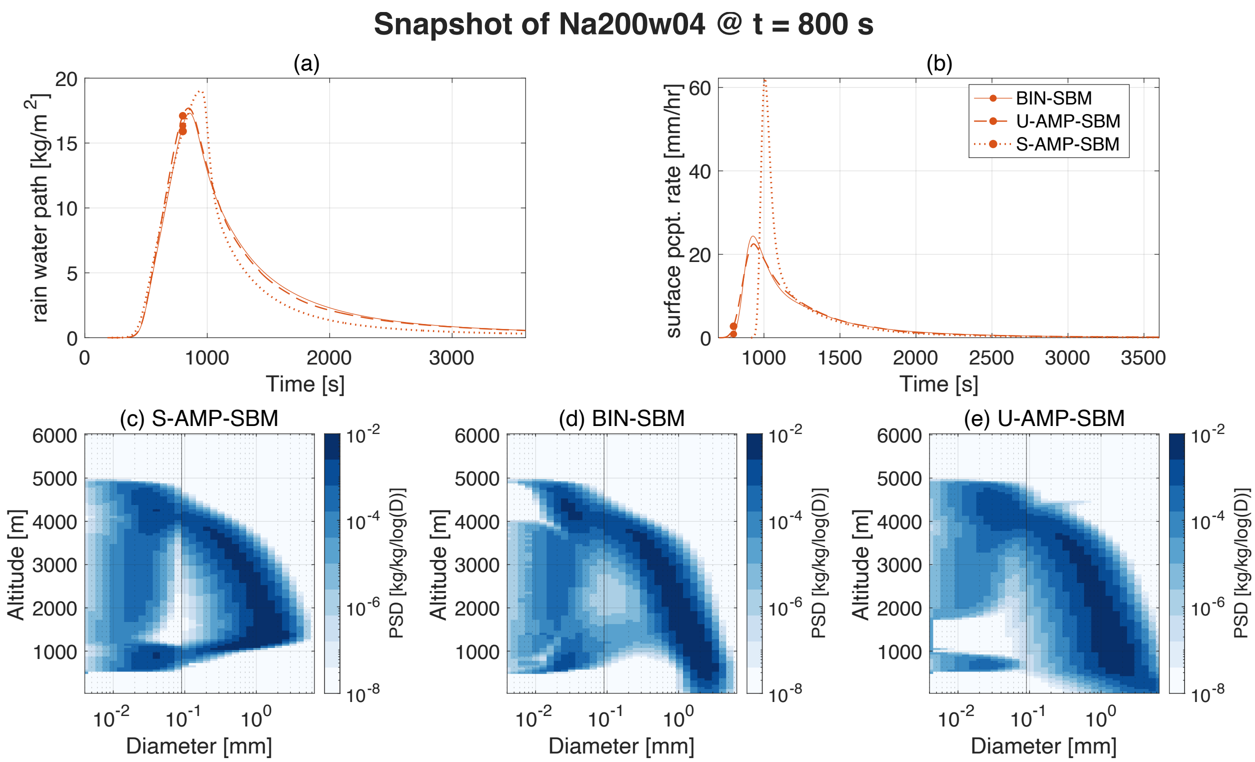

Figure 4.8. Time series of (a) rain water path and (b) surface precipitation rate of BIN-SBM (solid), U-AMP-SBM (dashed), and S-AMP-SBM (dotted). Snapshots of the PSD of (c) S-AMP-SBM, (d) BIN-SBM, and (e) U-AMP-SBM at t = 800 s. The solid gray vertical line in (c-d) marks the cloud-rain size boundary in S-AMP.

A sedimentation only simulation is performed to illustrate that S-AMP's delayed precipitation is indeed a direct result of the sedimentation process. The initial PSD profile (Figure 4.9a) consists of two layers of rain, one between 600 m and 2400 m with mean diameter of 200 μm and another one between 2400 m and 7000 m with linearly increasing liquid water content and a mean diameter of 600 μm. The configurations for U-AMP and S-AMP are inherited from Section 4.1. As can be seen in Figure 4.9c-e, U-AMP successfully reproduces BIN's bimodal characteristics within the canonical rain category, whereas the large mode in S-AMP slowly falls through the layers below while merging with the small raindrop mode to form a unimodal distribution. The time series of the surface precipitation rate (Figure 4.9b) shows a similar story to the full-microphysics setup above (Figure 4.8b and Figure 4.15b), where S-AMP holds onto the rain water mid-air much longer than U-AMP and BIN. This test suggests that, even without the challenges of autoconversion, separate category bulk schemes still face challenges when predicting precipitation in certain conditions, which highlights U-AMP's clear structural advantage in handling situations where multiple modes exist within the traditional rain category. The same visualization for TAU can be found in Figure 4.16, which shows the same features as SBM case and validates the robustness of this explanation.

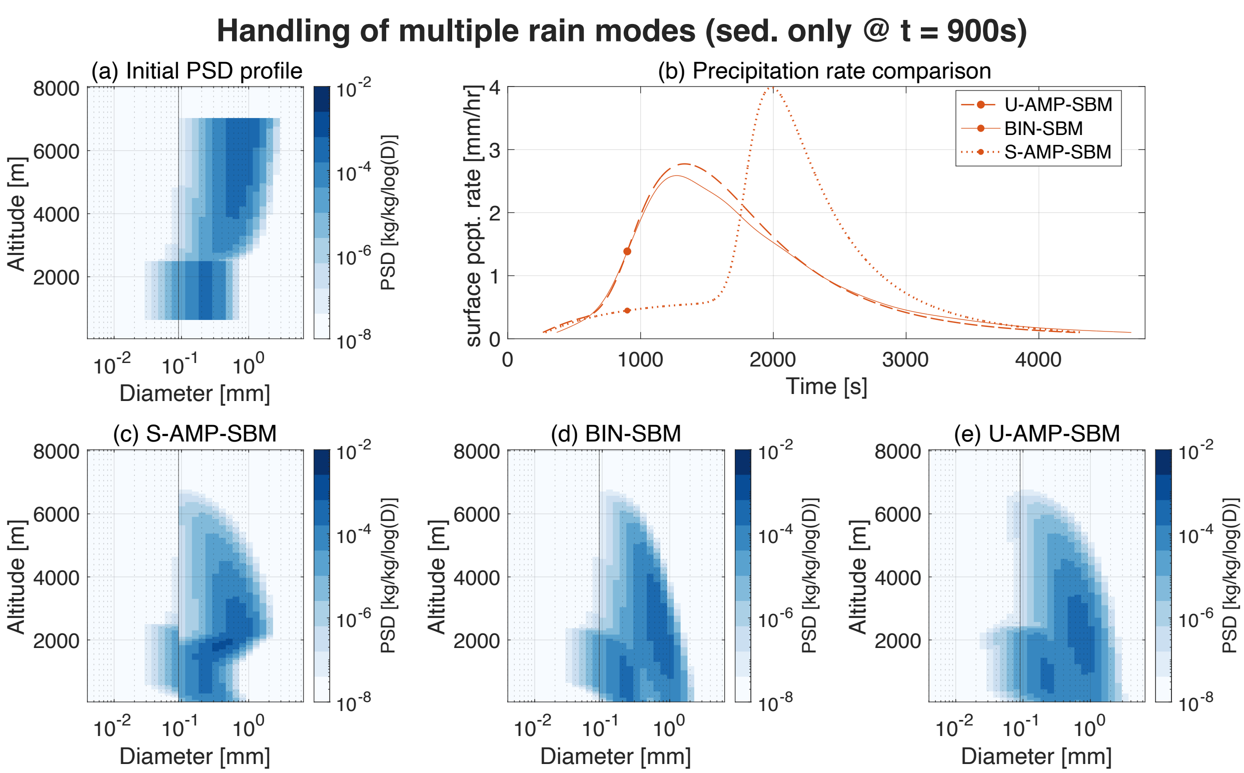

Figure 4.9. Time series of precipitation rate (b) of a sedimentation-only case starting from the PSD profile shown in panel (a). Snapshots of the PSD of (c) S-AMP-SBM, (d) BIN-SBM, and (e) U-AMP-SBM at t = 900 s.

4.5 Summary

This study uses AMP to explores the feasibility of a bulk scheme that adopts a unified liquid water category (U-AMP) and its advantages and disadvantages over traditional separate category bulk schemes (S-AMP). AMP is a bulk scheme that runs bin microphysics routines, which can also be their own standalone scheme and serve as the reference run for AMP to compare against. S-AMP prescribes a size boundary between the cloud and the rain category, fits a gamma distribution to each category, and concatenate the two distributions to obtain the full PSD. On the other hand, U-AMP does not prescribe a size boundary. Rather, it fits the entire PSD with a continuous bimodal distribution, which is constructed with a linear combination of two gamma distributions. The lack of size boundary allows the two gamma distributions in U-AMP to evolve without artificial limits on their sizes.

In this study, both S-AMP and U-AMP are run with assumed shape parameters for the two categories/modes, which means that four moments in total need to be predicted. Unlike S-AMP (or any other traditional separate category bulk scheme), which predicts the mass (3^{rd} moment) and number (0^{th} moment) of both cloud and rain categories, U-AMP needs to predict four distinct moments as it does not partition liquid water into subcategories. An extensive exploration is therefore required on how the selection of moments and assumed shape parameter of the gamma distribution influence U-AMP's replication of bin scheme.

After testing 700 different configurations (28 moment combinations and 5 shape parameters for each mode) across the 16 KiD test cases with different initial aerosol concentration and maximum vertical velocity ($N_a = 100 - 800/mg, w_{max} = 2 - 16\ m/s$), we find that the best moments to predict are the 4th and the 5th moment. This is likely because it provides enough information about the larger mode of the PSD while not being overly sensitive to the largest droplets, which could cause numerical instability. The best assumed shape parameters for U-AMP are found to be 4-4 ($\nu_1 - \nu_2$) in TAU and 2-2 for SBM. A similar approach is done to find the best assumed shape parameters for S-AMP, which is found to be 12-12 for TAU and 4-4 for SBM.

Using this configuration, U-AMP far outperforms S-AMP in estimating precipitation rate, an area where S-AMP struggles significantly. U-AMP also performs similarly to S-AMP in predicting quantities like cloud water path (CWP), rain water path (RWP), and liquid water path (LWP), where S-AMP already makes near-perfect predictions compared to bin schemes. U-AMP's superiority over S-AMP in simulating certain precipitation patterns is likely due to its ability to handle situations where multiple modes exist within the traditional rain category ($D > 80\ \mu m$). This can be common when large raindrops fall through a layer with much smaller raindrops. In this case, since S-AMP is unable to separate the two modes within the rain category, it artificially combines the two separate rain modes into one, which annihilates the fast-falling largest raindrops, leaves smaller raindrops mid-air for longer, and ultimately leads to a pent-up and delayed burst of precipitation. U-AMP, on the other hand, avoids this problem as it can reproduce the bimodal characteristics within the rain mode more accurately. This explanation is validated by a sedimentation-only test, which reproduces the delayed precipitation in S-AMP and near perfect emulation by U-AMP.

In summary, the results in this study suggests that U-AMP, or unified category bulk schemes in general, has significant improvements over traditional separate category bulk schemes, specifically in situations where multiple modes exist in one traditional category (rain category in this study and cloud category in I22). Such structural improvement could mark the beginning of a shift in the paradigm for bulk scheme development. Future study could include putting U-AMP into more sophisticated models with feedbacks between microphysics and thermodynamics. Designing an operational unified category bulk schemes would also be of great interest as the ultimate goal of this new structure is to improve weather and climate prediction with a scheme that does not considerably increase the computational cost.

4.6 Supplemental Information

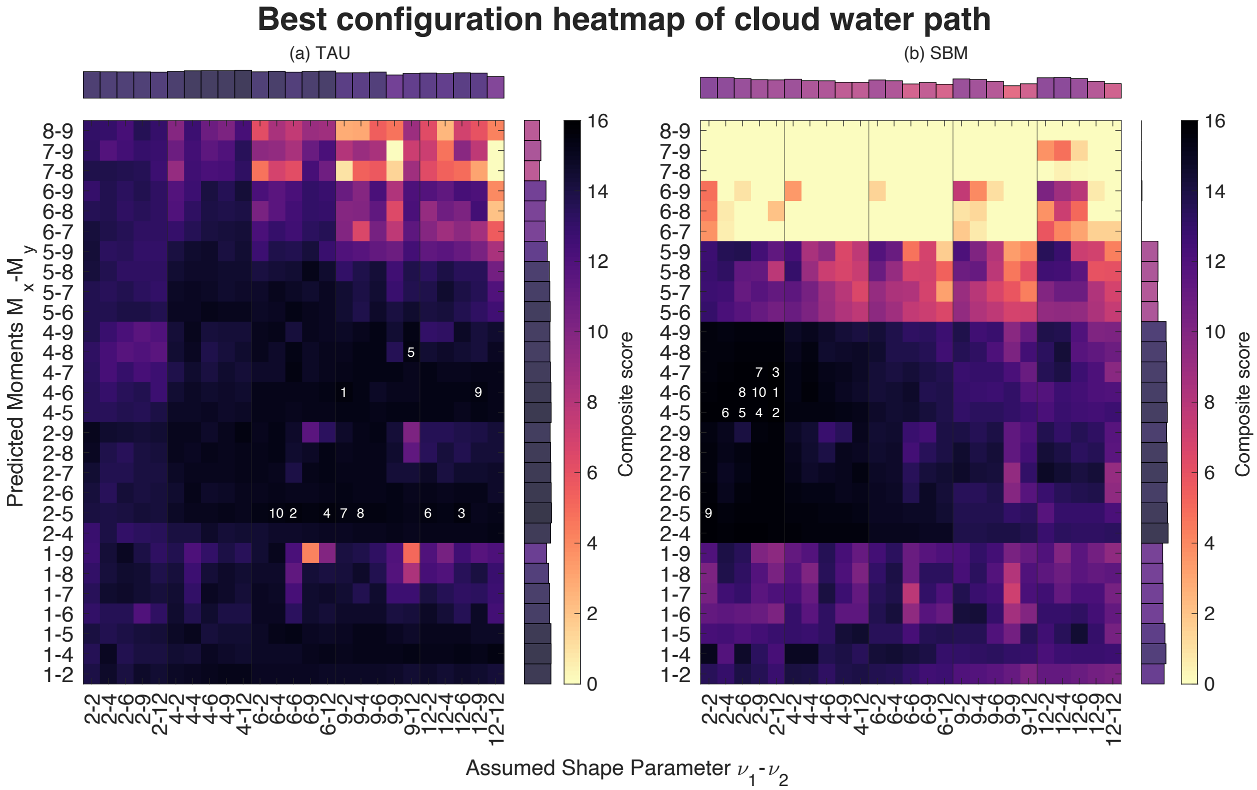

Figure 4.10. As in Figure 4.5 but for cloud water path.

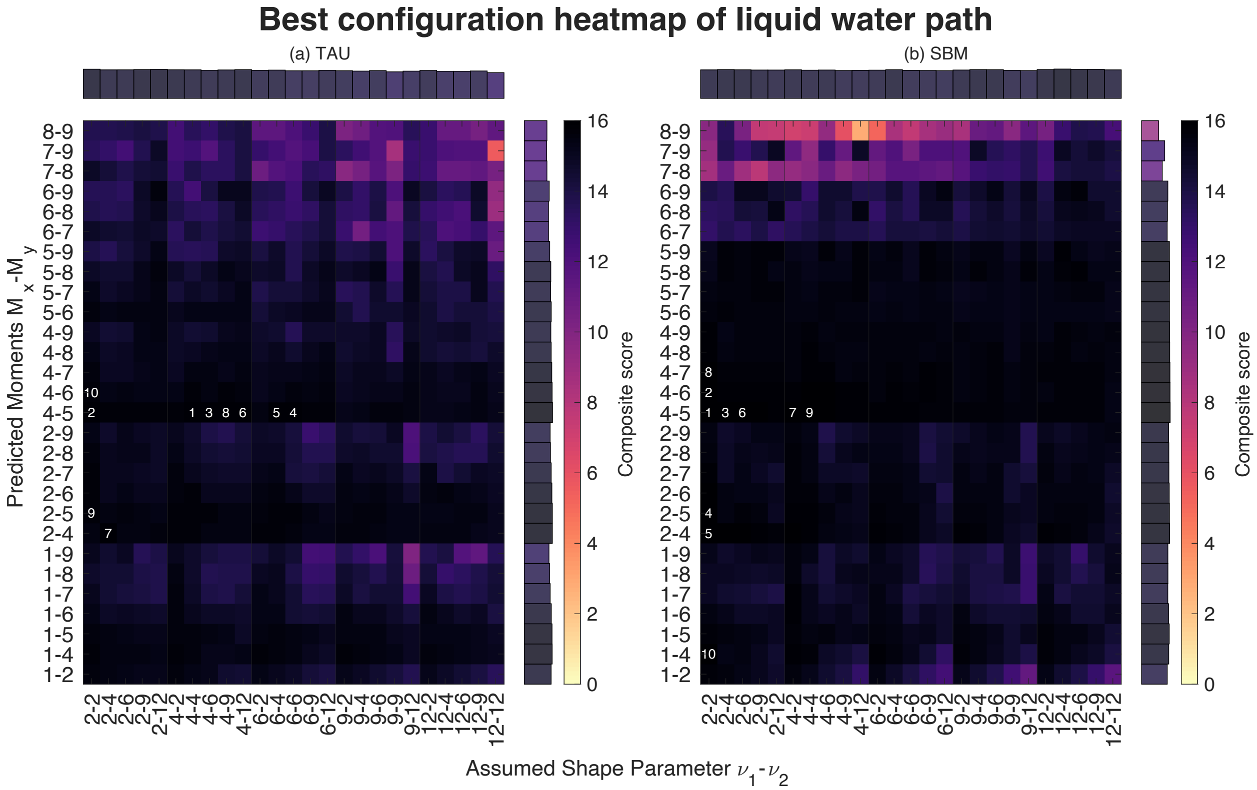

Figure 4.11. As in Figure 4.5 but for liquid water path.

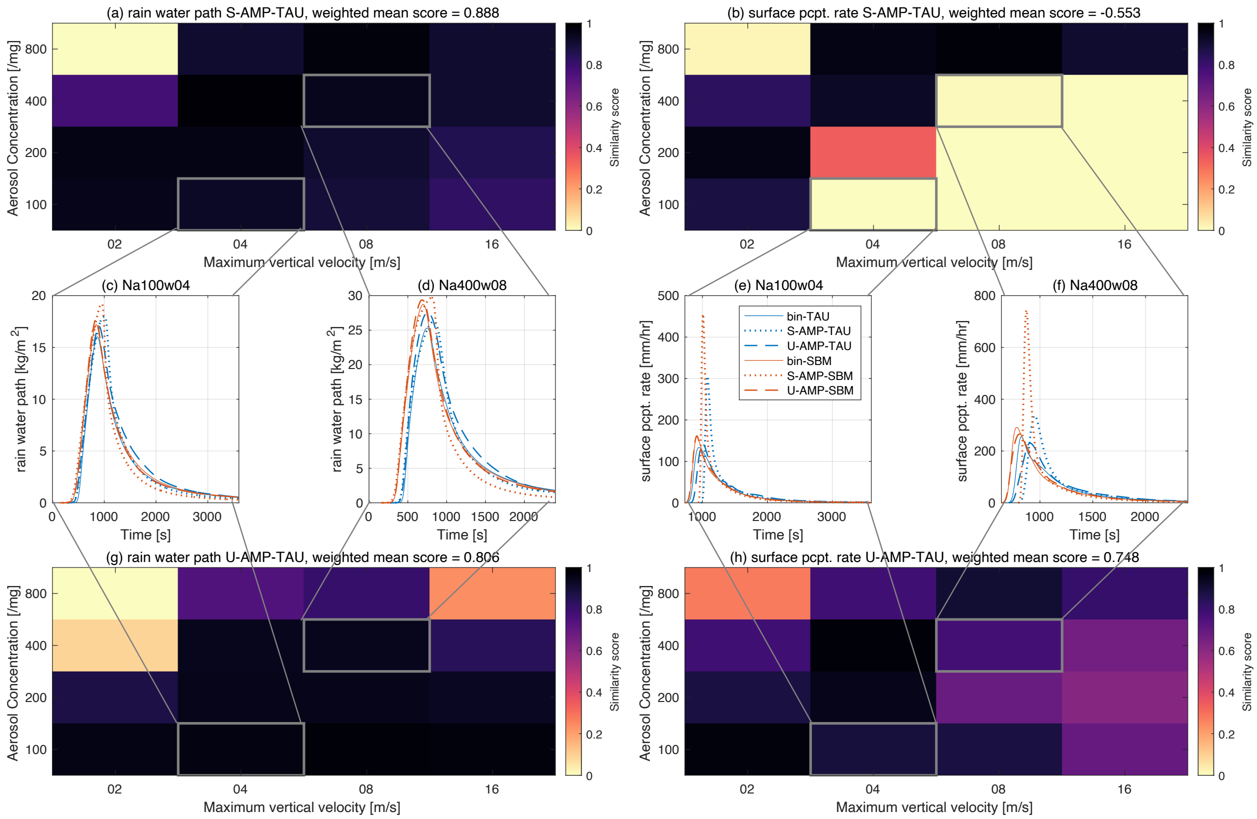

Figure 4.12. As in Figure 4.7 but for TAU.

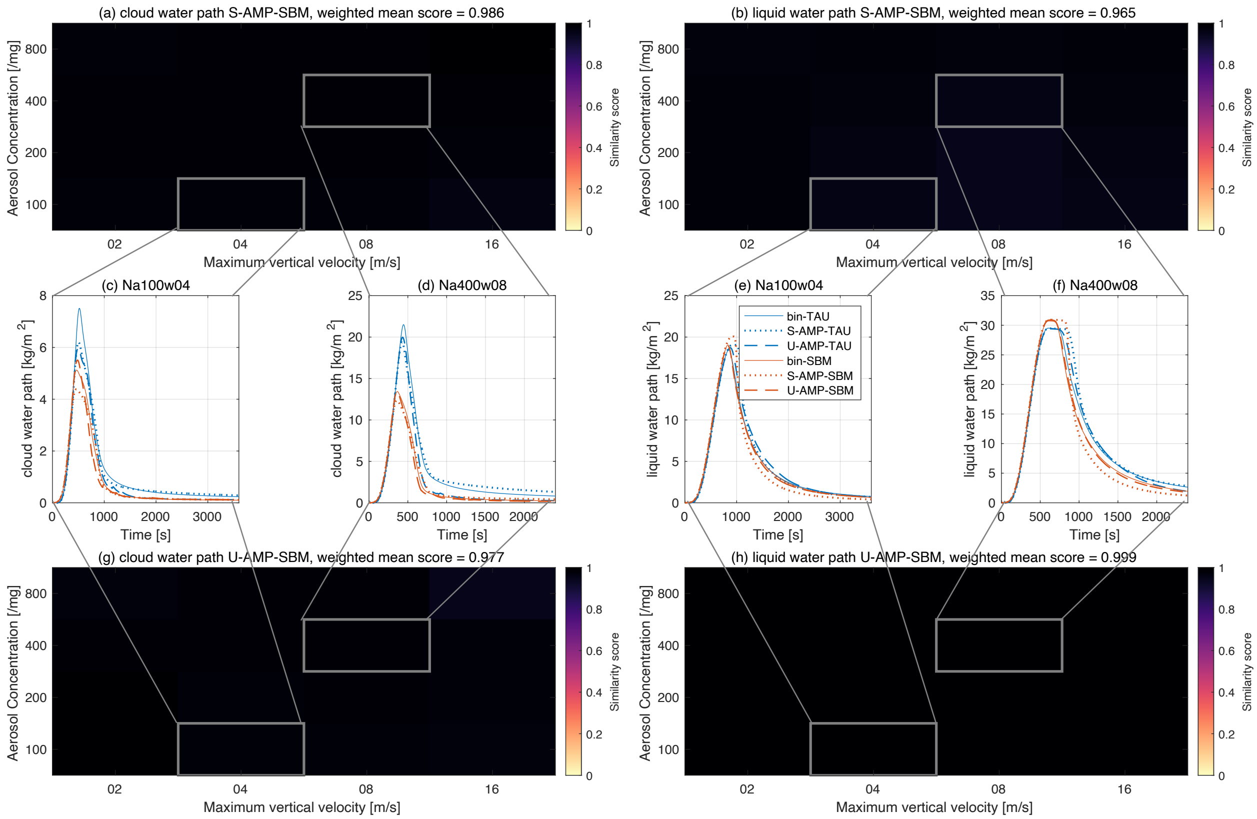

Figure 4.13. As in Figure 4.7 but for cloud water path and liquid water path.

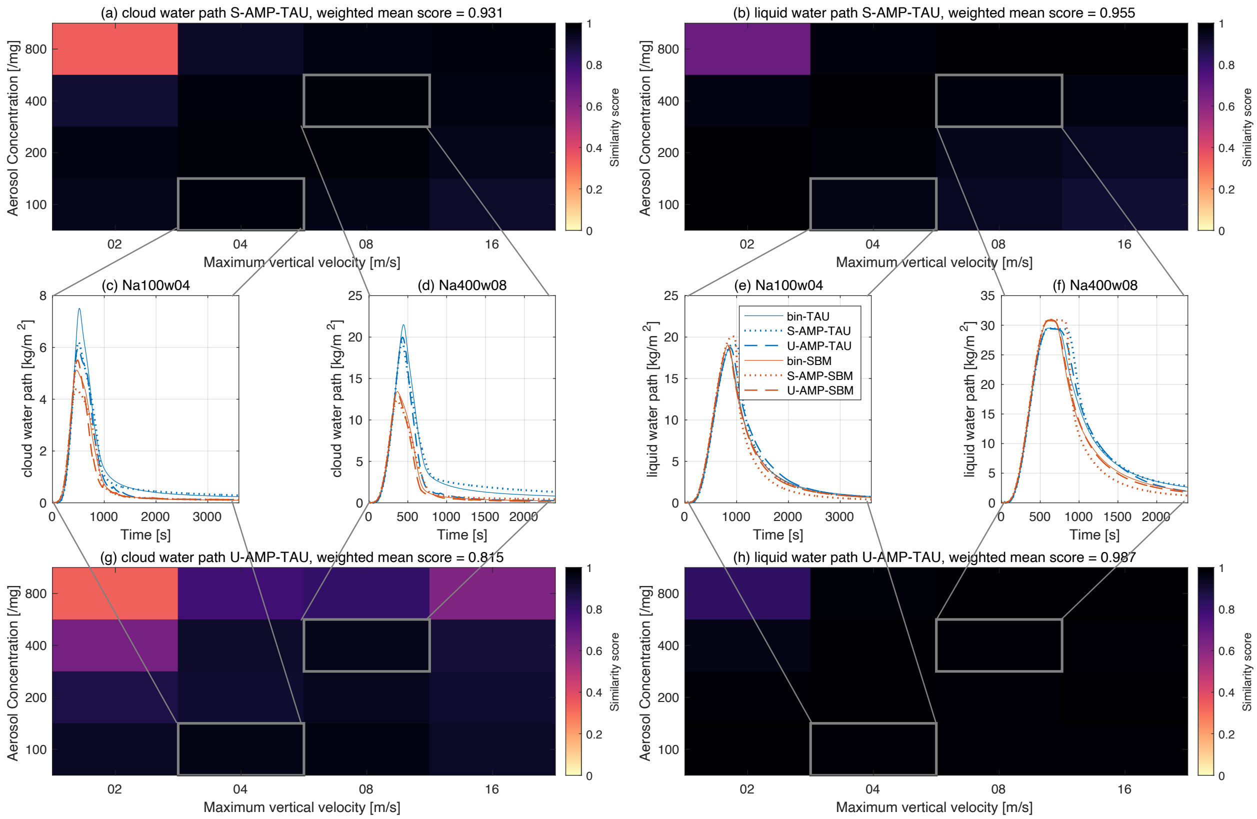

Figure 4.14. As in Figure 4.13 but for TAU.

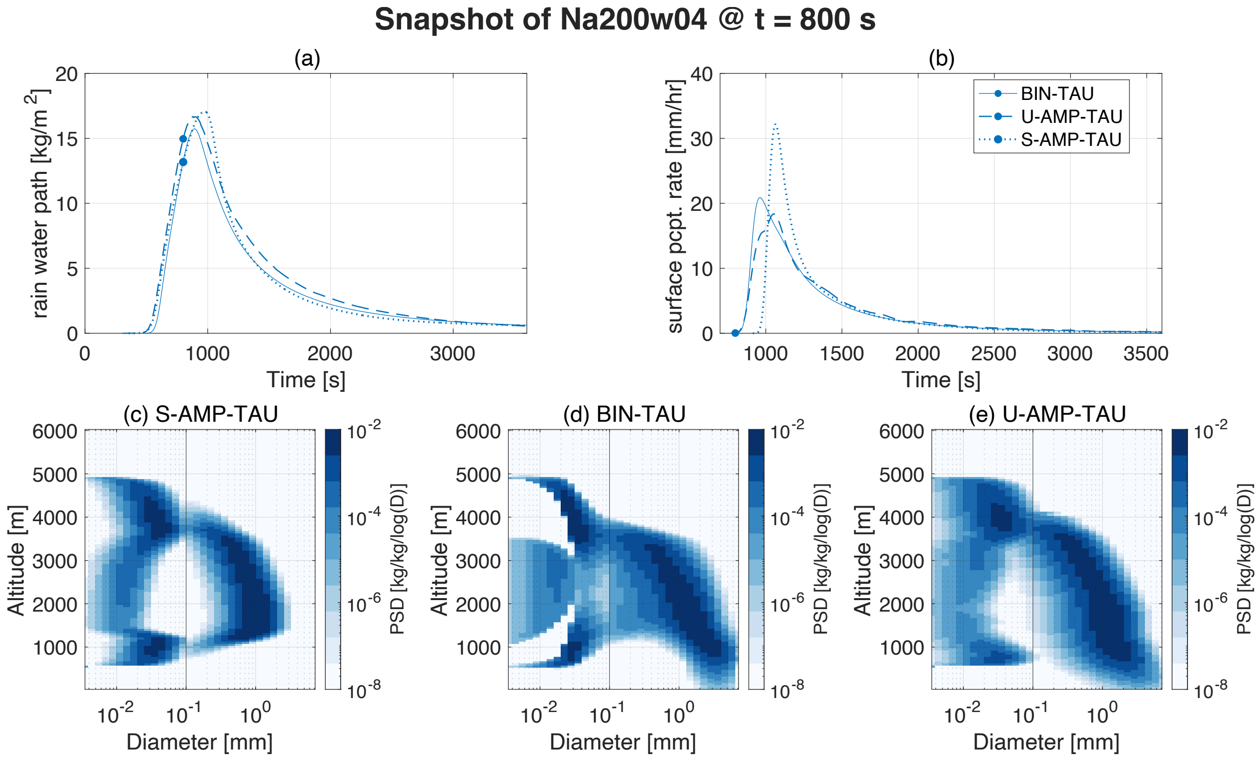

Figure 4.15. As in Figure 4.8 but for TAU.

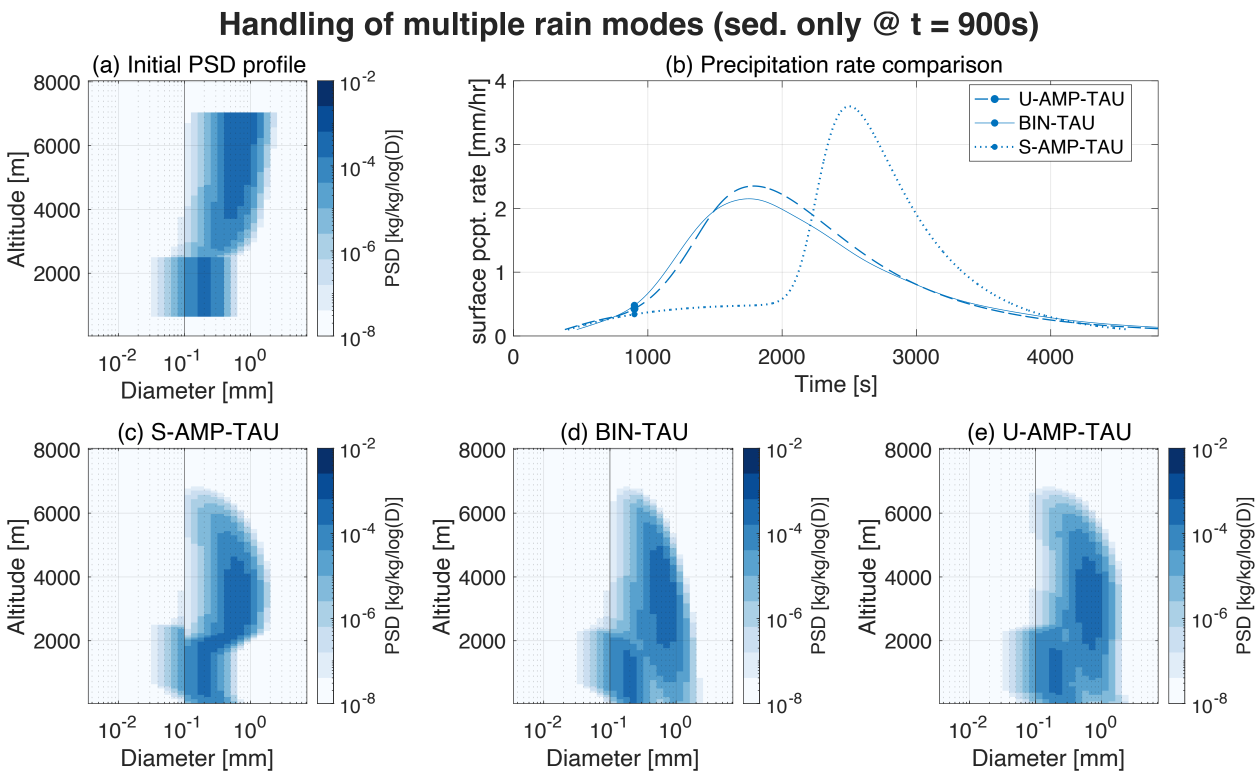

Figure 4.16. As in Figure 4.9 but for TAU.

5 Conclusions

This dissertation focuses on guidance on the future development in bulk microphysics scheme based on both observational and modeling results. Specifically, we aim to address the following questions:

1. Why do past studies on the subject of aerosol-dispersion effect not show a consistent correlation between aerosol number and droplet dispersion? Is there an empirical correlation we can use to diagnose the relative dispersion in a bulk microphysics scheme?
2. What is the effect of the structural difference between a bin scheme and a bulk scheme on their simulation results and how does it compare to the parameterization difference between two different bin schemes? Which process is the most susceptible to the bin-bulk structural difference and leads to the biggest discrepancy?
3. Is a bulk scheme with unified liquid water category feasible for predicting the evolution of a cloud? What would be the best configuration regarding its predicted moments and assumed shape parameters? Would it consistently outperform a traditional bulk scheme with separate liquid water category, using bin schemes as the references?

5.1 Aerosol-Dispersion Effect

This chapter reconciles the inconsistent sign of the correlation between aerosol number concentration and droplet size relative dispersion found in different studies in the past. Our insight was to distinguish local correlation from cloud-mean correlation. We find that, at the cloud-mean level, a correlation between aerosol concentration and relative dispersion is largely nonexistent, but in-cloud regions with high relative dispersion are commonly correlated with low local droplet concentrations. A more robust correlation is observed in relation to the local activation fraction, defined as the ratio of droplet concentration to the combined total of droplet and aerosol concentration. These observations of local correlation have guided us to propose a new equation to diagnose the shape parameter in marine stratocumulus clouds, specifically for double moment bulk schemes in cloud-resolving models or large-eddy simulations. The new equations proposed offers a more accurate physical representation than many existing equations that are based on the weak cloud-mean correlation.

5.2 Bin vs. Bulk Microphysics Scheme

This study examines the differences in cloud and precipitation characteristics simulated by bin and bulk schemes, which are the two main tools for parameterizing cloud microphysical processes. We employ a bulk schemes called Arbitrary Moment Predictor (AMP), which utilizes the same process parameterizations as a bin scheme but predicts only the moments of the size distribution like a bulk scheme. As such, differences between the results of simulations using AMP's bin scheme and AMP itself are necessarily the direct implication of their structural differences. When applied to one-dimensional kinematic simulations, the overall differences between AMP (bulk) and bin schemes are relatively minimal. Full-microphysics simulations reveal a close match in the mean liquid water path between AMP and bin (mean percent difference <4%), but AMP predicts a substantially lower mean precipitation rate (-35%) due to slower precipitation onset. In order to trace down the source of the discrepancy, we also run simulations with individual processes. Condensation is accurately represented by AMP, while minor differences between AMP and bin come from nucleation, evaporation, and sedimentation. Collision-coalescence is the most significant factor causing divergence between AMP and bin schemes. A detailed investigation indicates that the difference is primarily due to autoconversion rather than accretion. By reducing the diameter threshold separating the cloud and rain category in AMP from 80 to 50 μm in full microphysics simulations, the largest AMP-bin difference decreases to $\sim$10%. This suggests that the structural differences between AMP (and perhaps triple-moment bulk schemes in general) and bin schemes may be even less significant than the parameterization differences between the two bin schemes.

5.3 Unified Liquid Water Category Bulk scheme

This study explores the feasibility of a bulk scheme with unified liquid water category. We introduce it within the AMP framework (U-AMP) and comparing its advantages and disadvantages with the conventional, separate category bulk schemes (S-AMP). Systematically testing U-AMP for its optimal configuration reveal that the best moments predict are the 4th and 5th moment, which provides the most amount of information about the particle size distribution while avoiding numerical instability caused by the largest droplets. The best assumed shape parameters are identified to be 4-4 when TAU is used as the reference bin scheme and 2-2 under SBM.

Our findings suggest that, when configured optimally, U-AMP significantly outperforms S-AMP in predicting the timing and the peak rate of precipitation while performing comparably in estimating other quantities like cloud water path, rain water path, and liquid water path. U-AMP's superior performance in simulating specific precipitation patterns can be attributed to its better handling of situations with multiple modes within the traditional rain category. U-AMP's lack of categorization avoids the issue of artificially combining two separate rain modes, which is a limitation of S-AMP and leads to an unrealistic accumulation and delay of precipitation.

5.4 Future Directions

Given the promising results from U-AMP in predicting precipitation rates, it would be valuable to integrate U-AMP into more sophisticated models, such as the three-dimensional Colorado State Regional Atmospheric Modeling System (RAMS). This could help evaluate its performance with additional feedbacks between microphysics, thermodynamics, and radiation. Preliminary results show a similarly significant improvement in estimating precipitation using SBM as the underlying bin scheme (Figure 5.1). While U-AMP-TAU makes more bin-like predictions than S-AMP-TAU regarding total precipitation, it struggles to accurately predict the correct timing and peak rate of precipitation. However, the reason why S-AMP performs so poorly likely still stems from the same delayed precipitation problem as described in Section 4.4.2.

Additionally, now that U-AMP has demonstrated notable advantages over traditional separate category bulk schemes, the next step could be to work on designing an operational unified category bulk scheme. If done well, this could be a transformative step for bulk scheme development that fundamentally solves many existing problems, including autoconversion and sedimentation. Once an operational unified category bulk scheme is developed, it would be of great interest to assess how well it can enhance the accuracy of weather and climate prediction.

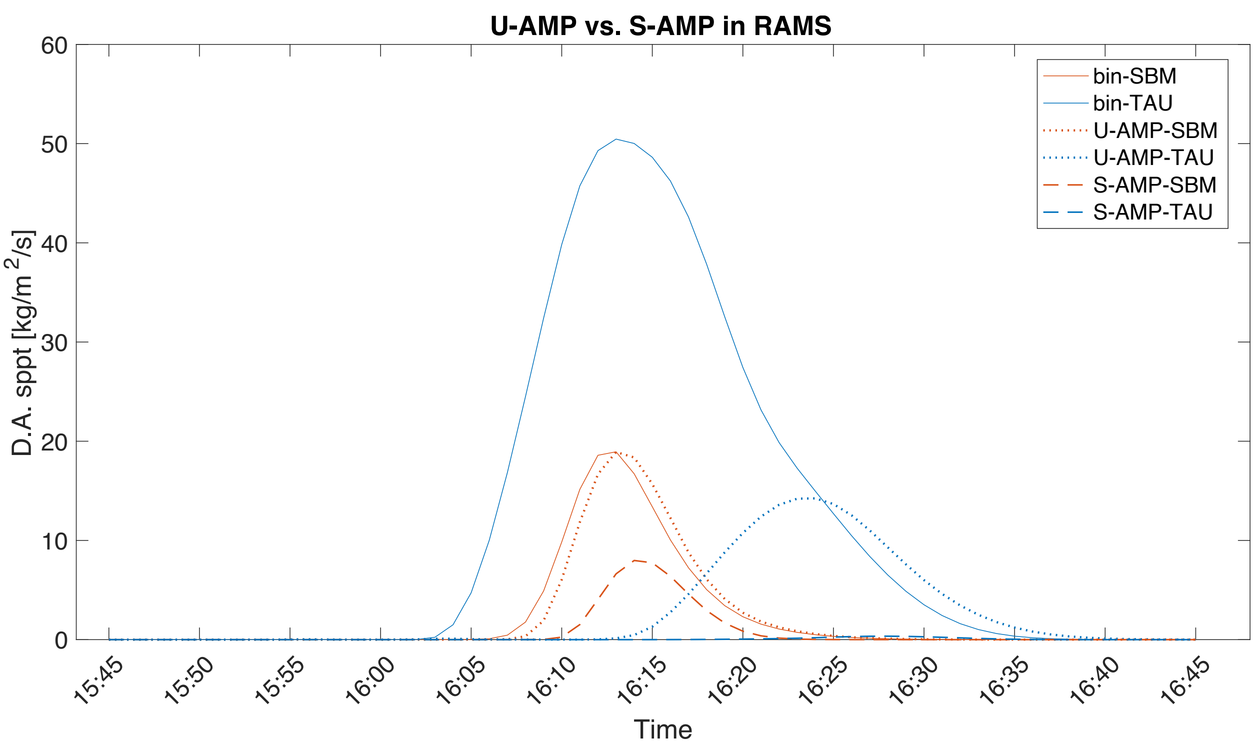

Figure 5.1. Domain averaged surface precipitation rate simulated in RAMS, comparing bin (solid), U-AMP (dotted), and S-AMP (dashed).

References

Abade, G. C., Grabowski, W. W., & Pawlowska, H. (2018). Broadening of cloud droplet spectra through eddy hopping: Turbulent entraining parcel simulations. *Journal of the Atmospheric Sciences*, *75*(10). https://doi.org/10.1175/JAS-D-18-0078.1

Abma, D., Heus, T., & Mellado, J. P. (2013). Direct numerical simulation of evaporative cooling at the lateral boundary of shallow cumulus clouds. *Journal of the Atmospheric Sciences*, *70*(7), 2088–2102. https://doi.org/10.1175/JAS-D-12-0230.1

Albrecht, B. A. (1989). Aerosols, cloud microphysics, and fractional cloudiness. *Science*, *245*(4923), 1227–1230. https://doi.org/10.1126/science.245.4923.1227

Austin, P., Wang, Y., Kujala, V., & Pincus, R. (1995). Precipitation in Stratocumulus Clouds: Observational and Modeling Results. *Journal of the Atmospheric Sciences*, *52*(13), 2329–2352. https://doi.org/10.1175/1520-0469(1995)052<2329:PISCOA>2.0.CO;2

Bates, T. S., Quinn, P. K., Coffman, D., Schulz, K., Covert, D. S., Johnson, J. E., et al. (2008). Boundary layer aerosol chemistry during TexAQS/GoMACCS 2006: Insights into aerosol sources and transformation processes. *Journal of Geophysical Research*, *113*, 1–18. https://doi.org/10.1029/2008jd010023

Beheng, K. D. (1994). A parameterization of warm cloud microphysical conversion processes. *Atmospheric Research*, *33*(1–4), 193–206. https://doi.org/10.1016/0169-8095(94)90020-5

Benjamin, S. G., Weygandt, S. S., Brown, J. M., Hu, M., Alexander, C. R., Smirnova, T. G., et al.

(2016). A North American hourly assimilation and model forecast cycle: The rapid refresh. *Monthly Weather Review*, *144*(4), 1669–1694. https://doi.org/10.1175/MWR-D-15-0242.1

Berry, E. X., & Reinhardt, R. L. (1974). An Analysis of Cloud Drop Growth by Collection: Part IV. A New Parameterization. *Journal of the Atmospheric Sciences*, *31*(8), 2127–2135. https://doi.org/10.1175/1520-0469(1974)031<2127:aaocdg>2.0.co;2

Boucher, O., Randall, D., Artaxo, P., Bretherton, C., Feingold, G., Forster, P., et al. (2014). Clouds and Aerosols. In *Climate Change 2013 – The Physical Science Basis* (Vol. 9781107057, pp. 571–658). Cambridge University Press. https://doi.org/10.1017/CBO9781107415324.016

Carman, J. K., Rossiter, D. L., Khelif, D., Jonsson, H. H., Faloona, I. C., & Chuang, P. Y. (2012). Observational constraints on entrainment and the entrainment interface layer in stratocumulus. *Atmospheric Chemistry and Physics*, *12*(22), 11135–11152. https://doi.org/10.5194/acp-12-11135-2012

Chandrakar, K. K., Cantrell, W., Chang, K., Ciochetto, D., Niedermeier, D., Ovchinnikov, M., et al. (2016). Aerosol indirect effect from turbulence-induced broadening of cloud-droplet size distributions. *Proceedings of the National Academy of Sciences of the United States of America*, *113*(50), 14243–14248. https://doi.org/10.1073/pnas.1612686113

Chen, J., Liu, Y., Zhang, M., & Peng, Y. (2016). New understanding and quantification of the regime dependence of aerosol-cloud interaction for studying aerosol indirect effects. *Geophysical Research Letters*, *43*(4), 1780–1787. https://doi.org/10.1002/2016GL067683

Chiu, J. C., Yang, C. K., van Leeuwen, P. J., Feingold, G., Wood, R., Blanchard, Y., et al. (2021). Observational Constraints on Warm Cloud Microphysical Processes Using Machine Learning and Optimization Techniques. *Geophysical Research Letters*, *48*(2), 1–13. https://doi.org/10.1029/2020GL091236

Chuang, P. Y., Saw, E. W., Small, J. D., Shaw, R. A., Sipperley, C. M., Payne, G. A., & Bachalo, W. D. (2008). Airborne phase Doppler interferometry for cloud microphysical measurements. *Aerosol Science and Technology*, *42*(8), 685–703. https://doi.org/10.1080/02786820802232956

Costa, A. A., De Oliveira, C. J., De Oliveira, J. C. P., & Sampaio, A. J. D. C. (2000). Microphysical observations of warm cumulus clouds in Ceara, Brazil. *Atmospheric Research*, *54*(2–3), 167–199. https://doi.org/10.1016/S0169-8095(00)00045-4

Falk, N. M., Igel, A. L., & Igel, M. R. (2019). The relative impact of ice fall speeds and microphysics parameterization complexity on supercell evolution. *Monthly Weather Review*, *147*(7), 2403–2415. https://doi.org/10.1175/MWR-D-18-0417.1

Fan, J., Leung, L. R., Li, Z., Morrison, H., Chen, H., Zhou, Y., et al. (2012). Aerosol impacts on clouds and precipitation in eastern China: Results from bin and bulk microphysics. *Journal of Geophysical Research: Atmospheres*, *117*(D16), n/a-n/a. https://doi.org/10.1029/2011JD016537

Fan, J., Wang, Y., Rosenfeld, D., & Liu, X. (2016). Review of aerosol-cloud interactions: Mechanisms, significance, and challenges. *Journal of the Atmospheric Sciences*, *73*(11), 4221–4252. https://doi.org/10.1175/JAS-D-16-0037.1

Feingold, G., Tzivion, S., & Levin, Z. (1988). Evolution of raindrop spectra. Part I: solution to the stochastic collection/breakup equation using the method of moments. *Journal of the Atmospheric Sciences*, *45*(22), 3387–3399. https://doi.org/10.1175/1520-0469(1988)045<3387:EORSPI>2.0.CO;2

Feingold, Graham, Walko, R. L., Stevens, B., & Cotton, W. R. (1998). Simulations of marine stratocumulus using a new microphysical parameterization scheme. *Atmospheric Research*, *47–48*, 505–528. https://doi.org/10.1016/S0169-8095(98)00058-1

Fovell, R. G., & Ogura, Y. (1988). Numerical simulation of a midlatitude squall line in two dimensions. *Journal of the Atmospheric Sciences*, *45*(24), 3846–3879. https://doi.org/10.1175/1520-0469(1988)045<3846:NSOAMS>2.0.CO;2

Gao, S., Ran, L., & Li, X. (2006). Impacts of ice microphysics on rainfall and thermodynamic processes in the tropical deep convective regime: A 2D cloud-resolving modeling study. *Monthly Weather Review*, *134*(10), 3015–3024. https://doi.org/10.1175/MWR3220.1

Ghan, S. J., Leung, L. R., Easter, R. C., & Abdul-Razzak, H. (1997). Prediction of cloud droplet number in a general circulation model. *Journal of Geophysical Research Atmospheres*, *102*(18), 21777–21794. https://doi.org/10.1029/97jd01810

Gillani, N. V., Schwartz, S. E., Leaitch, W. R., Strapp, J. W., & Isaac, G. A. (1995). Field observations in continental stratiform clouds: Partitioning of cloud particles between droplets and unactivated interstitial aerosols. *Journal of Geophysical Research*, *100*(D9), 18687. https://doi.org/10.1029/95JD01170

Gonçalves, F. L. T., Martins, J. A., & Silva Dias, M. A. (2008). Shape parameter analysis using cloud spectra and gamma functions in the numerical modeling RAMS during LBA Project at Amazonian region, Brazil. *Atmospheric Research*, *89*(1–2), 1–11. https://doi.org/10.1016/j.atmosres.2007.12.005

Grabowski, W. W. (1998). Toward Cloud Resolving Modeling of Large-Scale Tropical Circulations: A Simple Cloud Microphysics Parameterization. *Journal of the Atmospheric Sciences*, *55*(21), 3283–3298. https://doi.org/10.1175/1520-0469(1998)055<3283:tcrmol>2.0.co;2

Hartmann, D. (1992). *Global Physical Climatology*. *Physics Today*. San Diego: Academic Press.

Hill, A. A., Lebo, Z. J., Andrejczuk, M., Arabas, S., Dziekan, P., Field, P., et al. (2023). Toward a Numerical Benchmark for Warm Rain Processes. *Journal of the Atmospheric Sciences*, *80*(5), 1329–1359. https://doi.org/10.1175/JAS-D-21-0275.1

Hsieh, W. C., Jonsson, H., Wang, L. P., Buzorius, G., Flagan, R. C., Seinfeld, J. H., & Nenes, A. (2009). On the representation of droplet coalescence and autoconversion: Evaluation using ambient cloud droplet size distributions. *Journal of Geophysical Research Atmospheres*, *114*(7), 1–16. https://doi.org/10.1029/2008JD010502

Hu, A. Z., & Igel, A. L. (2023). A Bin and a Bulk Microphysics Scheme Can Be More Alike Than Two Bin Schemes Journal of Advances in Modeling Earth Systems. https://doi.org/10.1029/2022MS003303

Igel, A. L. (2019). Using an Arbitrary Moment Predictor to Investigate the Optimal Choice of

Prognostic Moments in Bulk Cloud Microphysics Schemes. *Journal of Advances in Modeling Earth Systems*. https://doi.org/10.1029/2019MS001733

Igel, A. L., & van den Heever, S. C. (2017). The importance of the shape of cloud droplet size distributions in shallow cumulus clouds. Part I: Bin microphysics simulations. *Journal of the Atmospheric Sciences*, *74*(1), 249–258. https://doi.org/10.1175/JAS-D-15-0382.1

Igel, A. L., Morrison, H., Santos, S. P., & van Lier-Walqui, M. (2022). Limitations of Separate Cloud and Rain Categories in Parameterizing Collision-Coalescence for Bulk Microphysics Schemes. *Journal of Advances in Modeling Earth Systems*, *14*(6), 1–20. https://doi.org/10.1029/2022ms003039

Jia, H., Ma, X., & Liu, Y. (2019). Exploring aerosol–cloud interaction using VOCALS-REx aircraft measurements. *Atmospheric Chemistry and Physics*, *19*(12), 7955–7971. https://doi.org/10.5194/acp-19-7955-2019

Johnson, J. S., Cui, Z., Lee, L. A., Gosling, J. P., Blyth, A. M., & Carslaw, K. S. (2015). Evaluating uncertainty in convective cloud microphysics using statistical emulation. *Journal of Advances in Modeling Earth Systems*, *7*(1), 162–187. https://doi.org/10.1002/2014MS000383

Kessler, E. (1969). On the Distribution and Continuity of Water Substance in Atmospheric Circulations. In *On the Distribution and Continuity of Water Substance in Atmospheric Circulations* (pp. 1–84). Boston, MA: American Meteorological Society. https://doi.org/10.1007/978-1-935704-36-2_1

Khain, A., Pokrovsky, A., Pinsky, M., Seifert, A., & Phillips, V. (2004). Simulation of effects of atmospheric aerosols on deep turbulent convective clouds using a spectral microphysics mixed-phase cumulus cloud model. Part I: Model description and possible applications. *Journal of the Atmospheric Sciences*, *61*(24), 2963–2982. https://doi.org/10.1175/JAS-3350.1

Khain, A. P., Beheng, K. D., Heymsfield, A., Korolev, A., Krichak, S. O., Levin, Z., et al. (2015). Representation of microphysical processes in cloud-resolving models: Spectral (bin) microphysics versus bulk parameterization. *Reviews of Geophysics*, *53*(2), 247–322. https://doi.org/10.1002/2014RG000468

Khairoutdinov, M., & Kogan, Y. (2000). A new cloud physics parameterization in a large-eddy simulation model of marine stratocumulus. *Monthly Weather Review*, *128*(1), 229–243. https://doi.org/10.1175/1520-0493(2000)128<0229:ANCPPI>2.0.CO;2

Koenig, L. R., & Murray, F. W. (1976). Ice-Bearing Cumulus Cloud Evolution: Numerical Simulation and General Comparison Against Observations. *Journal of Applied Meteorology*, *15*(7), 747–762. https://doi.org/10.1175/1520-0450(1976)015<0747:IBCCEN>2.0.CO;2

Kogan, Y. (2013). A cumulus cloud microphysics parameterization for cloud-resolving models. *Journal of the Atmospheric Sciences*, *70*(5), 1423–1436. https://doi.org/10.1175/JAS-D-12-0183.1

Kogan, Y. L., & Belochitski, A. (2012). Parameterization of cloud microphysics based on full integral moments. *Journal of the Atmospheric Sciences*, *69*(7), 2229–2242. https://doi.org/10.1175/JAS-D-11-0268.1

Kumar, B., Bera, S., Prabha, T. V., & Grabowski, W. W. (2017). Cloud-edge mixing: Direct numerical simulation and observations in Indian Monsoon clouds. *Journal of Advances in Modeling Earth Systems*, *9*(1), 332–353. https://doi.org/10.1002/2016MS000731

Lasher-Trapp, S. G., Cooper, W. A., & Blyth, A. M. (2005). Broadening of droplet size distributions from entrainment and mixing in a cumulus cloud. *Quarterly Journal of the Royal Meteorological Society*, *131*(605), 195–220. https://doi.org/10.1256/qj.03.199

Lee, H., & Baik, J. J. (2017). A physically based autoconversion parameterization. *Journal of the Atmospheric Sciences*, *74*(5), 1599–1616. https://doi.org/10.1175/JAS-D-16-0207.1

Li, X., Tao, W. K., Khain, A. P., Simpson, J., & Johnson, D. E. (2009). Sensitivity of a cloud-resolving model to bulk and explicit bin microphysical schemes. Part I: Comparisons. *Journal of the Atmospheric Sciences*, *66*(1), 3–21. https://doi.org/10.1175/2008JAS2646.1

van Lier-Walqui, M., Morrison, H., Kumjian, M. R., Reimel, K. J., Prat, O. P., Lunderman, S., & Morzfeld, M. (2020). A Bayesian approach for statistical–physical bulk parameterization of rain microphysics. Part II: Idealized Markov chain Monte Carlo experiments. *Journal of the Atmospheric Sciences*, *77*(3), 1043–1064. https://doi.org/10.1175/JAS-D-19-0071.1

Lin, Y. L., Farley, R. D., & Orville, H. D. (1983). Bulk parameterization of the snow field in a cloud model. *Journal of Climate & Applied Meteorology*, *22*(6), 1065–1092. https://doi.org/10.1175/1520-0450(1983)022<1065:BPOTSF>2.0.CO;2

Liu, Q., Kogan, Y. L., Lilly, D. K., & Khairoutdinov, M. P. (1997). Variational optimization method for calculation of cloud drop growth in an Eulerian drop-size framework. *Journal of the Atmospheric Sciences*, *54*(20), 2493–2504. https://doi.org/10.1175/1520-0469(1997)054<2493:VOMFCO>2.0.CO;2

Liu, Y., & Daum, P. H. (2002). Indirect warming effect from dispersion forcing. *Nature*, *419*(6907), 580–581. https://doi.org/10.1038/419580a

Liu, Y., & Daum, P. H. (2004). Parameterization of the autoconversion process. Part I: Analytical formulation of the Kessler-type parameterization. *Journal of the Atmospheric Sciences*, *61*(13), 1539–1548. https://doi.org/10.1175/1520-0469(2004)061<1539:POTAPI>2.0.CO;2

Lohmann, U., & Feichter, J. (2005). Global indirect aerosol effects: a review. *Atmospheric Chemistry and Physics*, *5*(3), 715–737. https://doi.org/10.5194/acp-5-715-2005

Lohmann, Ulrike, Feichter, J., Chuang, C. C., & Penner, J. E. (1999). Prediction of the number of cloud droplets in the ECHAM GCM. *Journal of Geophysical Research Atmospheres*, *104*(D8), 9169–9198. https://doi.org/10.1029/1999JD900046

Lord, S. J., Willoughby, H. E., & Piotrowicz, J. M. (1984). Role of a parameterized ice-phase microphysics in an axisymmetric, nonhydrostatic tropical cyclone model. *Journal of the Atmospheric Sciences*, *41*(19), 2836–2848. https://doi.org/10.1175/1520-0469(1984)041<2836:ROAPIP>2.0.CO;2

Lu, C., Liu, Y., Niu, S., & Vogelmann, A. M. (2012). Observed impacts of vertical velocity on cloud microphysics and implications for aerosol indirect effects. *Geophysical Research*

Letters, *39*(21). https://doi.org/10.1029/2012GL053599

Lu, M.-L., Conant, W. C., Jonsson, H. H., Varutbangkul, V., Flagan, R. C., & Seinfeld, J. H. (2007). The Marine Stratus/Stratocumulus Experiment (MASE): Aerosol-cloud relationships in marine stratocumulus. *Journal of Geophysical Research: Atmospheres*, *112*(D10). https://doi.org/10.1029/2006JD007985

Lu, M. L., & Seinfeld, J. H. (2006). Effect of aerosol number concentration on cloud droplet dispersion: A large-eddy simulation study and implications for aerosol indirect forcing. *Journal of Geophysical Research Atmospheres*, *111*(2), 1–16. https://doi.org/10.1029/2005JD006419

Ma, J., Chen, Y., Wang, W., Yan, P., Liu, H., Yang, S., et al. (2010). Strong air pollution causes widespread haze-clouds over China. *Journal of Geophysical Research Atmospheres*, *115*(18), 1–21. https://doi.org/10.1029/2009JD013065

Martin, G. M., Johnson, D. W., & Spice, A. (1994). The Measurement and Parameterization of Effective Radius of Droplets in Warm Stratocumulus Clouds. *Journal of the Atmospheric Sciences*, *51*(13), 1823–1842. https://doi.org/10.1175/1520-0469(1994)051<1823:tmapoe>2.0.co;2

Martins, J. A., & Silva Dias, M. A. F. (2009). The impact of smoke from forest fires on the spectral dispersion of cloud droplet size distributions in the Amazonian region. *Environmental Research Letters*, *4*(1). https://doi.org/10.1088/1748-9326/4/1/015002

McCumber, M., Wei-Kuo Tao, Simpson, J., Penc, R., & Su-Tzai Soong. (1991). Comparison of ice-phase microphysical parameterization schemes using numerical simulations of tropical convection. *Journal of Applied Meteorology*, *30*(7). https://doi.org/10.1175/1520-0450-30.7.985

Meyers, M. P., Walko, R. L., Harrington, J. Y., & Cotton, W. R. (1997). New RAMS cloud microphysics parameterization. Part II: The two-moment scheme. *Atmospheric Research*, *45*(1), 3–39. https://doi.org/10.1016/S0169-8095(97)00018-5

Milbrandt, J. A., & McTaggart-Cowan, R. (2010). Sedimentation-induced errors in bulk microphysics schemes. *Journal of the Atmospheric Sciences*, *67*(12), 3931–3948. https://doi.org/10.1175/2010JAS3541.1

Milbrandt, Jason A., & Yau, M. K. (2005). A multimoment bulk microphysics parameterization. Part I: Analysis of the role of the spectral shape parameter. *Journal of the Atmospheric Sciences*, *62*(9), 3051–3064. https://doi.org/10.1175/JAS3534.1

Milbrandt, Jason A., Bélair, S., Faucher, M., Vallée, M., Carrera, M. L., & Glazer, A. (2016). The pan-canadian high resolution (2.5 km) deterministic prediction system. *Weather and Forecasting*, *31*(6), 1791–1816. https://doi.org/10.1175/WAF-D-16-0035.1

Ming, Y., Ramaswamy, V., Donner, L. J., Phillips, V. T. J., Klein, S. A., Ginoux, P. A., & Horowitz, L. W. (2007). Modeling the interactions between aerosols and liquid water clouds with a self-consistent cloud scheme in a general circulation model. *Journal of the Atmospheric Sciences*, *64*(4), 1189–1209. https://doi.org/10.1175/JAS3874.1

Morrison, H. (2012). On the numerical treatment of hydrometeor sedimentation in bulk and hybrid bulk-bin microphysics schemes. *Monthly Weather Review*, *140*(5), 1572–

1588. https://doi.org/10.1175/MWR-D-11-00140.1

Morrison, H., & Gettelman, A. (2008). A new two-moment bulk stratiform cloud microphysics scheme in the community atmosphere model, version 3 (CAM3). Part I: Description and numerical tests. *Journal of Climate*, *21*(15), 3642–3659. https://doi.org/10.1175/2008JCLI2105.1

Morrison, H., & Grabowski, W. W. (2007). Comparison of Bulk and Bin Warm-Rain Microphysics Models Using a Kinematic Framework. *Journal of the Atmospheric Sciences*, *64*(8), 2839–2861. https://doi.org/10.1175/jas3980

Morrison, H., Milbrandt, J. A., Bryan, G. H., Ikeda, K., Tessendorf, S. A., & Thompson, G. (2015). Parameterization of cloud microphysics based on the prediction of bulk ice particle properties. Part II: Case study comparisons with observations and other schemes. *Journal of the Atmospheric Sciences*, *72*(1), 312–339. https://doi.org/10.1175/JAS-D-14-0066.1

Morrison, H., van Lier-Walqui, M., Kumjian, M. R., & Prat, O. P. (2020). A Bayesian approach for statistical–physical bulk parameterization of rain microphysics. Part I: Scheme description. *Journal of the Atmospheric Sciences*, *77*(3), 1019–1041. https://doi.org/10.1175/JAS-D-19-0070.1

Morrison, H., van Lier-Walqui, M., Fridlind, A. M., Grabowski, W. W., Harrington, J. Y., Hoose, C., et al. (2020). *Confronting the Challenge of Modeling Cloud and Precipitation Microphysics*. *Journal of Advances in Modeling Earth Systems* (Vol. 12). https://doi.org/10.1029/2019MS001689

Noonkester, V. R. (1984). Droplet Spectra Observed in Marine Stratus Cloud Layers. *Journal of the Atmospheric Sciences*, *41*(5), 829–845. https://doi.org/10.1175/1520-0469(1984)041<0829:DSOIMS>2.0.CO;2

Pandithurai, G., Dipu, S., Prabha, T. V., Maheskumar, R. S., Kulkarni, J. R., & Goswami, B. N. (2012). Aerosol effect on droplet spectral dispersion in warm continental cumuli. *Journal of Geophysical Research Atmospheres*, *117*(16). https://doi.org/10.1029/2011JD016532

Pawlowska, H., Grabowski, W. W., & Brenguier, J.-L. (2006). Observations of the width of cloud droplet spectra in stratocumulus. *Geophysical Research Letters*, *33*(19). https://doi.org/10.1029/2006GL026841

Peng, Y., & Lohmann, U. (2003). Sensitivity study of the spectral dispersion of the cloud droplet size distribution on the indirect aerosol effect. *Geophysical Research Letters*, *30*(10), n/a-n/a. https://doi.org/10.1029/2003gl017192

Perrin, V. E., & Jonker, H. J. J. (2015). Lagrangian droplet dynamics in the subsiding shell of a cloud using direct numerical simulations. *Journal of the Atmospheric Sciences*, *72*(10), 4015–4028. https://doi.org/10.1175/JAS-D-15-0045.1

Pöschl, U. (2005). Atmospheric aerosols: Composition, transformation, climate and health effects. *Angewandte Chemie - International Edition*, *44*(46), 7520–7540. https://doi.org/10.1002/anie.200501122

Prabha, T. V., Patade, S., Pandithurai, G., Khain, A., Axisa, D., Pradeep-Kumar, P., et al. (2012). Spectral width of premonsoon and monsoon clouds over Indo-Gangetic valley. *Journal* *of Geophysical Research Atmospheres*, *117*(20), 1–15. https://doi.org/10.1029/2011JD016837

Redemann, J., Wood, R., Zuidema, P., Doherty, S., Luna, B., LeBlanc, S., et al. (2020). An overview of the ORACLES (ObseRvations of Aerosols above CLouds and their intEractionS) project: aerosol-cloud-radiation interactions in the Southeast Atlantic basin. *Atmospheric Chemistry and Physics*, (June), 1–82. https://doi.org/10.5194/acp-2020-449

Rosenfeld, D., Lohmann, U., Raga, G. B., O'Dowd, C. D., Kulmala, M., Fuzzi, S., et al. (2008). Flood or Drought: How Do Aerosols Affect Precipitation? *Science*, *321*(5894), 1309–1313. https://doi.org/10.1126/science.1160606

Rotstayn, L. D., & Liu, Y. (2003). Sensitivity of the first indirect aerosol effect to an increase of cloud droplet spectral dispersion with droplet number concentration. *Journal of Climate*, *16*(21), 3476–3481. https://doi.org/10.1175/1520-0442(2003)016<3476:SOTFIA>2.0.CO;2

Rutledge, S. A., & Hobbs, P. V. (1984). Mesoscale and Microscale Structure and Organization of Clouds and Precipitation in Midlatitude Cyclones. Xii: a Diagnostic Modeling Study of Precipitation Development in Narrow Cold-Frontal Rainbands. *Journal of the Atmospheric Sciences*, *41*(20), 2949–2972. https://doi.org/10.1175/1520-0469(1984)041<2949:TMAMSA>2.0.CO;2

Seifert, A., & Beheng, K. D. (2001). A double-moment parameterization for simulating autoconversion, accretion and selfcollection. *Atmospheric Research*, *59–60*. https://doi.org/10.1016/S0169-8095(01)00126-0

Seifert, A., & Beheng, K. D. (2006a). A two-moment cloud microphysics parameterization for mixed-phase clouds. Part 1: Model description. *Meteorology and Atmospheric Physics*, *92*(1–2), 45–66. https://doi.org/10.1007/s00703-005-0112-4

Seifert, A., & Beheng, K. D. (2006b). A two-moment cloud microphysics parameterization for mixed-phase clouds. Part 2: Maritime vs. continental deep convective storms. *Meteorology and Atmospheric Physics*, *92*(1–2), 67–82. https://doi.org/10.1007/s00703-005-0113-3

Seifert, A., & Rasp, S. (2020). Potential and Limitations of Machine Learning for Modeling Warm-Rain Cloud Microphysical Processes. *Journal of Advances in Modeling Earth Systems*, *12*(12). https://doi.org/10.1029/2020MS002301

Shima, S., Kusano, K., Kawano, A., Sugiyama, T., & Kawahara, S. (2009). The super-droplet method for the numerical simulation of clouds and precipitation: a particle-based and probabilistic microphysics model coupled with a non-hydrostatic model. *Quarterly Journal of the Royal Meteorological Society*, *135*(642), 1307–1320. https://doi.org/10.1002/qj.441

Shipway, B. J., & Hill, A. A. (2012). Diagnosis of systematic differences between multiple parametrizations of warm rain microphysics using a kinematic framework. *Quarterly Journal of the Royal Meteorological Society*, *138*(669), 2196–2211. https://doi.org/10.1002/qj.1913

Stephens, G. L. (2005). Cloud feedbacks in the climate system: A critical review. *Journal of Climate*, *18*(2), 237–273. https://doi.org/10.1175/JCLI-3243.1

Stevens, B., & Feingold, G. (2009). Untangling aerosol effects on clouds and precipitation in a buffered system. *Nature*, *461*(7264), 607–613. https://doi.org/10.1038/nature08281

Stevens, B., Feingold, G., Cotton, W. R., & Walko, R. L. (1996). Elements of the microphysical structure of numerically simulated nonprecipitating stratocumulus. *Journal of the Atmospheric Sciences*, *53*(7), 980–1006. https://doi.org/10.1175/1520-0469(1996)053<0980:EOTMSO>2.0.CO;2

Szyrmer, W., Laroche, S., & Zawadzki, I. (2005). A microphysical bulk formulation based on scaling normalization of the particle size distribution. Part I: Description. *Journal of the Atmospheric Sciences*, *62*(12), 4206–4221. https://doi.org/10.1175/JAS3620.1

Thompson, G., Field, P. R., Rasmussen, R. M., & Hall, W. D. (2008). Explicit forecasts of winter precipitation using an improved bulk microphysics scheme. Part II: Implementation of a new snow parameterization. *Monthly Weather Review*, *136*(12), 5095–5115. https://doi.org/10.1175/2008MWR2387.1

Trenberth, K. E., Jones, P. D., Ambenje, P., Bojariu, R., Easterling, D., Klein Tank, A., et al. (2007). Observations: surface and atmospheric climate change. *Changes*, *164*(236–336), 235–336. https://doi.org/10.5194/cp-6-379-2010

Twomey, S. (1974). Pollution and the Planetary Albedo. *Atmospheric Environment*, *41*(SUPPL.), 120–125. https://doi.org/10.1016/0004-6981(74)90004-3

Twomey, S. (1977). The Influence of Pollution on the Shortwave Albedo of Clouds. *Journal of the Atmospheric Sciences*. https://doi.org/10.1175/1520-

0469(1977)034<1149:tiopot>2.0.co;2

Tzivion, S., Feingold, G., & Levin, Z. (1987). An efficient numerical solution to the stochastic collection equation. *Journal of the Atmospheric Sciences*. https://doi.org/10.1175/1520-0469(1987)044<3139:aenstt>2.0.co;2

Tzivion, S., Reisin, T. G., & Levin, Z. (1999). A Numerical Solution of the Kinetic Collection Equation Using High Spectral Grid Resolution: A Proposed Reference. *Journal of Computational Physics*, *148*(2), 527–544. https://doi.org/10.1006/jcph.1998.6128

Vie, B., Pinty, J. P., Berthet, S., & Leriche, M. (2016). LIMA (v1.0): A quasi two-moment microphysical scheme driven by a multimodal population of cloud condensation and ice freezing nuclei. *Geoscientific Model Development*, *9*(2), 567–586. https://doi.org/10.5194/gmd-9-567-2016

Wang, J., Daum, P. H., Kleinman, L. I., Lee, Y., Schwartz, S. E., Springston, S. R., et al. (2007). Observation of ambient aerosol particle growth due to in-cloud processes within boundary layers. *Journal of Geophysical Research*, *112*(D14), D14207. https://doi.org/10.1029/2006JD007989

Wang, X., Xue, H., Fang, W., & Zheng, G. (2011). A study of shallow cumulus cloud droplet dispersion by large eddy simulations. *Acta Meteorologica Sinica*, *25*(2), 166–175. https://doi.org/10.1007/s13351-011-0024-9

Wang, Yang, Zhao, C., McFarquhar, G. M., Wu, W., Reeves, M., & Li, J. (2021). Dispersion of Droplet Size Distributions in Supercooled Non-precipitating Stratocumulus from Aircraft Observations Obtained during the Southern Ocean Cloud Radiation Aerosol

Transport Experimental Study. *Journal of Geophysical Research: Atmospheres*, *126*(6), 1–15. https://doi.org/10.1029/2020jd033720

Wang, Yuan, Fan, J., Zhang, R., Leung, L. R., & Franklin, C. (2013). Improving bulk microphysics parameterizations in simulations of aerosol effects. *Journal of Geophysical Research Atmospheres*, *118*(11), 5361–5379. https://doi.org/10.1002/jgrd.50432

Wood, R. (2005). Drizzle in Stratiform Boundary Layer Clouds. Part I: Vertical and Horizontal Structure. *Journal of the Atmospheric Sciences*, *62*(9), 3011–3033. https://doi.org/10.1175/JAS3529.1

Xue, L., Fan, J., Lebo, Z. J., Wu, W., Morrison, H., Grabowski, W. W., et al. (2017). Idealized simulations of a squall line from the MC3E field campaign applying three bin microphysics schemes: Dynamic and thermodynamic structure. *Monthly Weather Review*, *145*(12), 4789–4812. https://doi.org/10.1175/MWR-D-16-0385.1

Yum, S. S., & Hudson, J. G. (2005). Adiabatic predictions and observations of cloud droplet spectral broadness. *Atmospheric Research*, *73*(3–4), 203–223. https://doi.org/10.1016/j.atmosres.2004.10.006

Zheng, X., Albrecht, B., Jonsson, H. H., Khelif, D., Feingold, G., Minnis, P., et al. (2011). Observations of the boundary layer, cloud, and aerosol variability in the southeast Pacific near-coastal marine stratocumulus during VOCALS-REx. *Atmospheric Chemistry and Physics*, *11*(18), 9943–9959. https://doi.org/10.5194/acp-11-9943-2011